2019

Computational Simulation of a Femoral Nail Fracture

Stephen Charles Whatley
Wright State University

COMPUTATIONAL SIMULATION OF A FEMORAL NAIL FRACTURE

A Thesis submitted in partial fulfillment of the
requirements for the degree of
Master of Science in Biomedical Engineering

By

STEPHEN CHARLES WHATLEY
B.S., Metropolitan State University of Denver Colorado, 2015

2019
Wright State University

WRIGHT STATE UNIVERSITY
GRADUATE SCHOOL

05/01/2019

I HEREBY RECOMMEND THAT THE THESIS PREPARED UNDER MY SUPERVISION BY Stephen Charles Whatley ENTITLED COMPUTATIONAL SIMULATION OF A FEMORAL NAIL FRACTURE BE ACCEPTED IN PARTIAL FULFILLMENT OF THE REQUIREMENTS FOR THE DEGREE OF Master of Science in Biomedical Engineering.

_____
Tarun Goswami, D.Sc.
Thesis Director

_____
John C. Gallagher, Ph.D.
Chair, Department of
Biomedical, Industrial and
Human Factors Engineering

Committee on Final Examination:

_____
Caroline GL Cao, PhD.

_____
Ulas Sunar, Ph.D.

_____
Tarun Goswami, D.Sc

_____
Barry Milligan, Ph.D.
Interim Dean of the Graduate School

Abstract

Whatley, Stephen Charles. M.S.B.M.E. Department of Biomedical, Industrial and Human Factors Engineering, Wright State University, 2019. COMPUTATIONAL SIMULATION OF A FEMORAL NAIL FRACTURE.

Every year in the United States roughly 300,000 people over the age of 65 suffer from a hip fracture. Ninety five percent of which are the result from a fall. The resulting hip fracture can be classified into several categories of fracture. Depending on the damage the patient could be implanted with a femoral nail device to assist in their recovery. These devices can, however, have complications during recovery. In some cases, these nails can have a failure rate as high as 10%. When failure occurs, extensive investigations are needed to determine the causes of failure. These investigations involve physical examination, testing for material and chemical properties, and numerical computation with computer simulations. The results from this investigation show that the nail investigated may have accrued damage from the implantation process. There is evidence of internal crack propagation leading to device failure. Simulations performed indicate that if the nail was operating in a femur with a subtrochanteric fracture the internal forces may have been 50% higher than that of a normal femur, significantly more than any fracture type.

Table of Contents

Table of Figures

Table of Tables

Acknowledgements

I'd like to thank Dr. Tarun Goswami for giving me the opportunity and guidance needed to do this thesis. His teaching is what allowed me to get where I am now. I'd like to thank Farah Hamandi. She has been a constant source of help and guidance for this project. And, of course, I'd like to thank my parents Donna and Tom Norman. Without everything they have provided for me none of this could be possible.

CHAPTER 1: INTRODUCTION

1.1 Introduction

In the United States roughly 300,000 people over the age of sixty-five are hospitalized every year with a hip fracture [10, 23, 27]. Ninety five percent of these hip fractures are the result of the impact resulting from a fall [27]. The resulting fractures generally fall into three primary categories: intracapsular, intertrochanteric, and subtrochanteric fractures [26] (Figure 1.1.1). An intracapsular fracture is characterized as a fracture located below the head or along the neck of the femur [2, 53]. An intertrochanteric fracture is defined as a fracture on the femur located between the greater and lesser trochanter [34]. A subtrochanteric fracture is a fracture located below the lesser trochanter [4]. There exist various methods used to treat hip fractures and put them on the path to recovery [35]. One such option is the use of an internal fixation device [30]. An internal fixation device classified is a medical device implanted within the body for the purpose of stabilizing and joins bone fractures allowing the bone to heal [9]. The healing process can, however, come to an immediate stop. This can happen as a result from the medical device failing. For cephalomedullary nails, the failure rate can be as high as 10% when used to treat subtrochanteric fractures. [31, 49, 54] In the event such a failure occurs, steps must be taken to prevent future incidence. Part of this process involves investigating the cause of the failure.

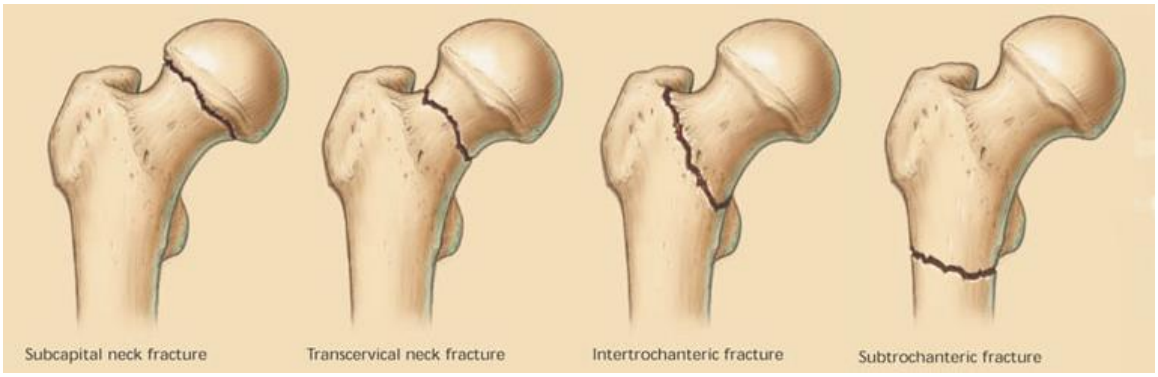

Figure 1.1.1 Different types of hip fractures. Retrieved from [26].

1.2 Motivation

With every medical device, much like any device, there is always the risk that it might fail. For medical devices, a failure can occur when the device does not perform the task for which it is being used. [25, 42] It is also possible that a medical device can fail when the device breaks and can no longer perform its function [8, 31, 38]. A case of the former would be something like an intramedullary nail being implanted in order to mend a broken bone and after a few months the bone fracture failed to fuse. A case of the latter would be the same nail breaking in two because it was overloaded. Both cases are failures, but what events that led up to the failure are quite different. In either case when a failure occurs, someone will be tasked with finding out why the failure transpired. Knowing how and why a device failed is very valuable knowledge. Failure has a good way of showing where a design is weak. As engineers, we often think of how a device should work, but not always obvious the ways it can fail. Failure can be a good thing for a design providing that you have the means to understand why the failure occurred. In order to understand how something fails, there needs to be an extensive effort made to collect evidence from a broad spectrum of

categories. For failures of this kind, it is seldom from a singular cause or event. Because of this, the investigator must look at every possible avenue before drawing conclusions. [22] This can include physical examination, testing for material and chemical properties, and numerical commutation with computer simulations. Only after every possible contributing factor is examined can the puzzle be pieced together.

1.3 Goals

There are two overall goals to be accomplished during the duration of this project. First is the collection of physical evidence from the failed intramedullary nail. This will be performed through various methods such as visual examination and observation under optical and scanning electron microscopes (SEM). Chemical composition and microstructure analysis will also be examined for possible leads for defects. By collecting evidence from the failed device, a case for how the device failed can be developed.

The second goal for this thesis is to develop and test different models for the femur. These models will represent three different types of hip fractures. By testing different fracture types, it can be determined how these fracture types affect the forces that the nail undergoes during loading. Understanding the effect that the factures have on the intramedullary nail can help the risks that could arise though use. [60]

CHAPTER 2: Background

2.1 Case Study

It was established that the device was implanted in August of 2017. The patient did not appear to have any issues for about three months. In December of 2017 the patient came in complaining of pain from the fracture site. X-rays showed that the device failed and was surgically removed. The device came into the school's possession in January of 2018. The device was in five separate parts (Figures 2.1.1-2.1.4). The failed nail was in two pieces fractured along the thin walls on the proximal portion. The other three pieces of the device were a self-tapping helical screw and two screws that secured the distal portion of the nail in vivo. Other than the timeframe for the device being in vivo, no other patient information, such as demography and radiological reports, were available for examination.

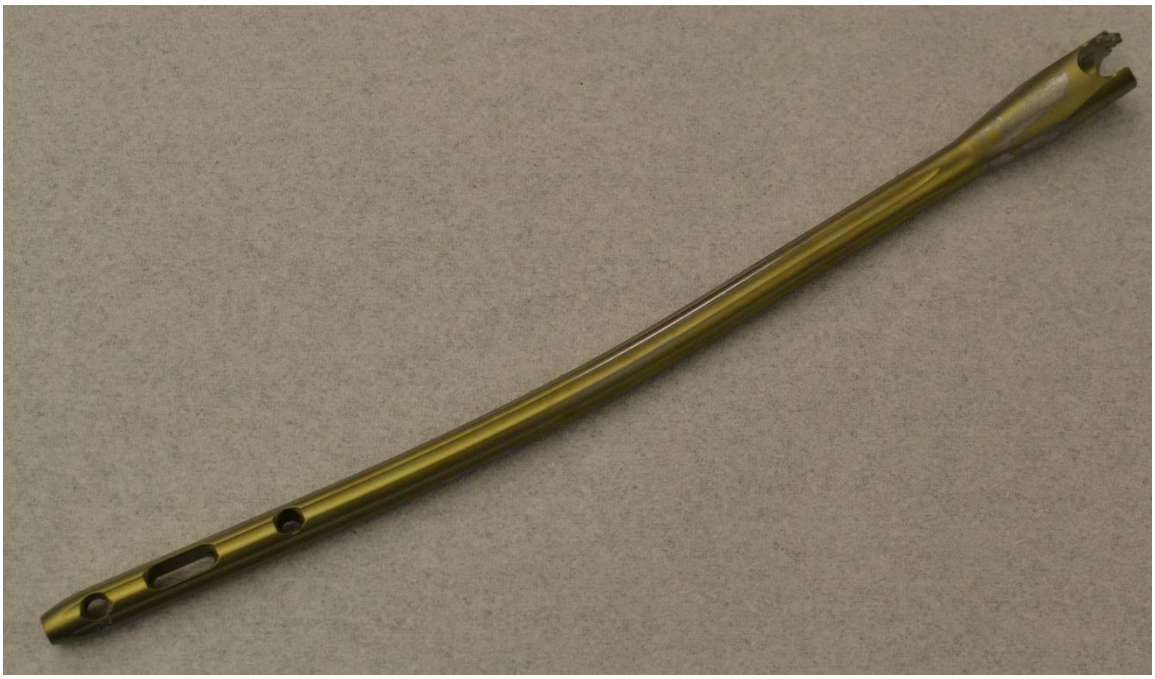

Figure 2.1.1 Distal portion of the failed nail.

Figure 2.1.2 Proximal portion of the failed nail.

Figure 2.1.3 Self-tapping helical screw.

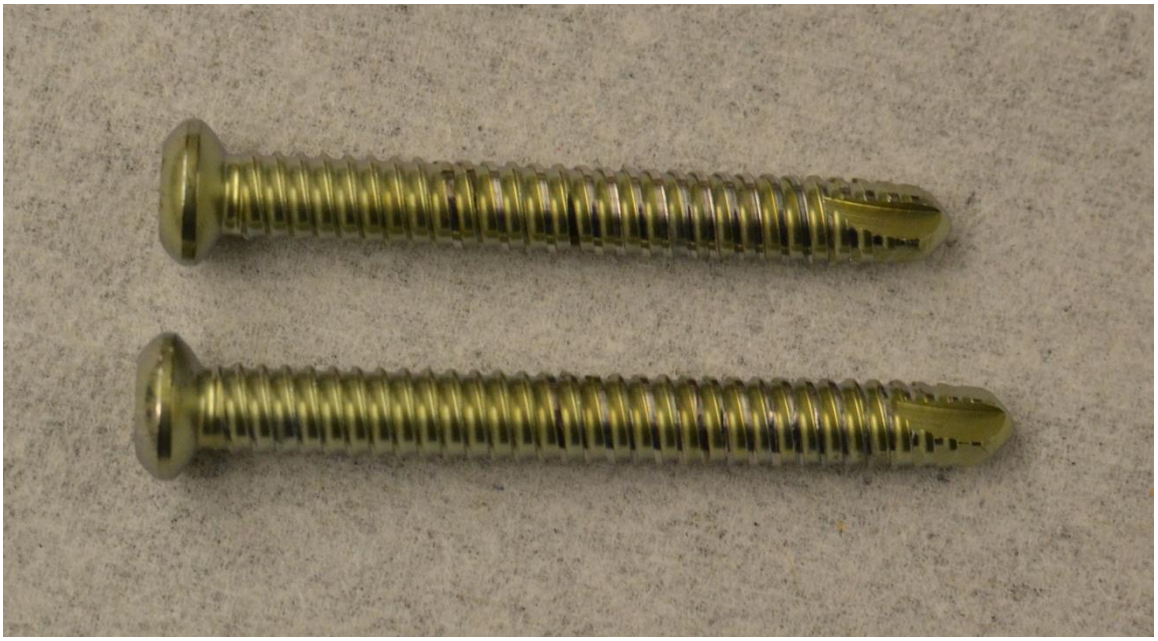

Figure 2.1.4 Distal locking screws

2.2 Device Information

How to mend broken bones has been a problem mankind has struggled with since the inception of medical treatment [50, 51]. Throughout the millennia, the solutions for this problem have evolved. Some of the oldest methods were to simply immobilize the fractured limb and just hoping for the best [7, 47]. This often left the patient with permanent deformities and other complications [5, 47].

In the past couple of hundred years, doctors performed surgeries to set the bones in place before being put in a cast and allowed time for the bone to heal. While this was an improvement over older methods it too, was not without its flaws. This method took months to complete [13, 49]. During this time the patient was not allowed to move [49]. This was because doing so ran the possibility of moving the fractured bits of bone leading to not heal properly resulting in permanent bone deformity [47]. In modern times we have adopted the use of internal fixation devices in order to mend serious bone fractures. Unlike previous methods of repairing bone fractures internal fixation devices offer several benefits, such as quicker recovery times and without the immobility that comes using a cast [44].

Figure 2.2.1Intramedulleary nail in vivo. Retrieved from [12]

Internal fixation devices cover a broad spectrum of device types. They can include metal plates, pins, nails, screws, and even wire [59, 6, 11, 1, 19, 3]. The internal fixation device investigated during this project is an intramedullary nail. Intramedullary nails work by being implanted within a fractured long bone and secured with a series of pins and or screws [56, 57] (Figure 2.2.1). The body of the nail provides stability to the long bone while being able help support external weight [17, 55]. These features allow the patient mobility that one could not find using a cast or splint [38]. Following hip replacement surgery today, patients are sometimes able to move on their own in as quickly as the day following surgery.

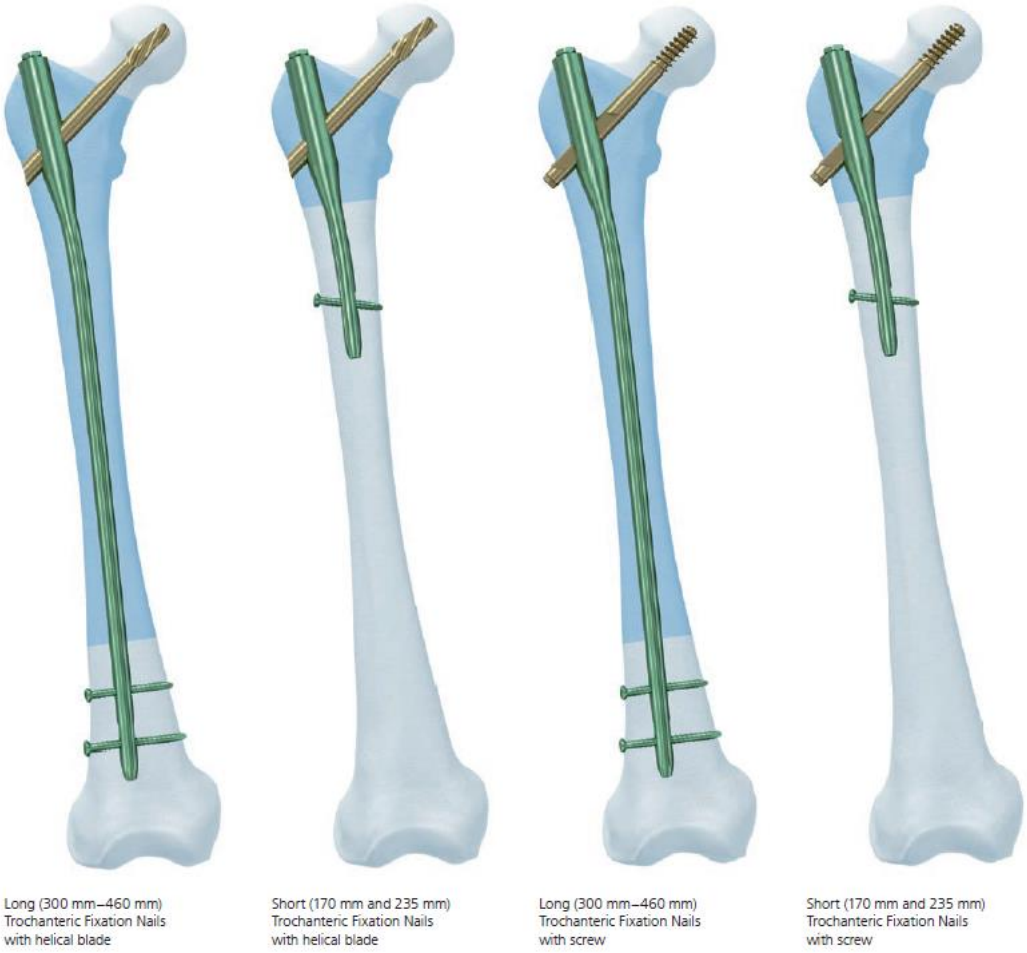

Figure 2.2.2 Different types of cephalomedullary nails. Retrieved from [12].

The specific type of nail we received was a cephalomedullary nail (Figure 2.2.2). What makes this nail different from other types of nail is the use of one or more large self-tapping screws. Unlike other screws, this screw is used only to gain purchase to the bone, these large screws provide load-bearing support to the nail as well as purchase to the bone. The self-taping screws are inserted through the nail at an angle between 125°-135° (Figure 2.2.3). The screw cuts into medullary cavity of the femoral head gaining purchase to the bone. The screw is then locked into place and the nail is capped. These screws are what transfer

weight of the body from the head of the femur to the nail body. The failed nail we received was a right side, 10mm diameter by 320mm long nail that mated with 80mm long screw at 125°. The nail was made of the titanium alloy Ti-15Mo and the other device composites were made of the alloy Ti-6Al-7Nb. The failure was in the section where the nail and the self-tapping screw mated.

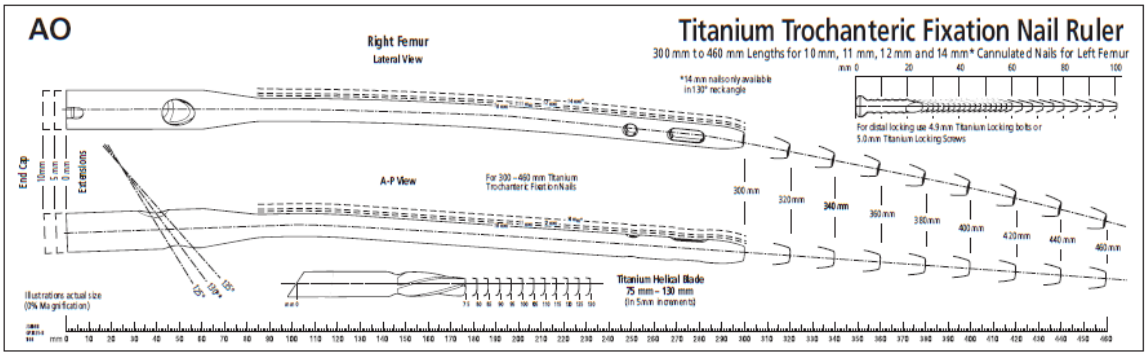

Figure 2.2.3 Diagram of nail variability. Retrieved from [12].

2.3 Hip Biomechanics

Through the process of movement, the body undergoes several internal forces. Even with simple and regular movements such as walking, the femur can experience intense internal forces. During the gait cycle the proximal portion of the femur experience a complex range of three-dimensional forces (Figure 2.3.1). During loading cycle the head and neck of the femur can experience forces up to 3.5 times the human body weight [18, 20]. During the gait cycle the femoral head can rotate between 40°-50°. [18] The hip can also experience up to 35° flection and 10° extensions. [18] These forces add to create a dynamic environment of loading conditions that intramedullary nail must contend with. Because of the wide range of internal forces, the intramedullary nail needs several levels of safety factors greater than the human body weight.

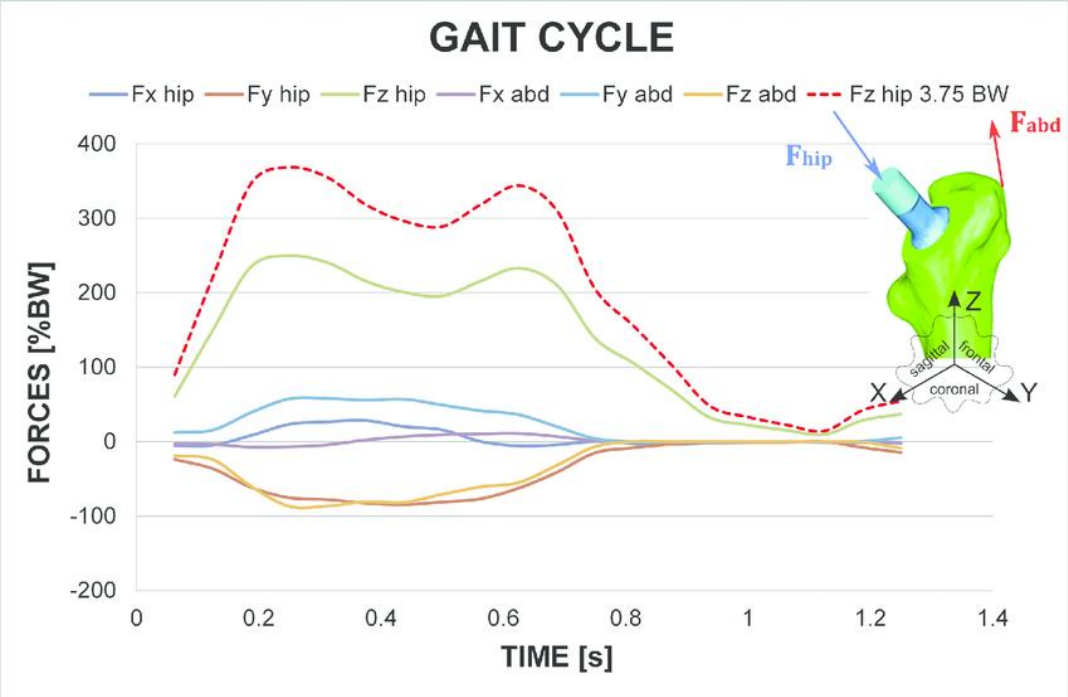

Figure 2.3.1 Graph of the gait cycle. Retrieved from [18].

CHAPTER 3: Physical Examination of the Failed Device

3.1 Visual and Optical Microscope Examination

This project began with a simple visual examination of the failed device. The purpose of doing this was to catalog the parts and find areas of interest for further, more rigorous examination. The parts were visually inspected and photographic evidence was collected. When examining the fractured surfaces of the nail, there appeared to be ripples across the surface moving from one direction to another and transitioned into a rougher looking texture. There was also some discoloration of the metal along the interior surface of the nail (Figure 3.1.1). When examining the self-tapping helical screw, there was also some discoloration on the outer edge of flutes and along the body of the screw (Figure 3.1.2).

Figure 3.1.1 Close-up photo of the fracture surface.

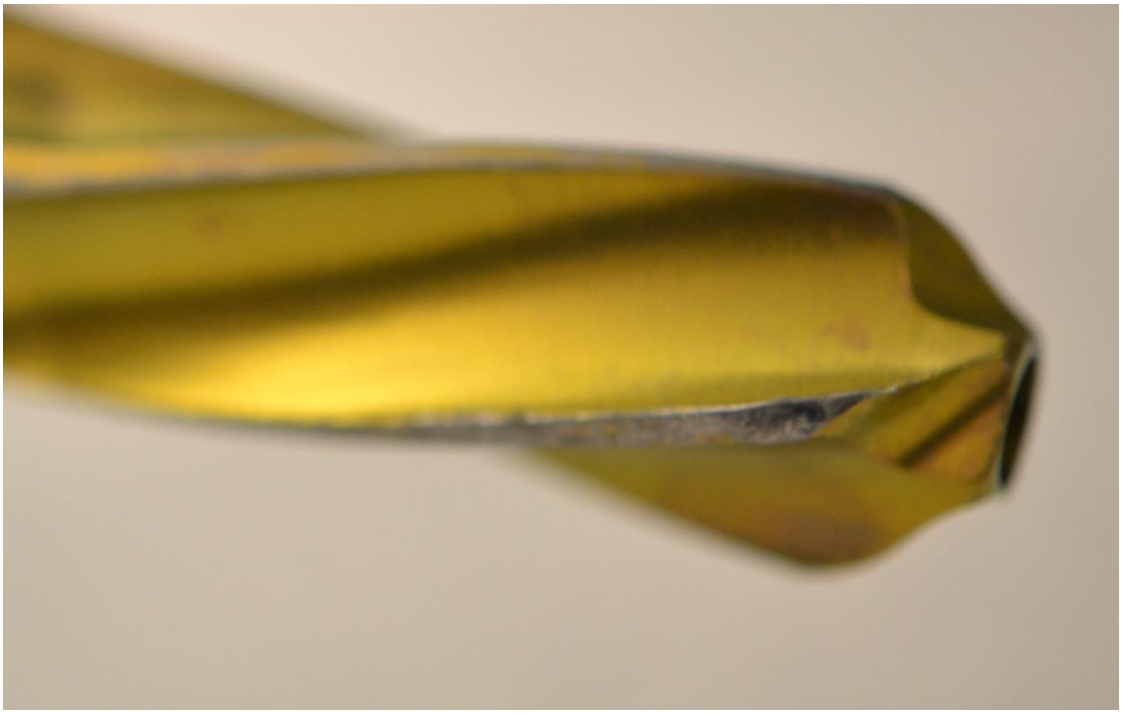

Figure 3.1.2 Close-up photo of the helical screw.

After examining the different parts of the failed femoral nail, there is supporting evidence for the likelihood of several different events. There are some macroscopic features that could be beachmarks. If there are beachmarks, then it is possible that there was some level of fatigue failure. This would mean that failure of the device occurred over some number of cycles arising from walking. Next to the area with rippled surface, there appears to be rougher surface. This could be possible evidence of an overloading failure mode. Lastly there are similar discolorations on the interior of the nail and the self-tapping screw. This could be evidence of the screw scrapping against the nail at the time of insertion. This could be a possible lead on where to find a surface crack if one occurred. With some areas of interest located, it was time to use the optical microscope to assess the damage.

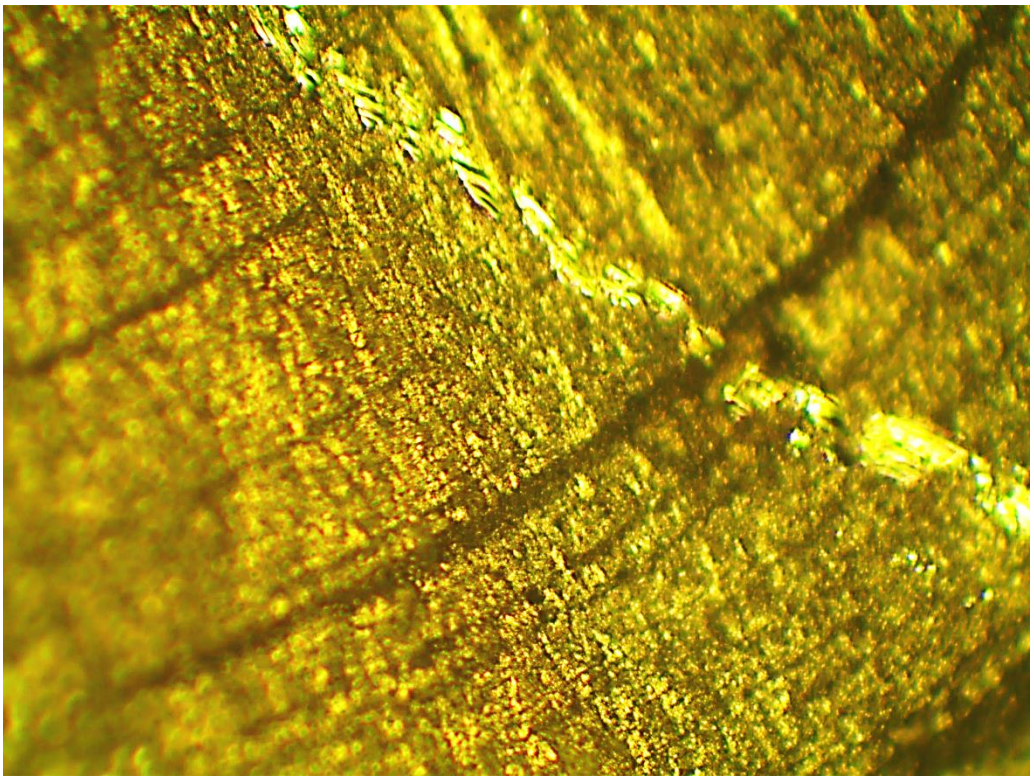

Figure 3.1.3 Benchmarks on the fractured surface under 100x magnification.

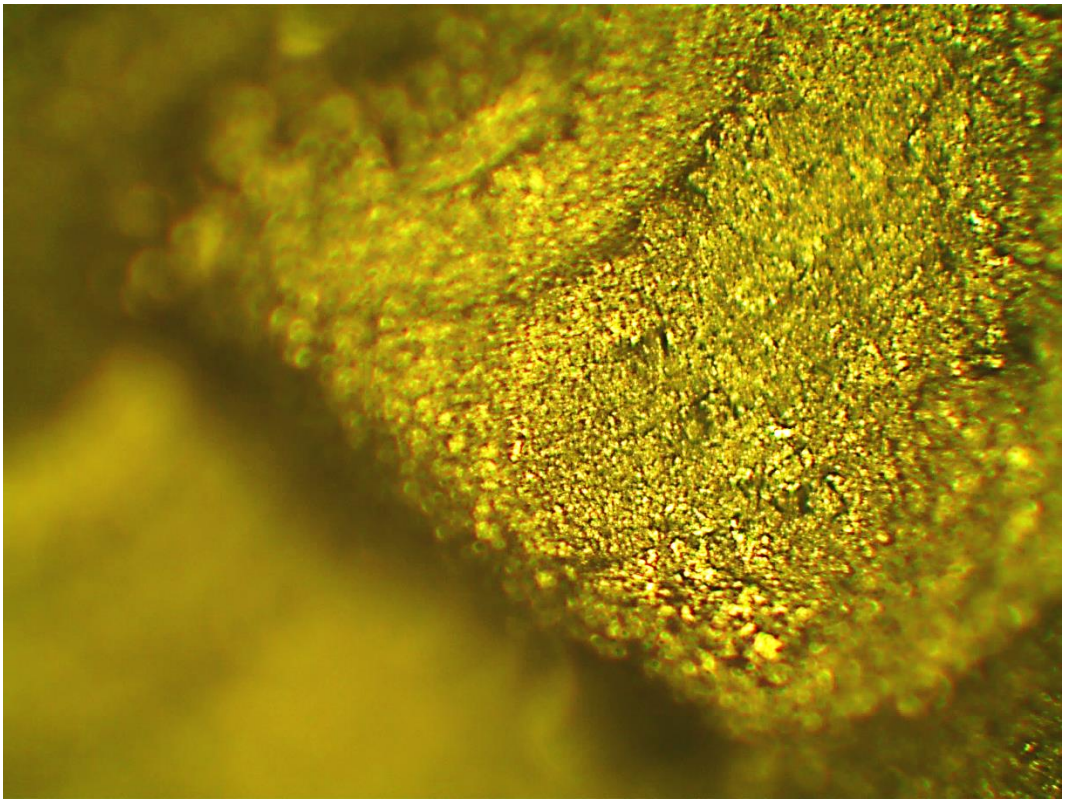

Figure 3.1.4 Rough overload failure area under 100x magnification.

With the aid of an optical microscope, it is possible to see details normally invisible to the naked eye. An optical microscope is an excellent tool for examining the site of failure in order to find detail that can't be easily seen. Such a microscope was used to take the pictures at the failure site on the most proximal portion on the device at 100x magnification (Figures 3.1.3, 3.1.4). At this level of magnification, the macrostructures typical of dimples and beachmarks are very clear. At this point, the evidence was pointing to the likelihood of the device undergoing damage due to mechanical fatigue that eventually led to the device to catastrophically fail from overloading. This evidence alone, however, is not enough to draw definitive conclusions. It is merely one of the many parts that need to be examined that could potentially contribute to the failure of the device.

3.2 Fractographic Examination

3.2.1 Specimen Preparation

In order to perform more extensive examinations of the nail, several specimens were prepared. The parts taken were a 2mm ring from the most distal portion of the nail body and one of the failure surface sections. These specimens would be used for analyzing the material structure of the titanium and failure characteristics examination under SEM. The specimens were cut from their respective areas with the use of an abrasive circular saw. This method was preferred over a typical saw blade due to smaller depth of cut, thus leaving a cleaner cut surface. Before the microstructure analysis could be performed, the ring specimen needed to be polished to a very fine degree. The ring specimen was mounted within a mounting compound making it easier to hold to a grinding wheel. The specimen was held to the grinding for periods of 30 minutes occasionally rotating the piece to assure an even removal of material. This process was performed with increasingly finer grit sandpaper until it was reasonable to believe that the process had diminishing returns on removal of material. Sandpaper alone would not be enough to remove the scratches on the surface that were now nearly invisible to the naked eye. In order to remove the last of the scratches a diamond particle solution was used to further polish the surface to the necessary specifications.

3.2.2 Microstructure Analysis

The Air Force Research Laboratory assisted in the evaluation of

microstructure analysis and examination under SEM. The mounted ring specimen was prepared for microstructure analysis. The purpose of this examination was to determine the percentage of alpha and beta formations within the titanium. The volumes of alpha and beta colonies have an effect in the material properties of the titanium alloy [14, 54]. By measuring the alpha and beta structures, it can be determined if the material in the failed nail conformed to ASME F620-00 and ASTM F2066-18 standards [63, 64]. The ring specimen was examined under SEM and electron backscatter diffraction (EBSD) examinations was performed. Pictures of the surface of the specimen were taken at 2000x and 7000x magnification. The pictures taken show the titanium is made up of mostly beta-phase with some intergranular alpha-phase (Figures 3.2.2.1, 3.2.2.2). When analyzed for volume, the pictures showed the titanium to be 70.6825% beta-phase. For implantable titanium nails of this kind it is typical that they are majority beta phase [32].

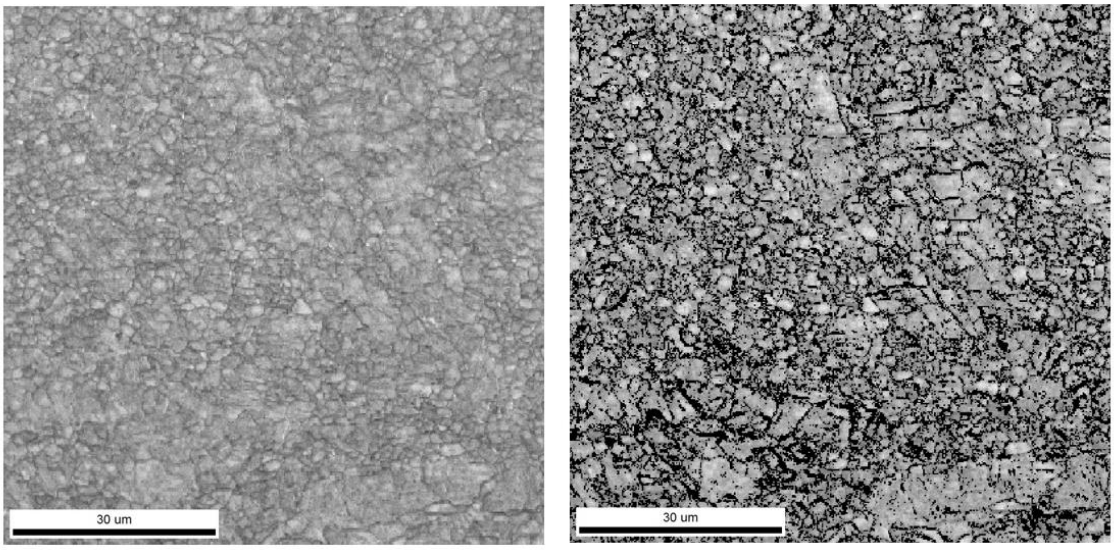

Figure 3.2.2.1 Alpha plus beta (left) and beta only (right) microstructures.

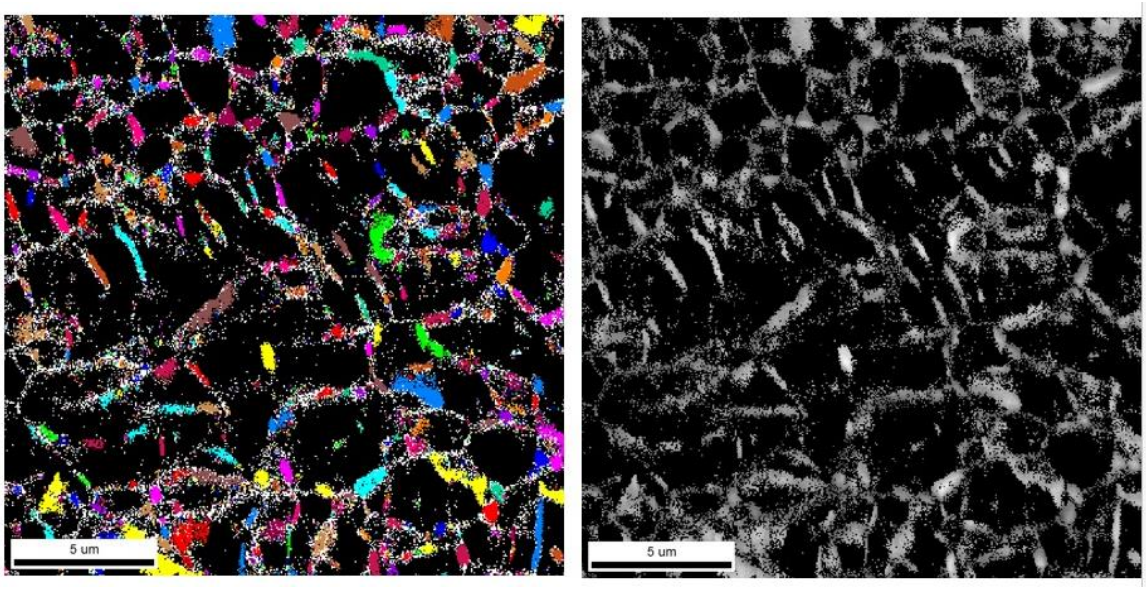

Figure 3.2.2.2 Alpha only microstructures for Ti-15Mo.

3.2.3 Scanning Electron Microscopy

For the next level of examination, the failure area needed to be examined under SEM to better see the details of the fracture surface. The specimen was mounted and a small portion was coated with Silver (Ag) paint. This allowed the electrons a means to discharge from the specimen to the mounting stud so that the SEM could see the surface. The specimen was loaded into the SEM and several areas selected for scanning at different levels of magnification (Figure 3.2.3.1). From these photographs, we can see the striations characteristic of crack propagation within the device (Figure 3.2.3.3). The striations were measured and found to have an average length of 0.689 micrometers. There is also the presence of overloading failure characteristics in areas that were not obvious when examining under the optical microscope (Figure 3.2.3.3).

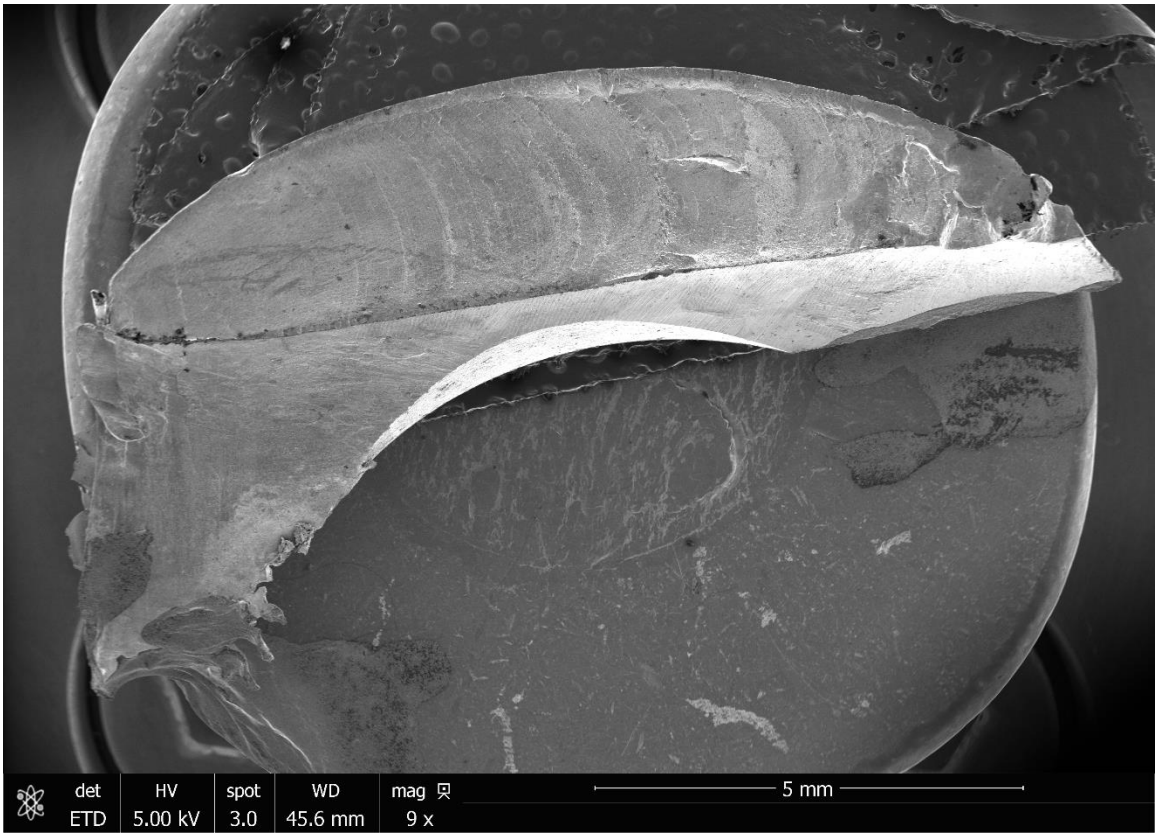

Figure 3.2.3.1 Overview of the fracture surface under SEM.

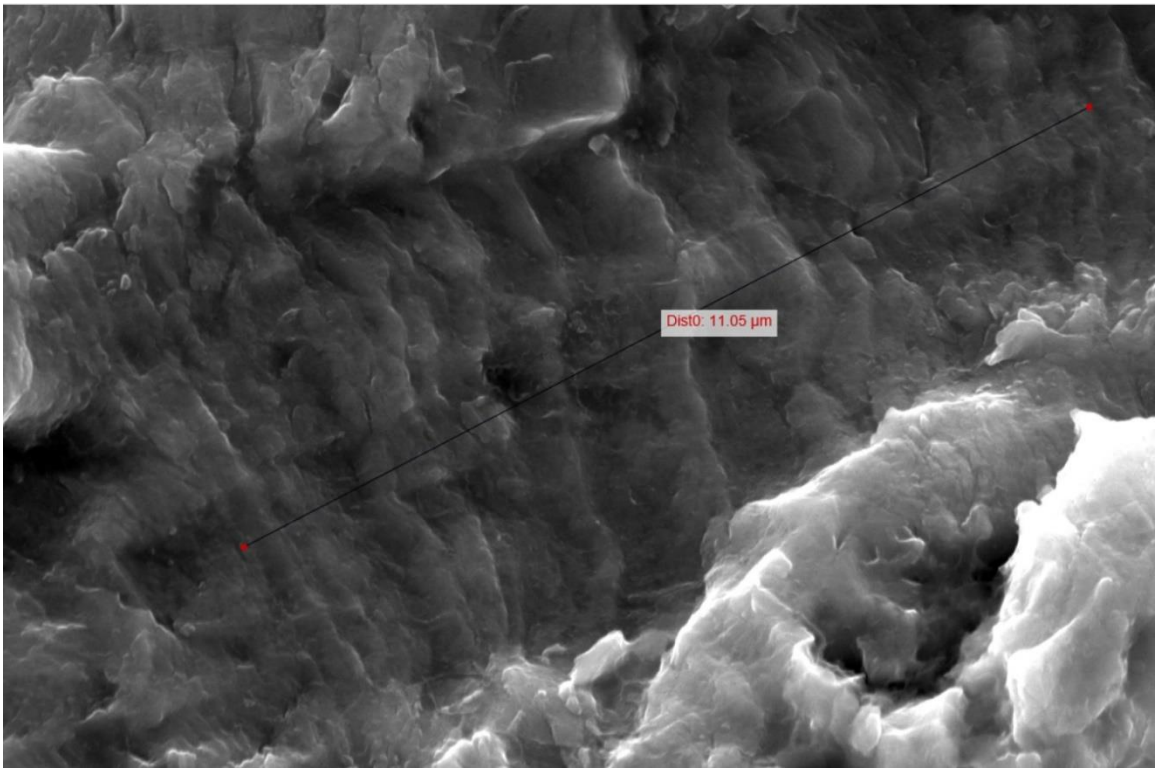

Figure 3.2.3.2 Measurements of striations at 7,000x magnification.

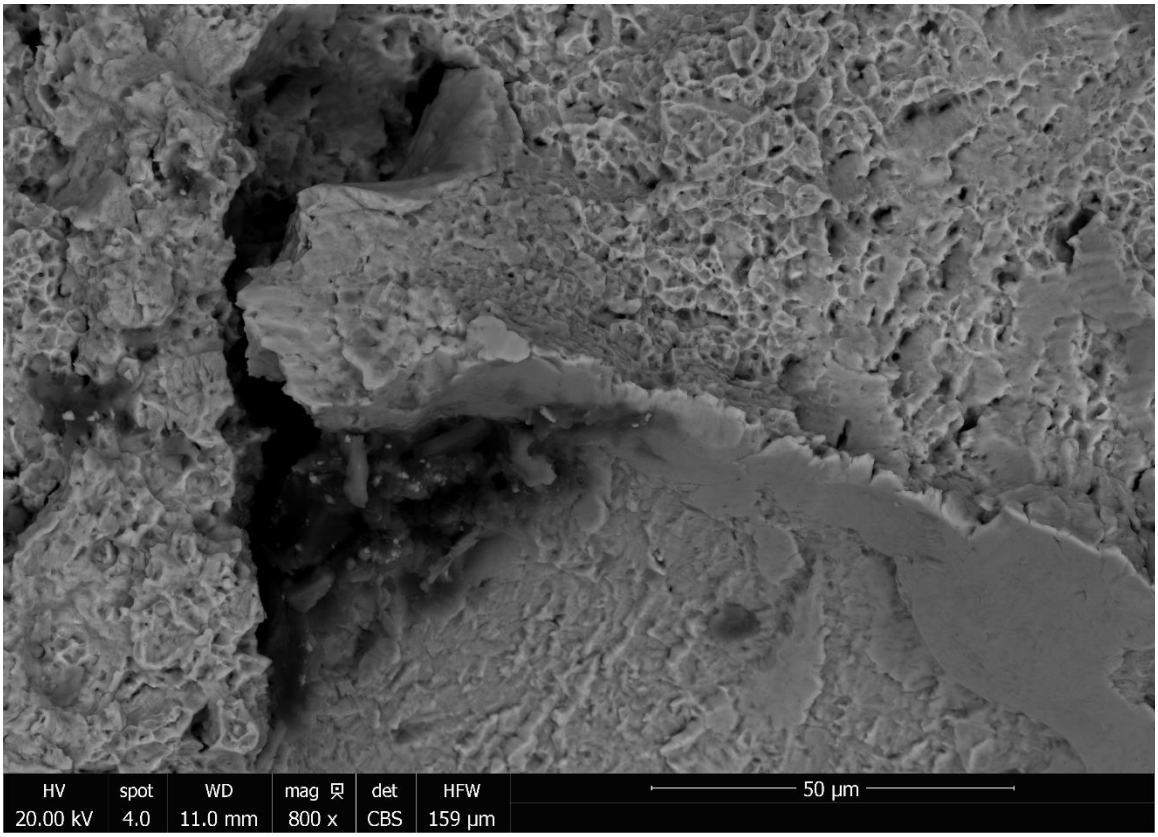

Figure 3.2.3.3 Overloaded failure are under 800x magnification.

3.3 Material Conformity

The last portion of evidence that needed to be collected was to determine the chemical characterization of the failed nail. For the material to perform per specifications, the titanium alloy needed to meet certain chemical criteria. The chemical characterization was collected by performing energy-dispersive X-ray spectroscopy (EDS) on the failed nail. Information was gathered from several different areas from the fracture surface and distal sample (Figure 3.3.2-3.3.4). When compared to ASTM standards (Figure 33.1) [63] the material the titanium alloy appears to be missing key chemical components. None of the examined areas met the requirements for the necessary amount of titanium or molybdenum. There is also

an abundance of Carbon among the sample area, far more than what standards allow. The missing components could cause the material to exhibit different mechanical properties than what the expected values given in the standard. If the material is weaker then this could be a contributing factor to the premature failure of the device.

Table 3.3.1 ASMT F2066-18 Chemical Requirements

Element	Composition, %, (Mass/Mass)
Nitrogen, max	0.05
Carbon, max	0.10
Hydrogen, max	0.015
Iron, max	0.10
Oxygen, max	0.20
Molybdenum	14.00-16.00
Titanium	Balance

Table 3.3.2 Comparison of EDS

	Required %	Area 1	Area 2	Area 3
Carbon	0.10 max	4.74	6.42	40.82
Molybdenum	14.00-16.00	8.61	6.25	-
Titanium	83.535 min	69.11	67.68	12.21

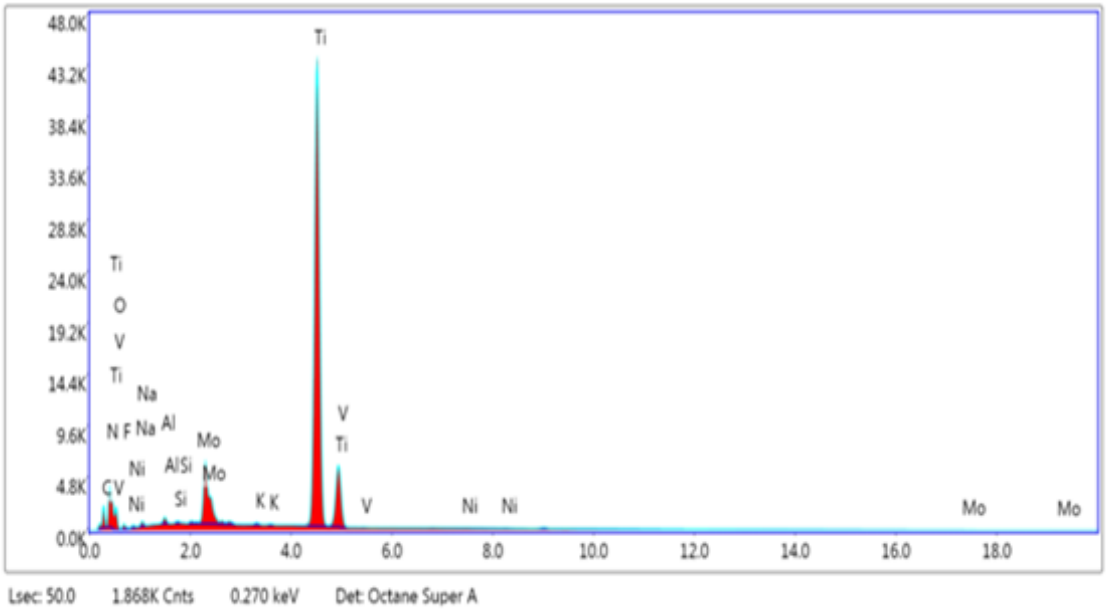

Figure 3.3.1 EDS results for area 1.

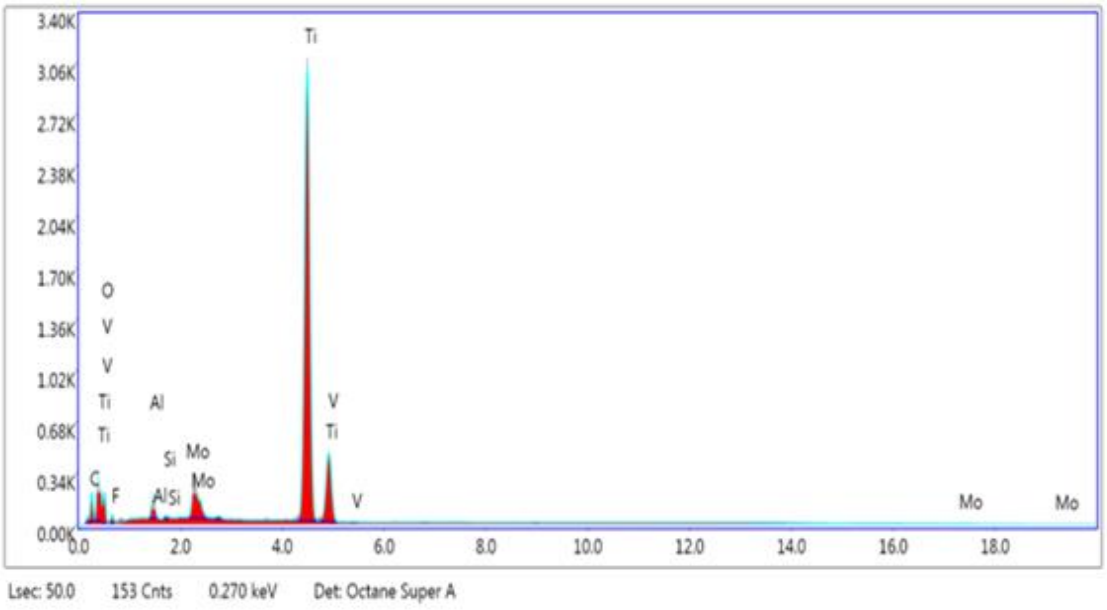

Figure 3.3.2 EDS results for area 2.

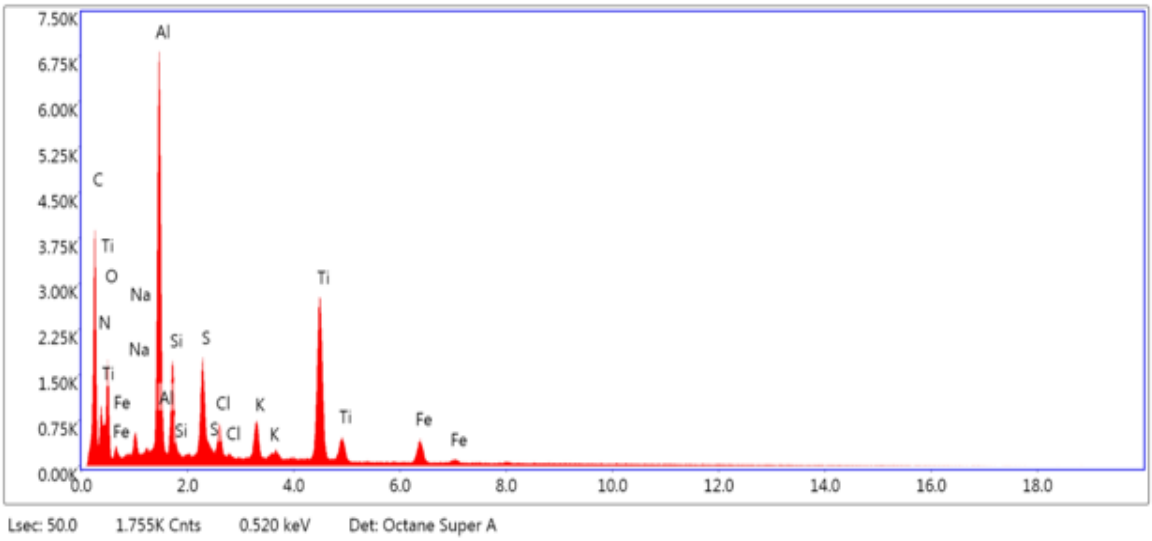

Figure 3.3.3 EDS results for area 3.

CHAPTER 4: FINITE ELEMENT ANALYSIS

4.1 Construction of 3D Experimental Models

4.1.1 Designing the Nail and Screw Models

Three-dimensional models of the intramedullary femoral nail and helical screw were constructed using SolidWorks software. These models would be later imported in ANSYS Workbench to simulate different loading scenarios to test how stress is developed during loading under different boundary conditions. The models for the intramedullary nail and helical screw were generated using a combination of dimensions taken from DePuy Synthes brochures and measurements from the failed device [12]. Serial number information on the side of the both the intramedullary nail and helical screw matched with specific models found within the brochures. This information yielded details important to recreating the nail such as the original length, curvature of the nail, and angle of helical screw relative to the nail body. The information within the brochures were, however, not enough to recreate every detail necessary. Measurements were taken from the intramedullary nail in order to ascertain missing details needed to complete accurate three-dimensional models (Figures 4.1.1.1, 4.1.1.2).

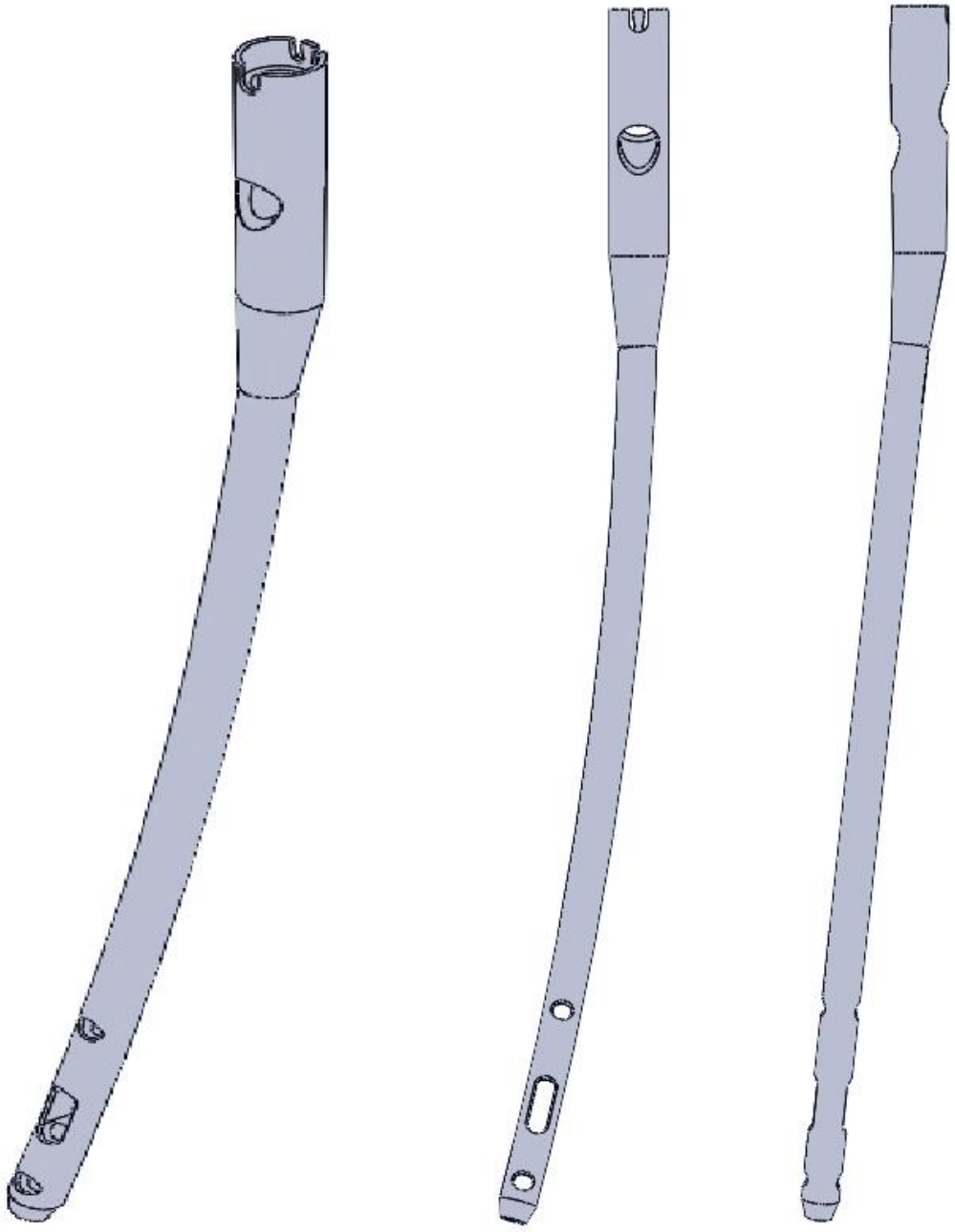

Figure 4.1.1.1 Generated model for the femoral nail.

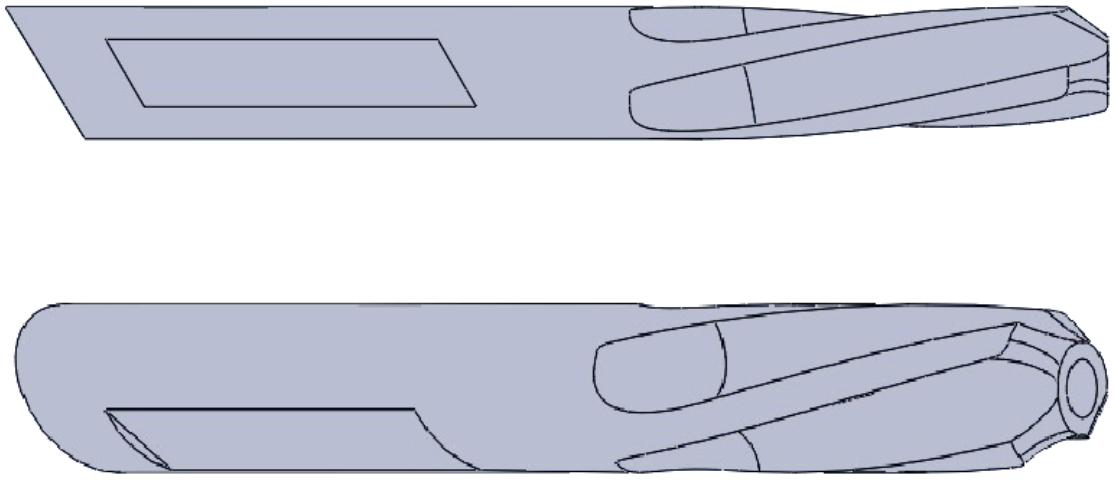

Figure 4.1.1.2 Generated model for the helical screw.

4.1.2 Designing the Femur Models

For this experiment, a set of adult femur models were generated using Mimics Research 19.0 and 3-matic Research 13.0 software. These models included a normal adult femur as well as femurs modified to simulate various types of hip fractures. These models would later be combined with the intramedullary nail and helical screw models in order to construct a realistic loading environment for the nail during finite element analysis. The process of generating the femur models began with acquiring a computerized tomography (CT) scan of an intact adult right femur. The Mimics software uses information imbedded within the CT scan in order to generate masks across hundreds of layers of X-rays images in all three dimensions. These masks are areas of interest that, when compiled, can generate solid three-dimensional models. The software can auto-generate these masked based on selected range of Hounsfield units (HU) making it much easier to select the bone tissue from the other body tissue. In order to create a model for the femur manual editing, of the mask was

necessary to remove the other bones from the selection and fix portions of the femur that didn't register well in the CT scan due to their low density.

After the masks are compiled into a single femur model, the model is them imported into 3-matric software for mesh generation and editing models for special conditions. Generating a mesh is the process of mapping the surface of a three-dimensional object. The mesh is comprised of hundreds to tens of thousands of triangular faces depending of the complexity of the object. These triangular faces are the elements that interact with one another within a computer simulation. Before the mesh was generated the femur model was smoothed in order to reduce the number of irregular features and reduce the overall number of generated faces. After the mesh generation, three copies of the femur were created. From these copies, the femurs with different types of common hip fractures were developed. The three hip fractures chosen to simulate are intracapsular, intertrochanteric, and subtrochanteric fractures [26] (Figures 4.1.2.2-4.1.2.4). This process was accomplished by first mapping paths for the different fracture along the surface mesh. This path is then used to make a sweeping cut around the features of the femur removing one millimeter of material from the surface. The mesh is then regenerated creating models simulating fractured bones.

With the meshes generated, the models were them imported back into Mimics in order to generate realistic material behavior for the femurs. Unlike the intramedullary nail, human bones demonstrate anisotropic material properties. This means the material properties are not uniform and change depending on the area where the load is applied. This is due to the fact the density of the bone is different

depending on the area [58]. Another contributing factor is that long bones, like the femur, are made up of different types of bone tissue which have their own material properties [58]. Equations for the modulus of elasticity and Poisson's ratio were assigned to the femur and distributed over the bone corresponding HU values [28]. By doing this, the model femurs can display accurate material behavior under load in the simulations.

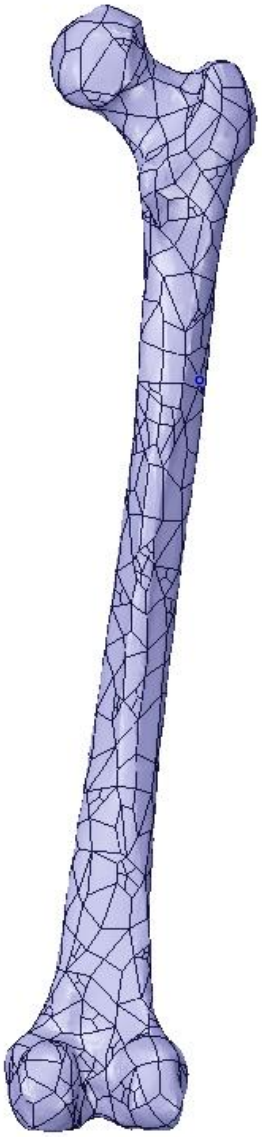

Figure 4.1.2.1 Generated model of an adult right femur.

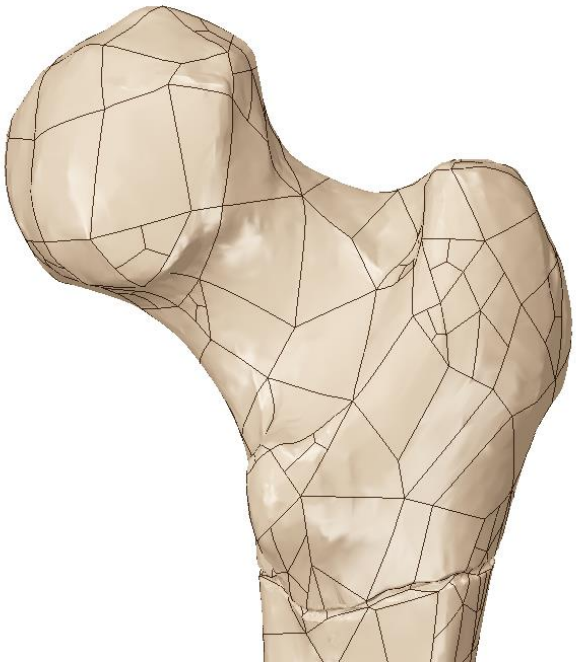

Figure 4.1.2.2 Femur model with a Subtrochanteric fracture.

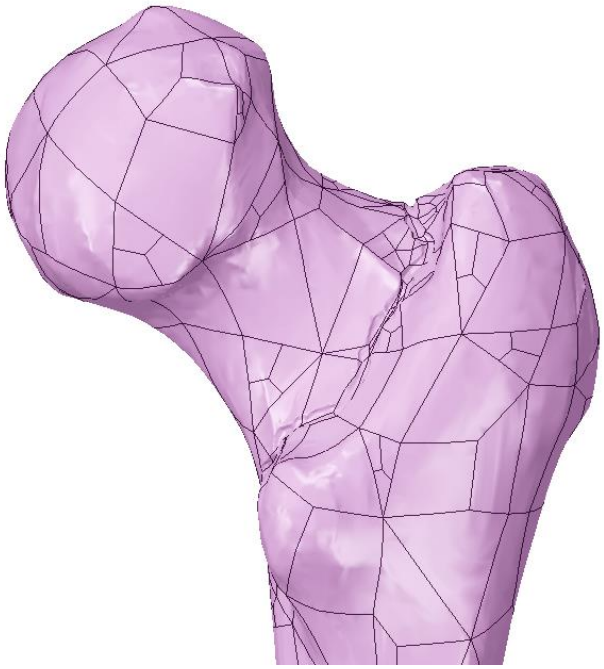

Figure 4.1.2.3 Femur model with an Intertrochanteric fracture.

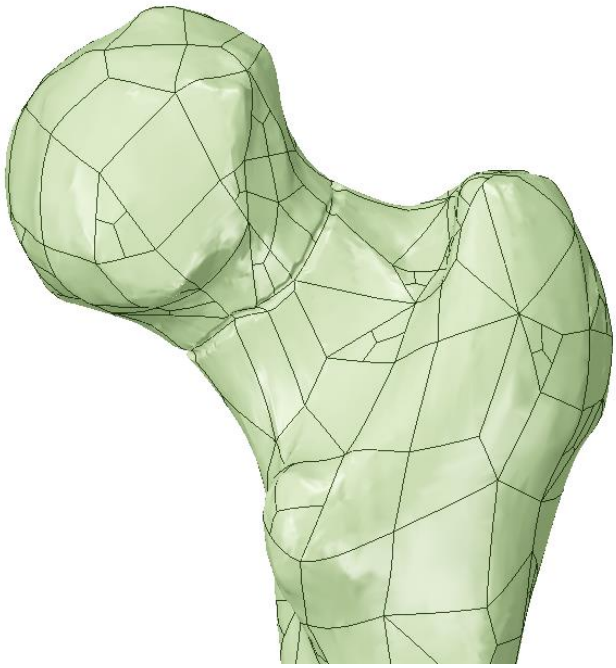

Figure 4.1.2.4 Femur model with an Intracapsular fracture.

4.2 Finite Element Analysis

With the models for all the components finalized, the process of finite element analysis could be performed. The models for the intramedullary nail, helical screw, and femurs were imported into ANSYS Workbench for simulation. Before the simulations could be performed, material properties needed to be assigned to the intramedullary nail and helical screw and boundary conditions assigned to all the models so that the software could capture how models interacted with one another. The material properties assigned to the device parts were those of the titanium alloys Ti-15Mo and Ti-6Al-7Nb in accordance to ASTM F2066-18 and ASTM F1295-05 standards, respectively [63, 62]. For the simplified models of the femur, the cortical and cancellous portions were assigned a modulus of elasticity of 12.7 GPa and 0.9 GPa, respectively, and a Poisson's ratio of 0.3 and 0.2, respectively, [24, 29, 61]. For these simplified models, the material properties of the bone were treated as

homogeneous and isotropic.

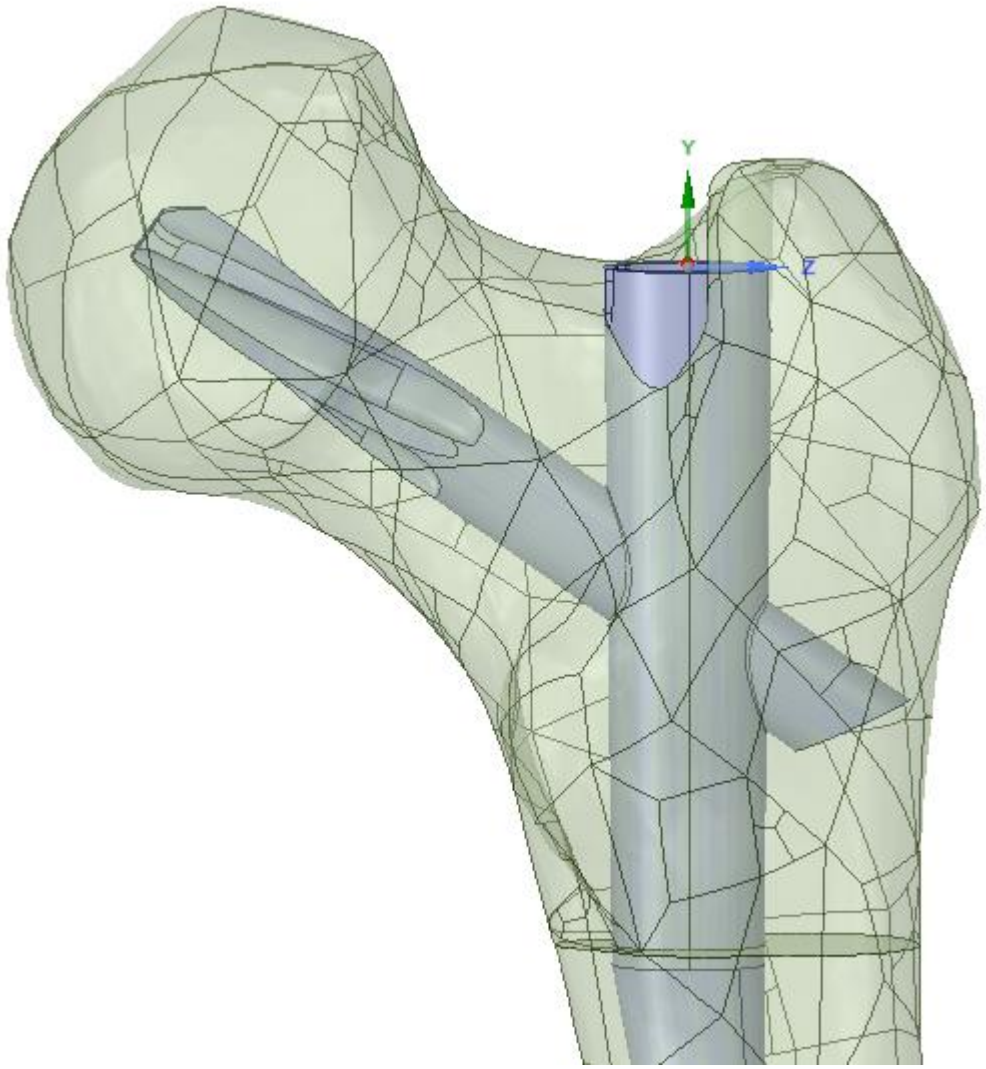

Figure 4.2.1 Femoral nail positioned within the femur model.

Using editing software in ANSYS, the physical relationship between the device part and femur were established (Figure 4.2.1). The nail and screw were placed inside the femur such that the helical screw was aligned with the femoral neck and the tip of the screw was near the center of the femoral head. The intramedullary nail and helical screw were configured such that the axis of screw model aligned with the axis of cylindrical shaft on the nail that houses the screw when it is in the body. The

models were adjusted so that the long body of the nail fit as close to the center of the long portion of the femur as possible without moving the other boundary relationships. The regular femur was divided into three sections (Figure 4.2.2). This was done so the different sections of the bone could be assigned material properties representative of each section. In addition to this, the intracapsular and Intertrochanteric fractured femurs were given an additional division in a plane along their fractured surfaces. This was done so a coefficient of friction could be added between the fractured parts of the bone. With the geometry defined, the numerical portion of FEA could be performed.

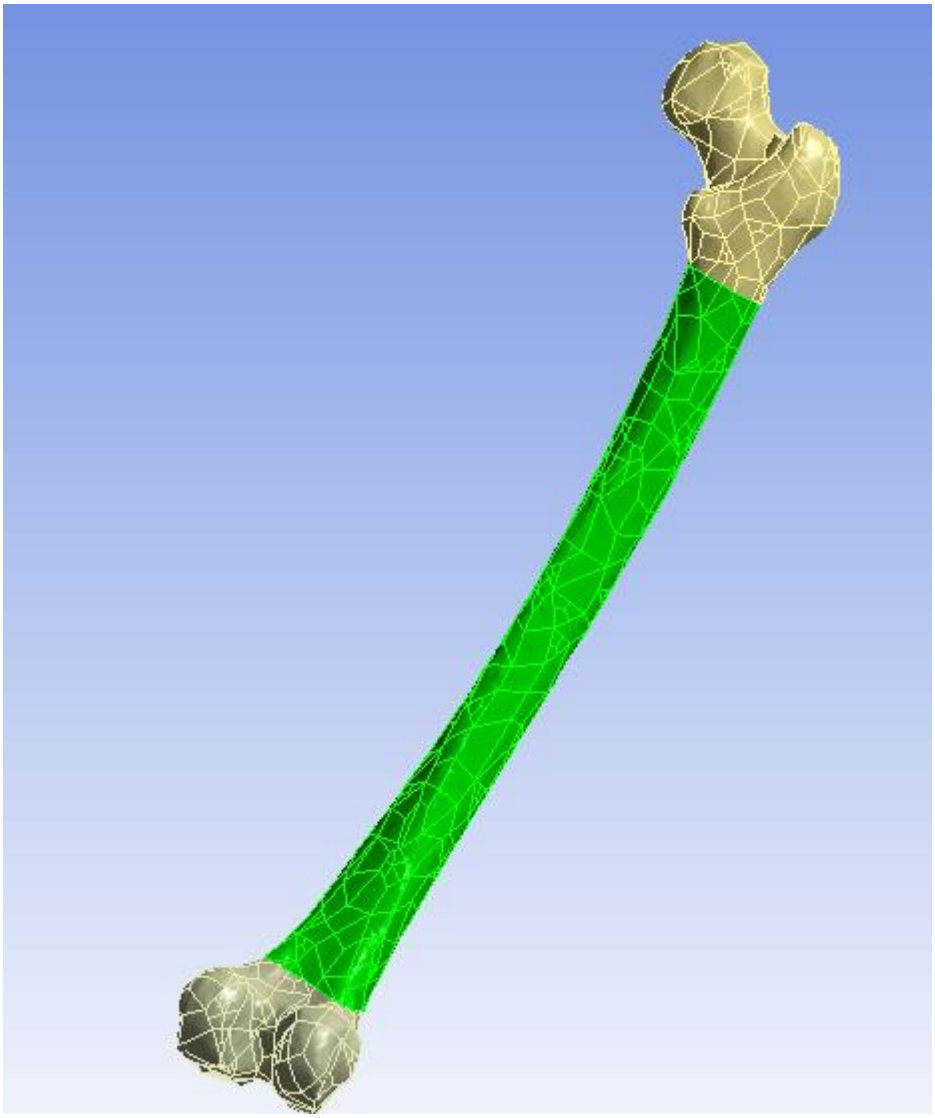

Figure 4.2.2 Femur model divided into three sections based on material properties.

For the finite element analysis, the four femur models underwent three different loading scenarios. These scenarios were a ramped compression load, ramped compression load with added torque, and the gait cycle. The purpose of performing the two compressions tests was to find the amount of force needed to make the nail fail. By finding the load in which the nail would fail, we can assess the likelihood of this event occurring under normal use. The last loading scenario was performed to ascertain the stress forces occurring during the gait cycle. This would be useful to

understand if the forces were present for mechanical fatigue to occur. Before the simulations could be run, all the boundaries needed to be defined and meshes for the models generated. The number of nodes and elements generated during meshing are listed in Table 4.2.1.

Table 4.2.1 Number of nodes and elements per femur model.

	Number of Nodes	Number of Elements
Normal	24317	13154
Subtrochanteric	27783	15254
Intertrochanteric	52461	29053
Intracapsular	48945	26967

Friction coefficients were defined between the different bodies. The friction coefficients between the nail and the screw and the device and bone were defined as 0.35 and 0.4 respectively [24] (Figure 4.2.3). For the femurs with fractures, a coefficient of 0.4 was given between the fracture surfaces [35, 36] (Figures 4.2.4-4.2.6). The parts of the femur that were divided for the purpose of assigning them different material properties were considered to be bonded.

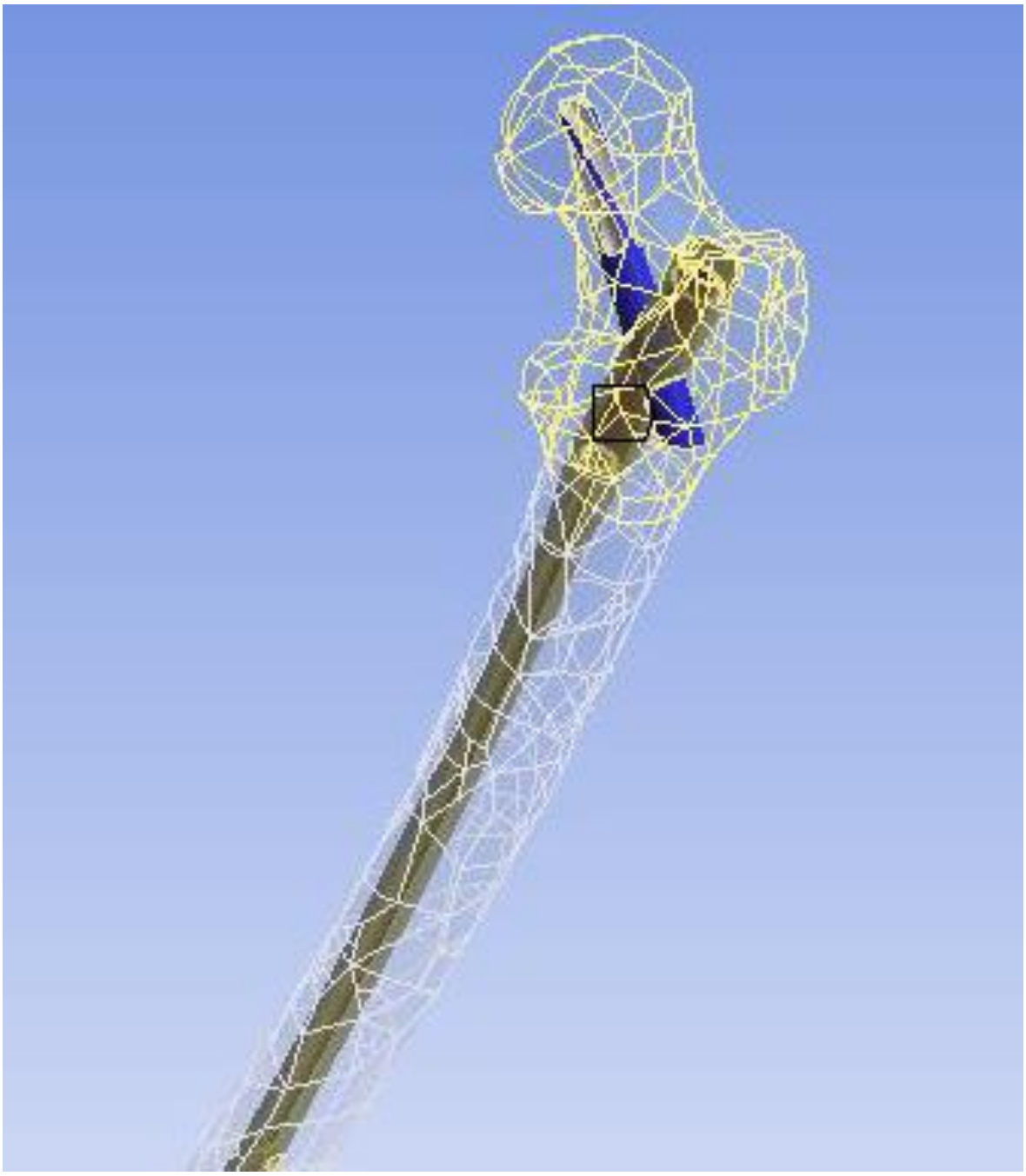

Figure 4.2.3Frictional boundaries between the nail and screw.

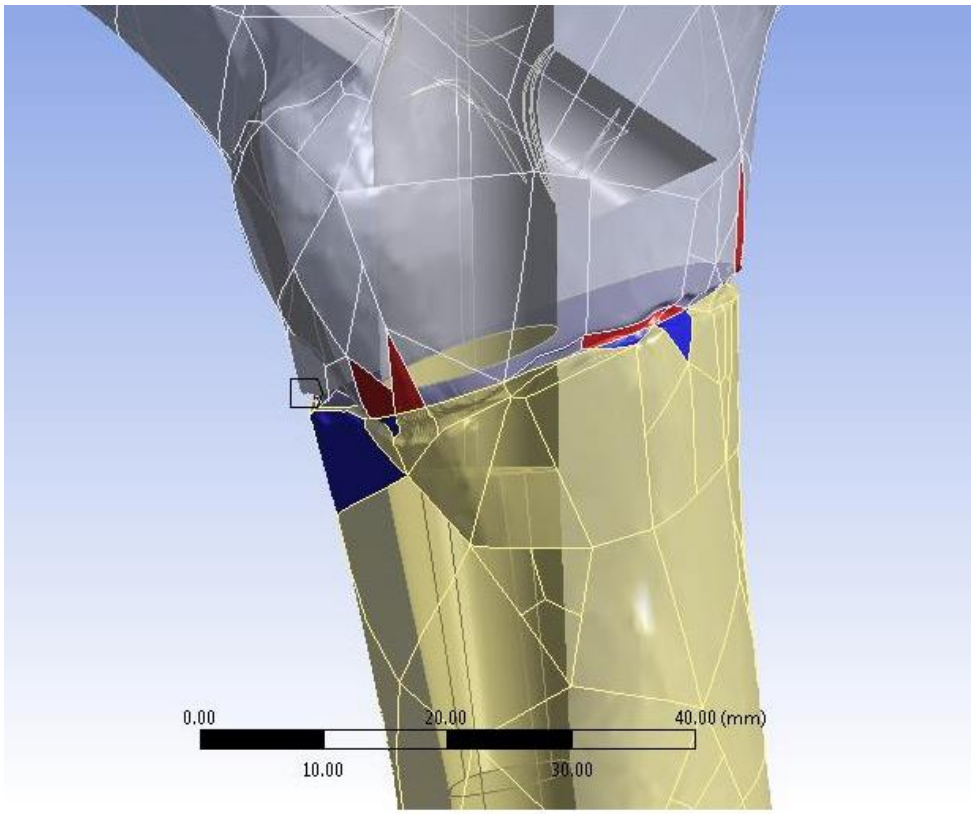

Figure 4.2.4 Frictional boundaries between Subtrochanteric fracture.

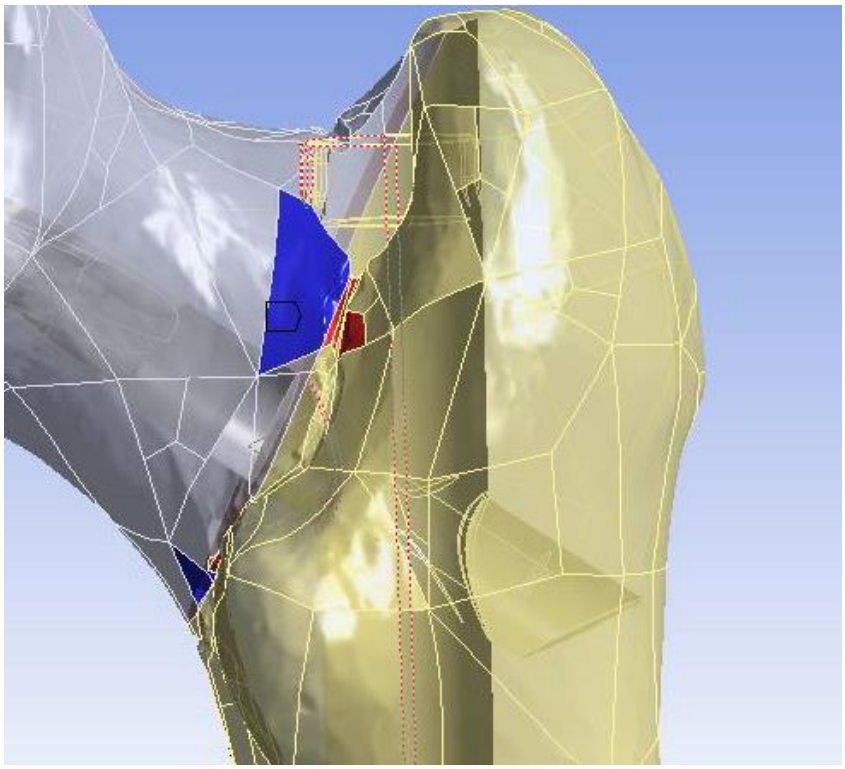

Figure 4.2.5 Frictional boundaries between Intertrochanteric fracture.

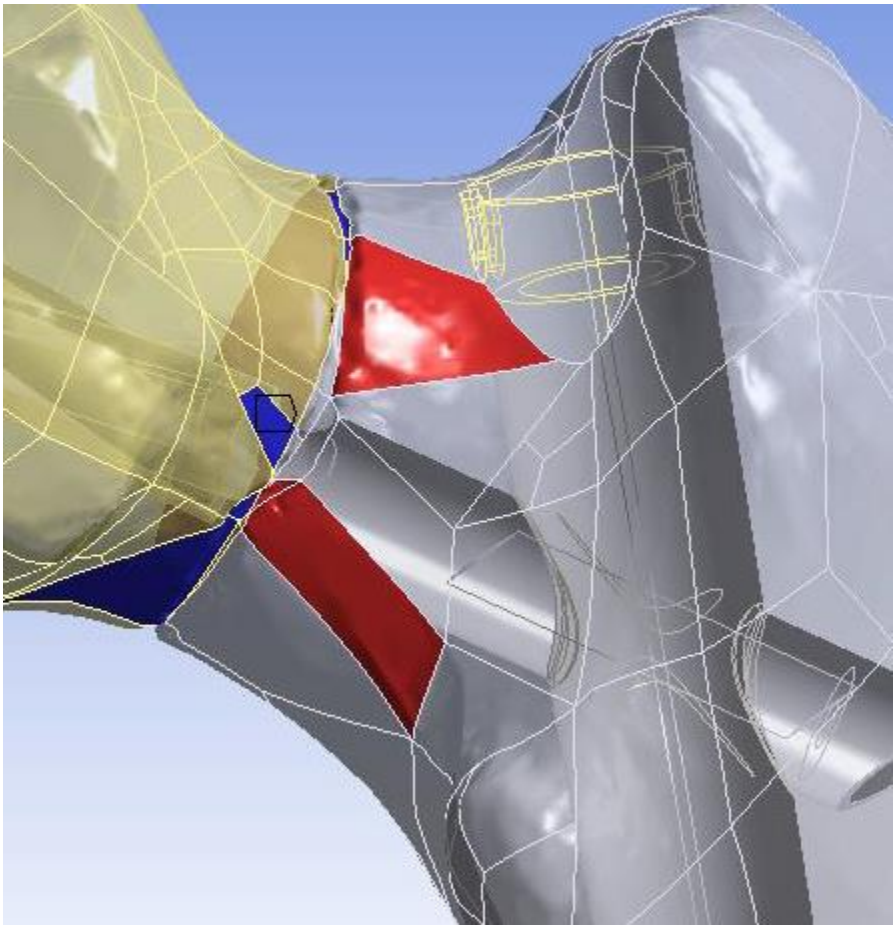

Figure 4.2.6 Frictional boundaries between Intracapsular fracture.

The models were restrained by considering the most distal partition of the femur to be in contact with a fixed support (Figure 4.2.7). For the compression only test, the femur was loaded on the top of the femoral head in the negative y-direction [35, 36] (Figure 4.2.8). Loads applied to the femur were between 500N-4500N in 500N increments over a period of nine seconds (Figure 4.2.8). For the solutions, ANSYS was configured to collect data for equivalent stress, total deformation, equivalent elastic strain, and shear stress. The simulations were allowed to run and the data collected. The data would be later entered into JMP Pro 13 statistical analysis software for comparison.

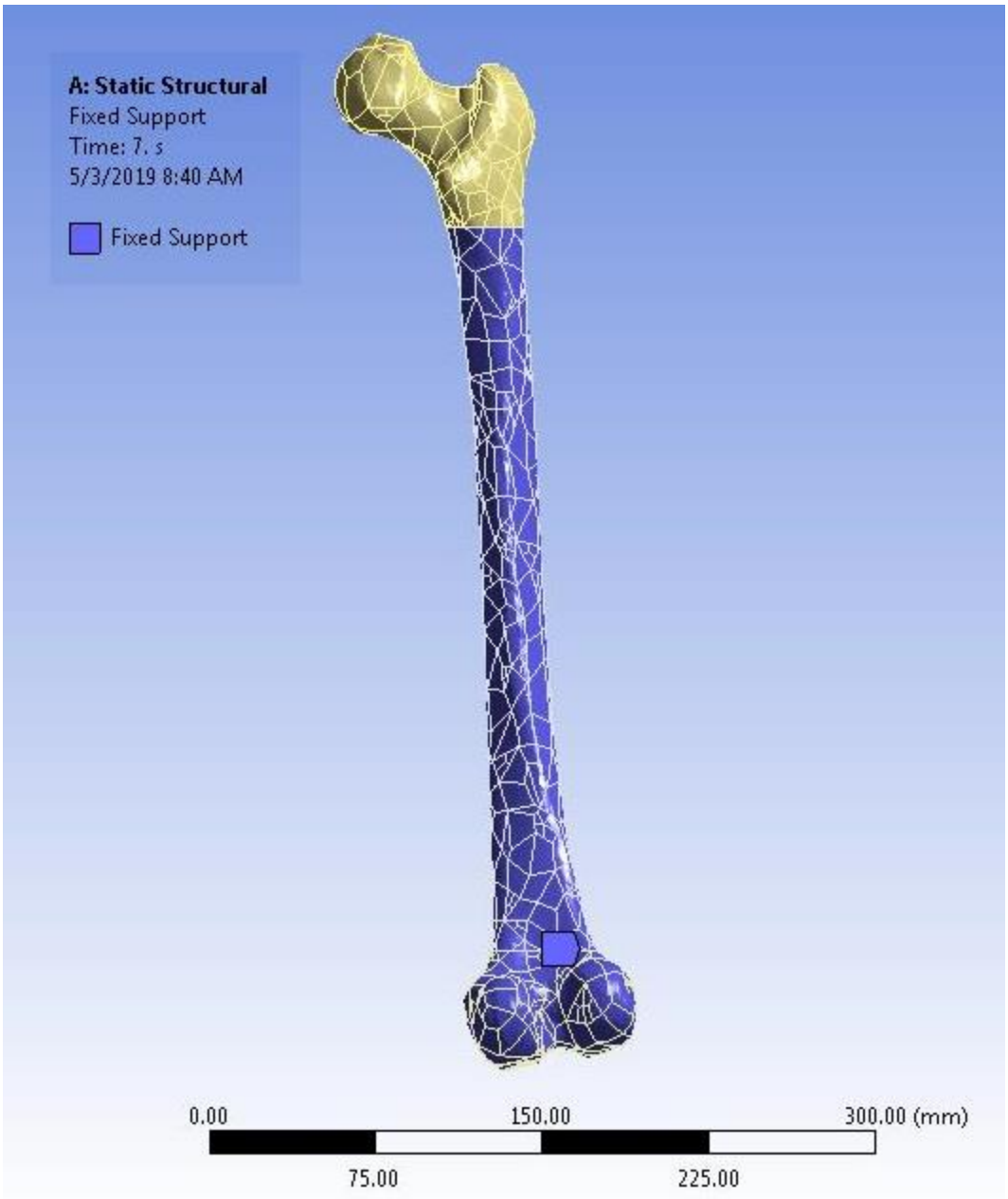

Figure 4.2.7 Fixed support boundary defined on the distal portion of the femur models.

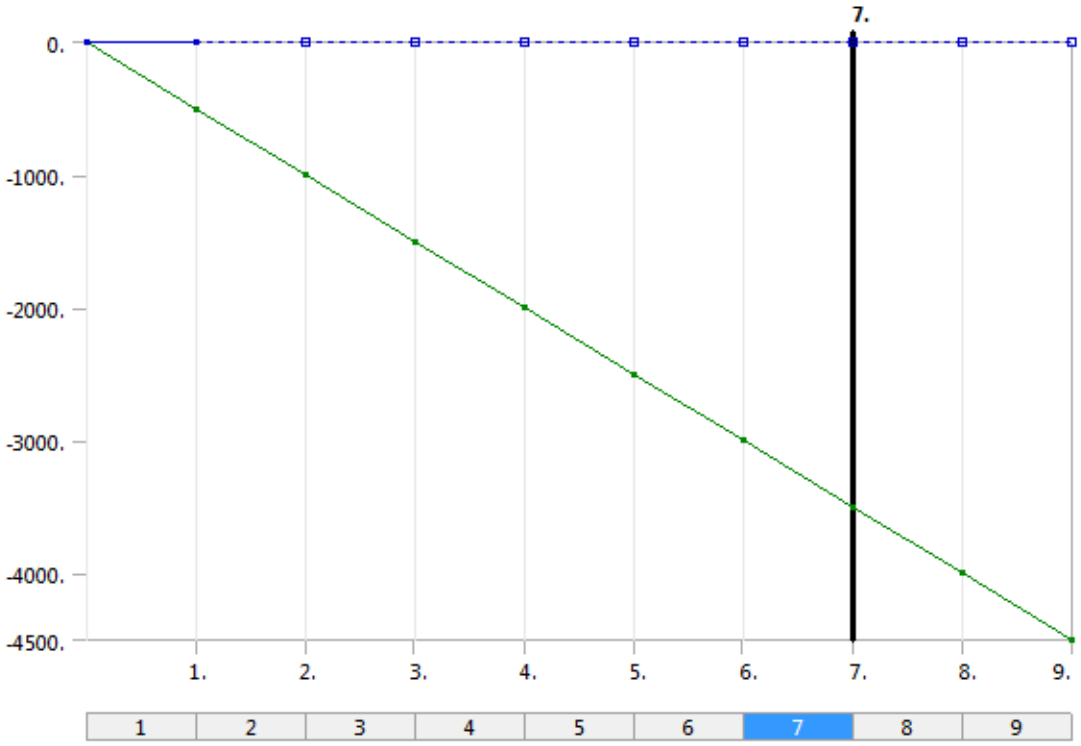

Figure 4.2.8 Application of compressive load to proximal femur.

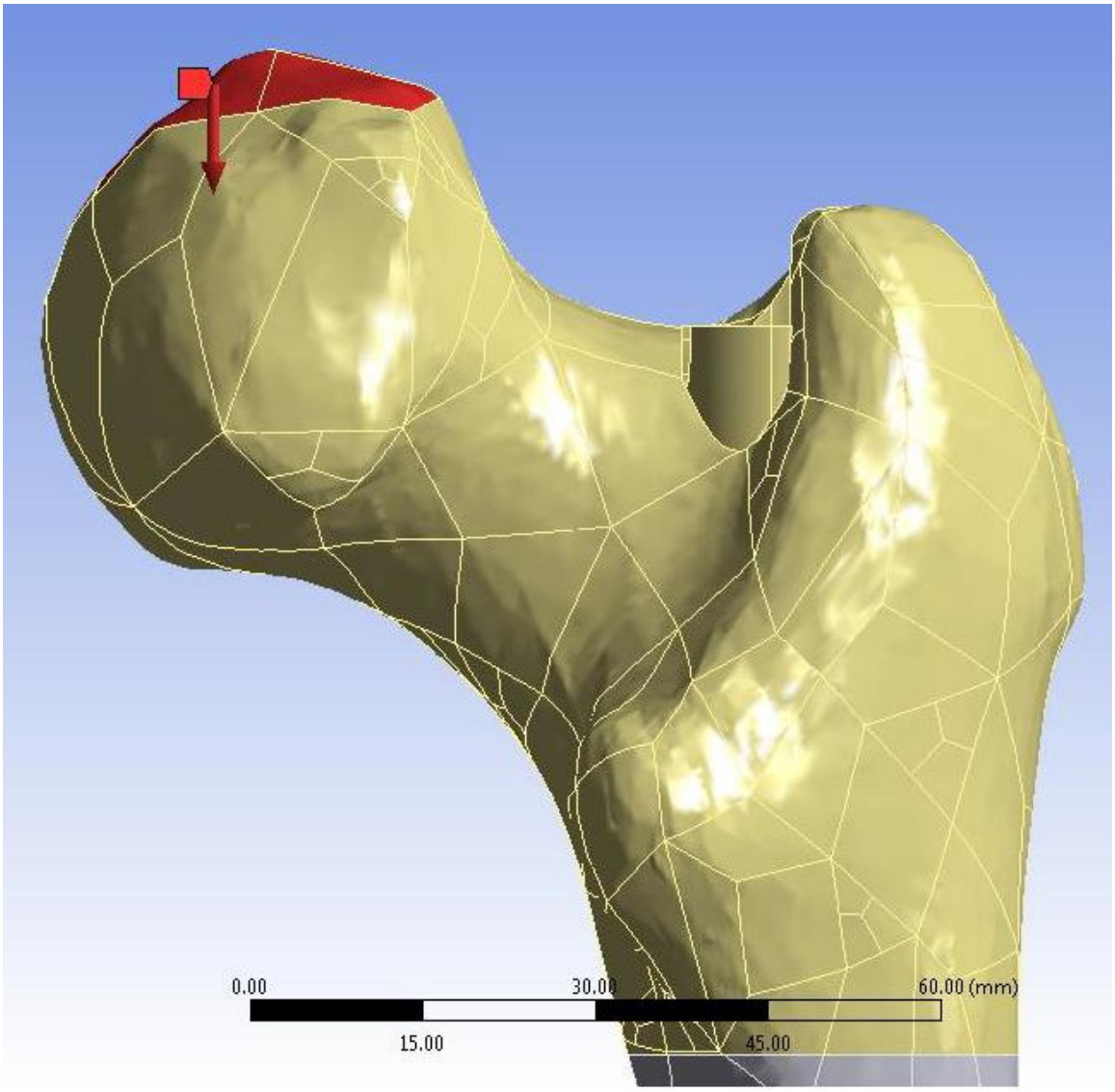

Figure 4.2.9 Compressive forces loaded on the head of the femur.

For the tests of combined compression and torque to failure, the setups for the boundary conditions for the models were nearly identical. Both the fix support and compressive forces were applied the same as before. In addition to these, a bending moment was applied to the body of the nail (Figure 4.2.10). This rotational force ranged from 5Nm-45Nm increasing by 5Nm per step (Figure 4.2.11). With this setup, the simulations were allowed to run collecting the same types of data as the compression only tests.

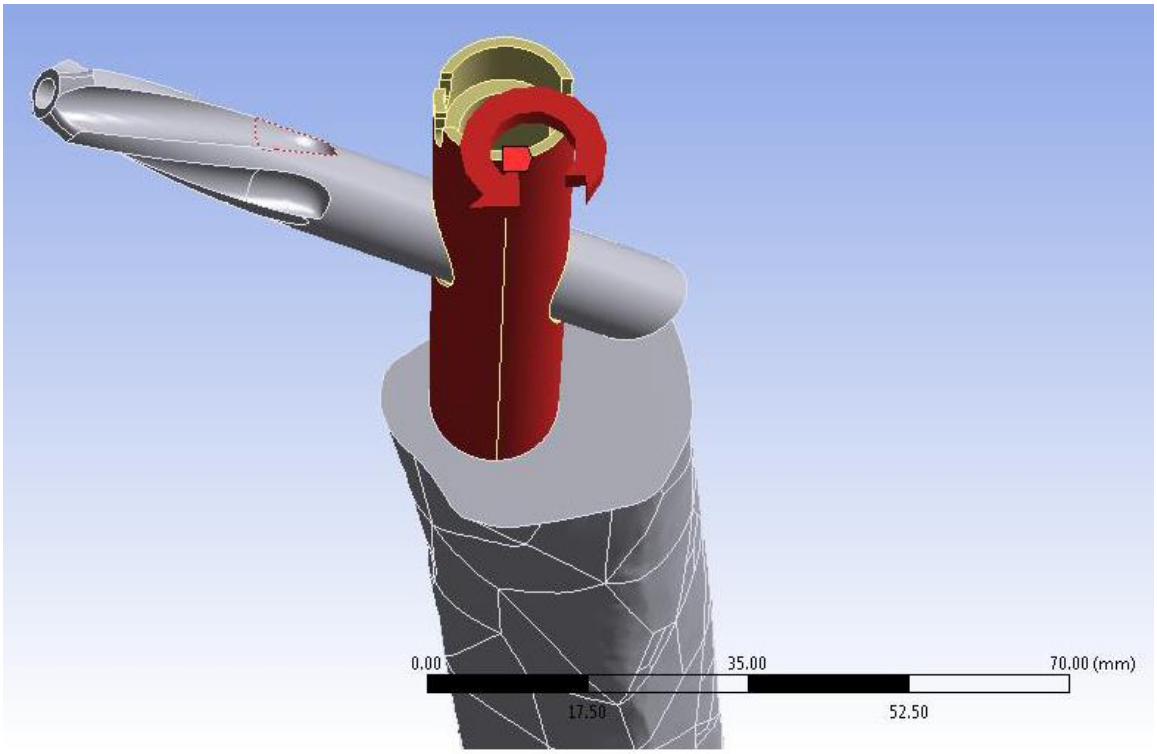

Figure 4.2.10 Bending moment applied to the body of the nail.

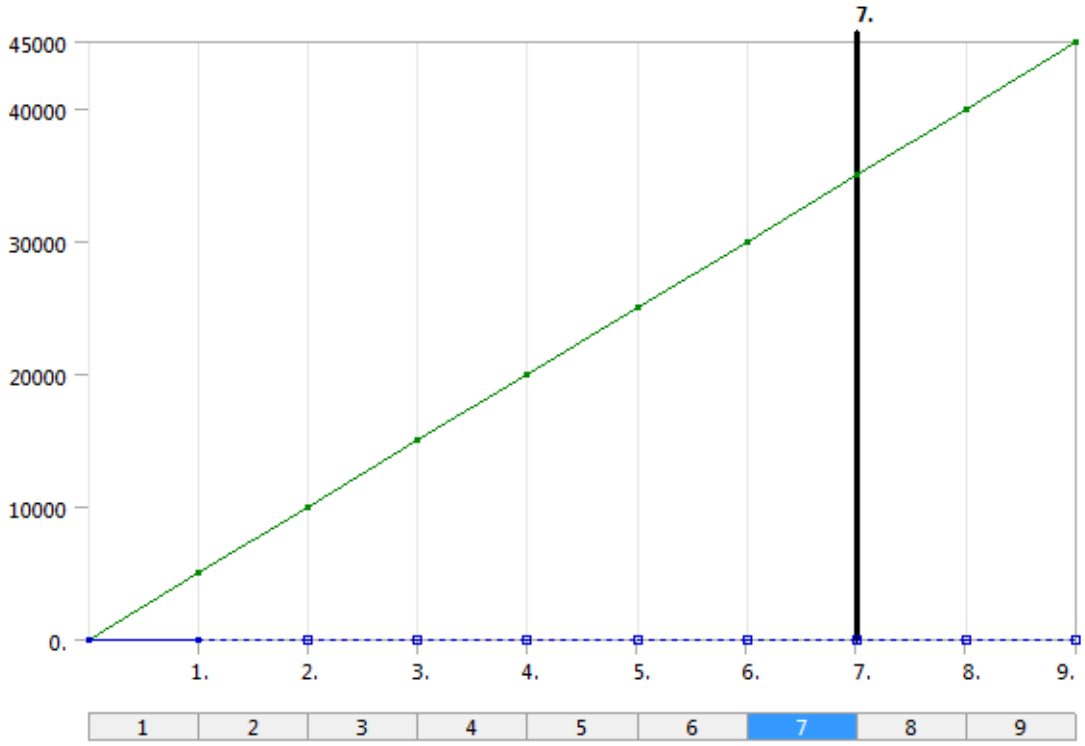

Figure 4.2.11 Bending force applied to nail body.

The last type of tests run measured the effects of the gait cycle on the nail. The applications of forces for this set of tests were very different from the previous test in that gait forces are three dimensional forces. Every step the program takes has a different force in the x, y, and z directions. To reflect this difference, the target area for the allied force was expanded to the whole femoral head (Figure 4.2.12). The tests were set to run for 60 steps over the course of 2.069 seconds (Figure 4.2.13). The simulations were allowed to run and the data were collected for statistical analysis.

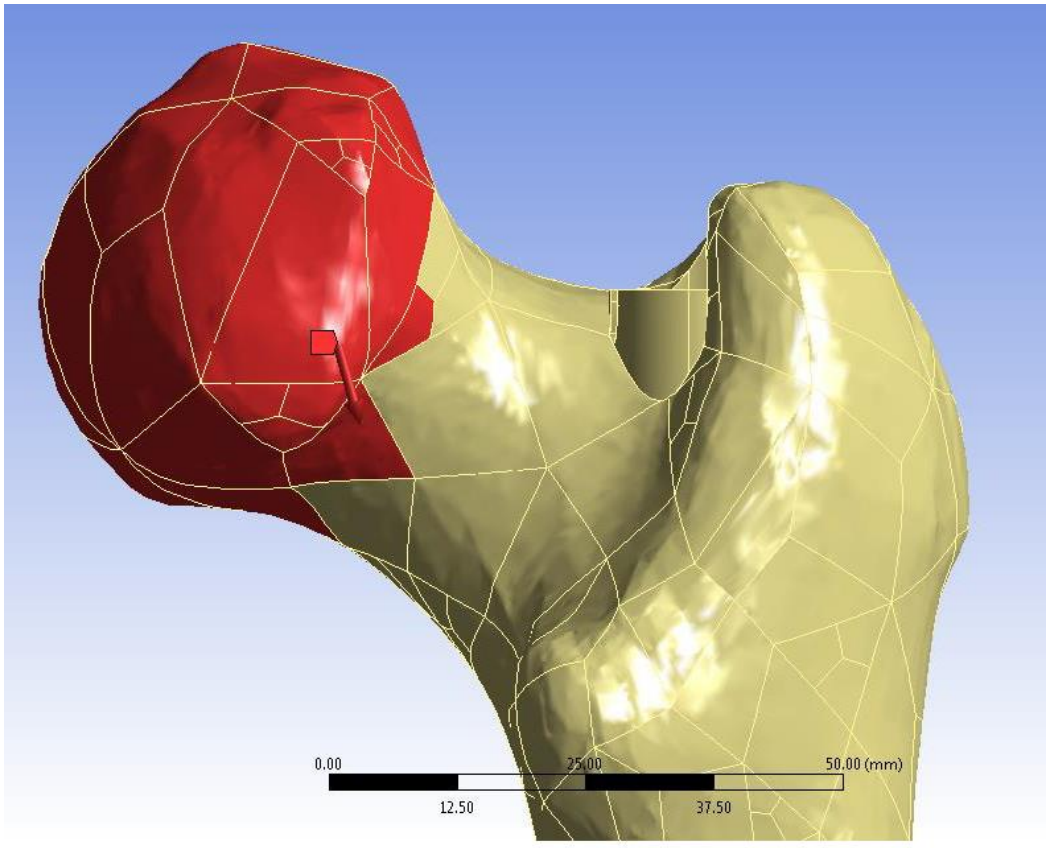

Figure 4.2.12 Gait forces applied to the head of the femur.

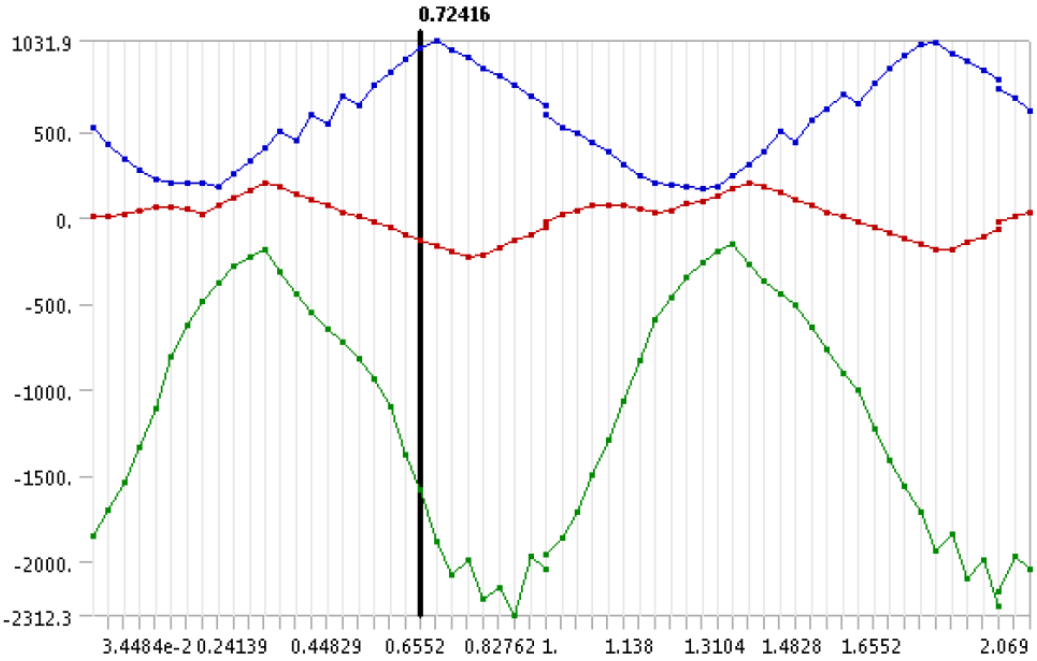

Figure 4.2.13 Graph of the forces applied to the femur during the gait cycle.

4.3 Discussion of FEA Results

Data collection was performed across the four different models under three different loading conditions. Visual inspection of the models was useful in determining the areas of high stress occurrence. The visual information was a useful tool to gauge the validity of the results (Figures 4.3.1-4.3.3). Due to the complexity of the setup of the models, there were many cases where the simulation failed to produce real results. This could be seen during visual inspection of the models as they often show high amounts of stress in irregular places (Figure 4.3.4).

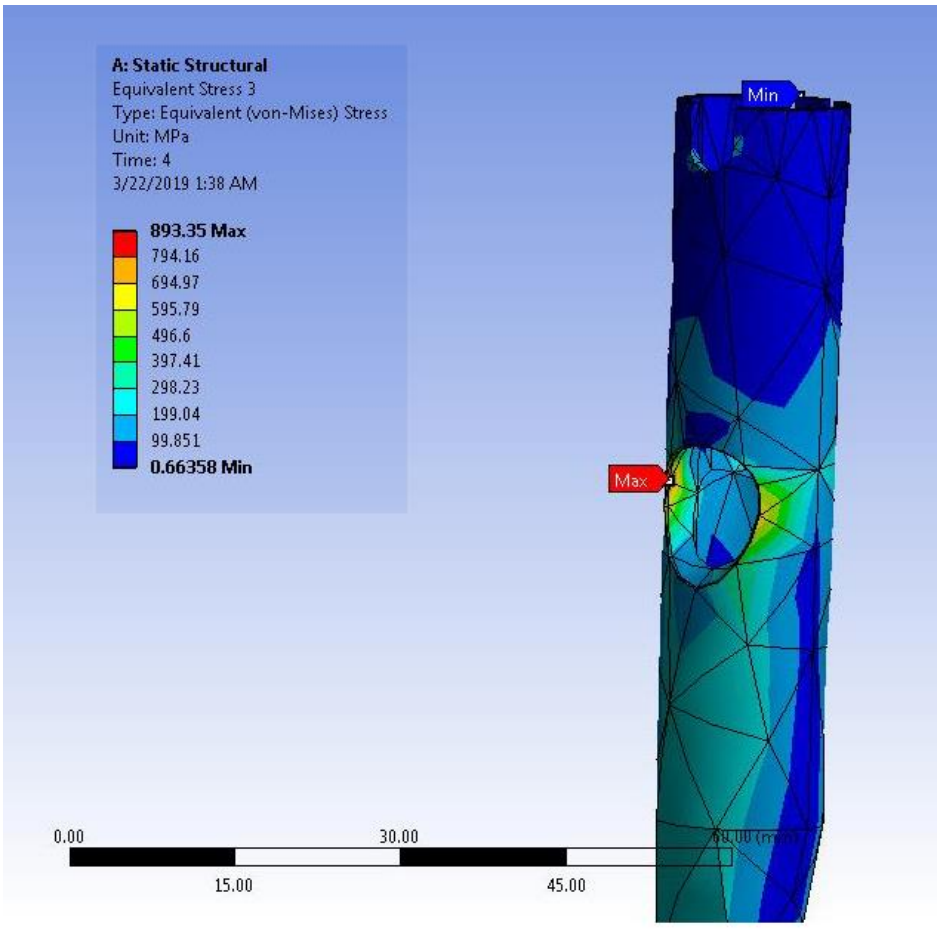

Figure 4.3.1 Stress distribution on the femoral nail.

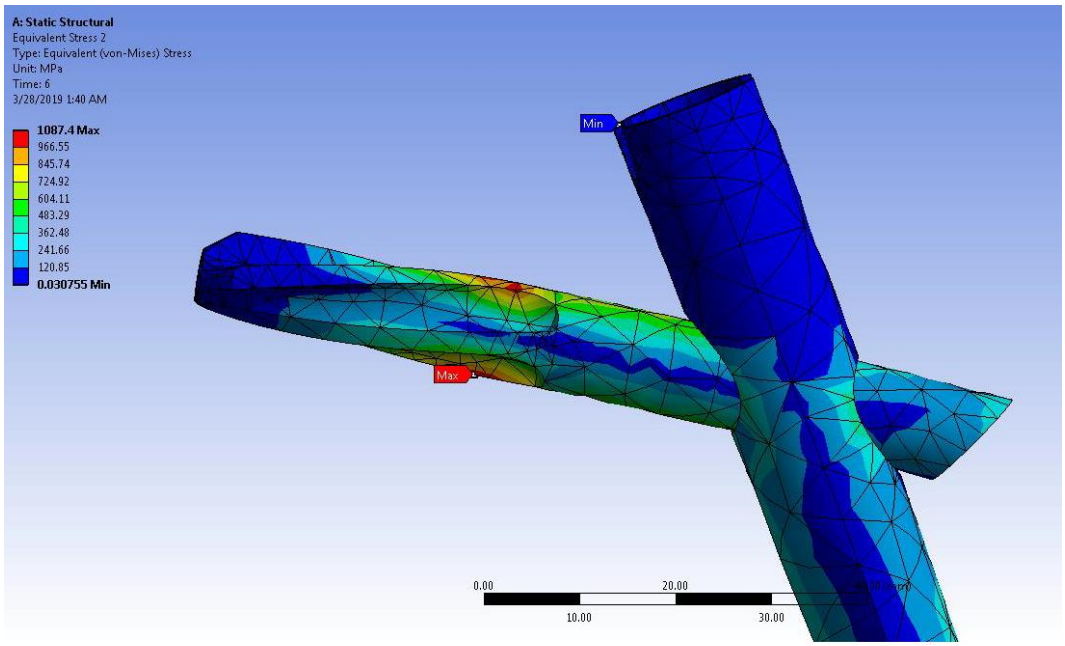

Figure 4.3.2 Stress distribution on the nail and screw.

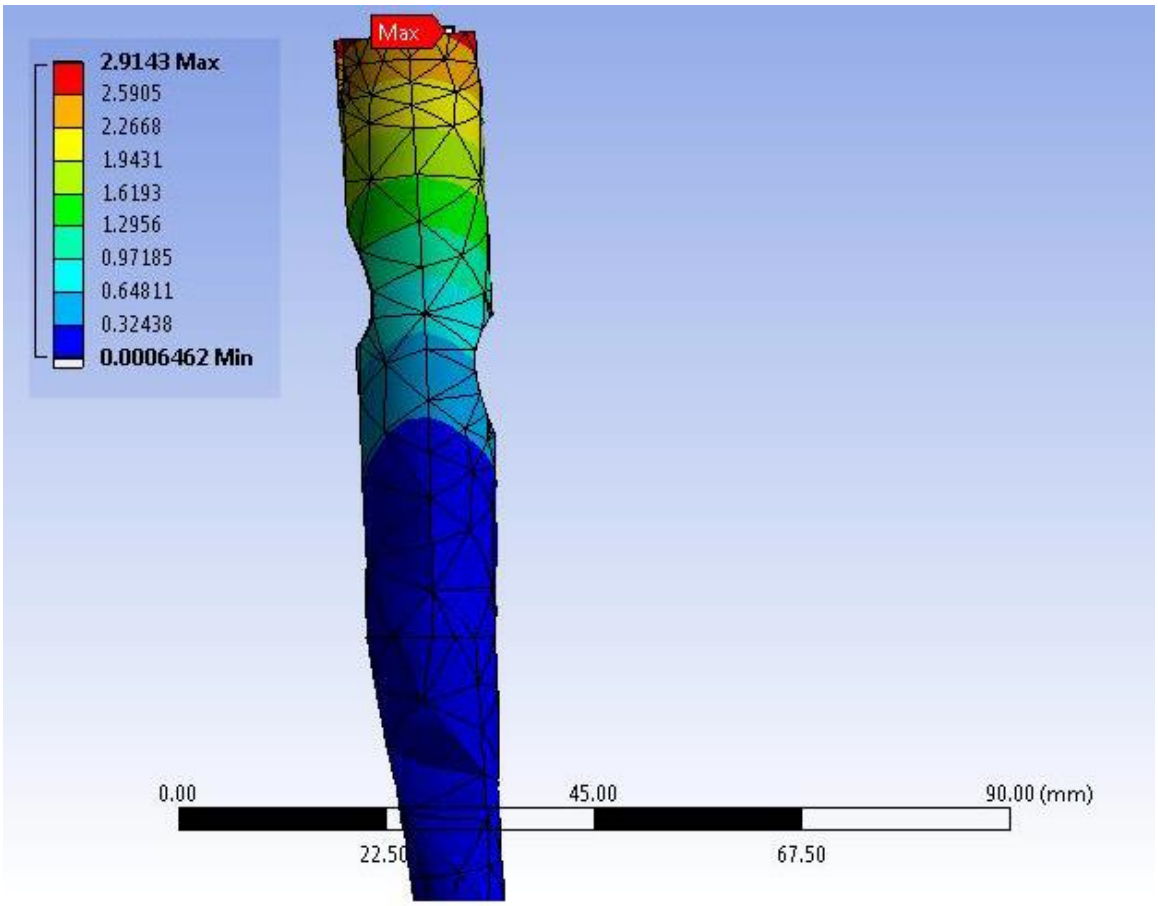

Figure 4.3.3 Total deformation on nail.

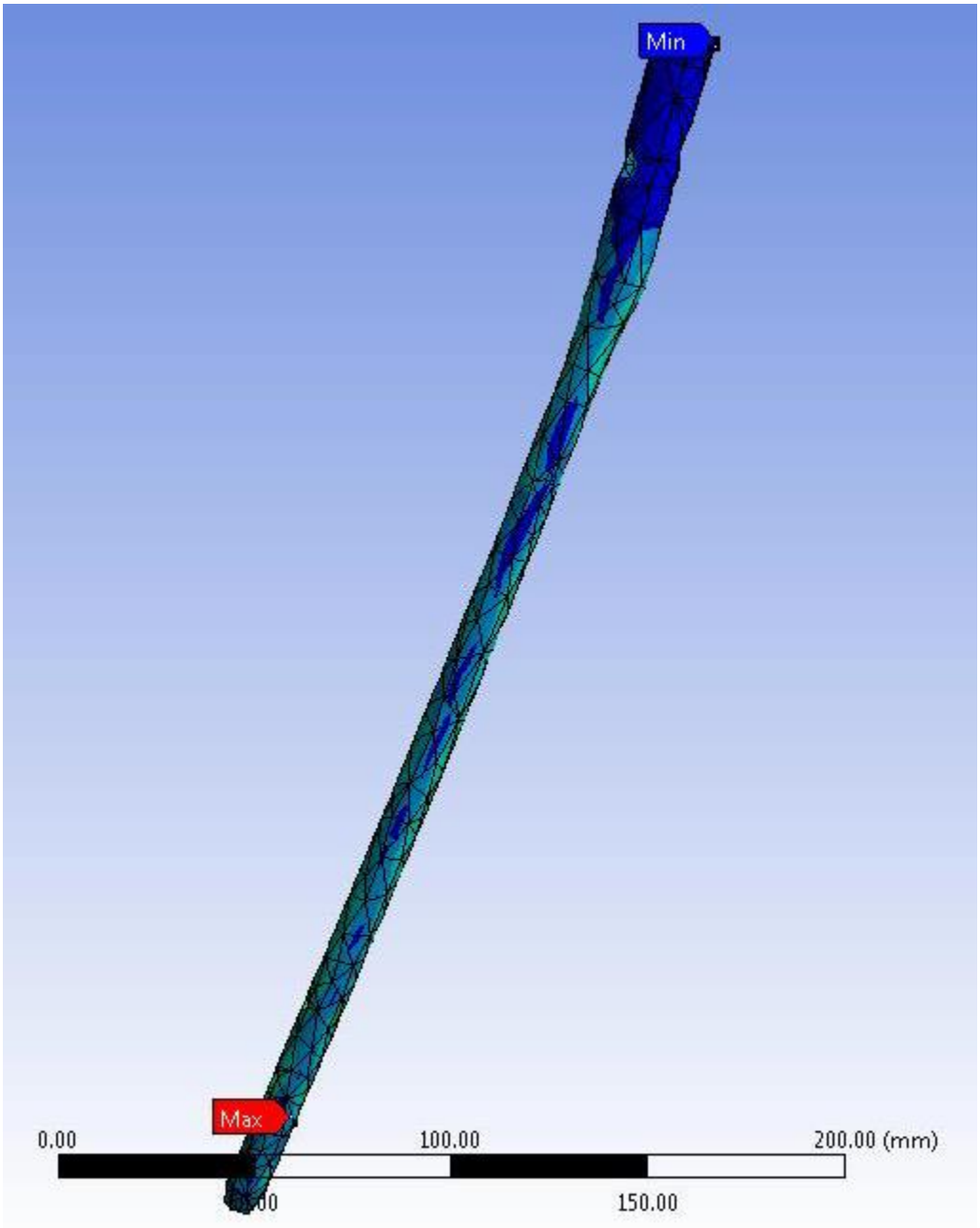

Figure 4.3.4 Irregular distribution of internal stress.

Information was collected on equivalent stress, total deformation, equivalent elastic strain, and shear stress [Appendix 1-32]. A problem with these data sets is that the simulations collect data past the point where a real test specimen would have failed. In order to find the true max values for these data sets, we needed to

calculate the loads when the nail would have failed. To accomplish this, the data points were loaded into JMP Pro 13 software for analysis. The data were plotted using fit Y by X chart where Newtons and Newton meters were charted along the x-axis and stresses were plotted along the y-axis (Figures 4.3.5, 4.3.6). With the data plotted, the program can calculate an equation for a linear fit line through the data set (Table 4.3.1). Equations were also generated for total deformation, equivalent elastic strain, and shear stress using the same methods (Table 4.3.2). Since the tensile yield strength is known to be 1050 MPa, these equations can be used to calculate the force required to fail the device and the time that the failure occurred (Table 4.3.3). The values generated for force allied at the time of failure can be used in the equations to calculate the total deformation, equivalent elastic strain, and shear stress to ascertain their max values at the time of failure (Tables 4.3.4, 4.3.5). For the simulations of the gait cycle, the maximum values were organized for comparison (Table 5.1.6).

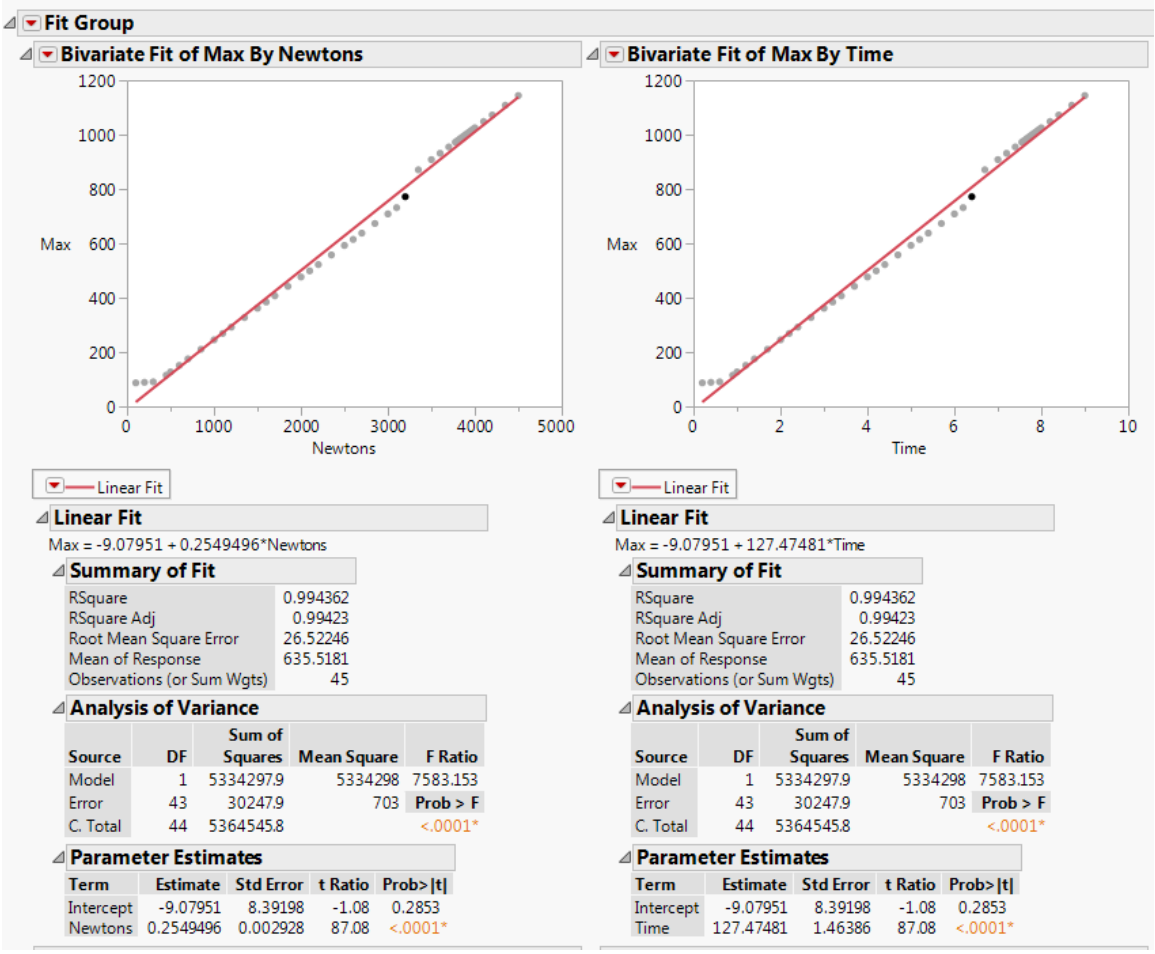

Figure 4.3.5 Graphs of data from loading to failure.

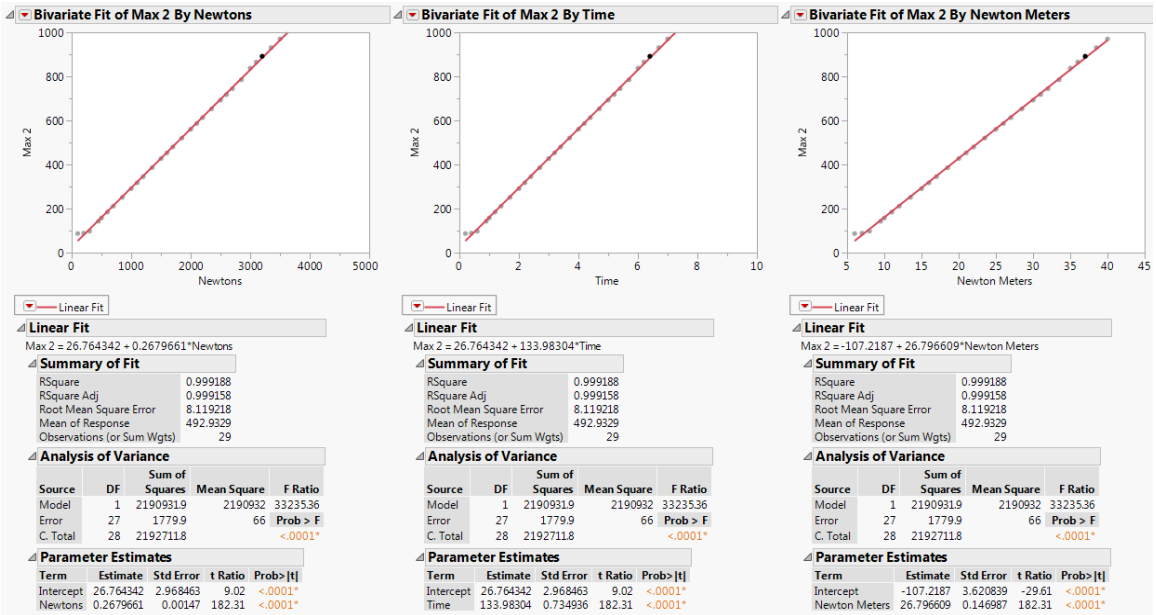

Figure 4.3.6 Graphs of data from loading and torque to failure.

Table 4.3.1 Equations for stress for loading to failure and loading and torque to failure.

	Stress Load to Failure (MPa)	**Stress Load and Torque to Failure (MPa)**
Normal	$\sigma = 38.931412 + 0.2591927*N$	$\sigma = 7.0509289 + 0.2970706*N$ $\sigma = 7.0509289 + 29.707059*Nm$
Subtrochanteric	$\sigma = -37.83904 + 0.5619352*N$	$\sigma = -88.43195 + 0.6193804*N$ $\sigma = -88.43195 + 61.938038*Nm$
Intertrochanteric	$\sigma = -64.32084 + 0.4833329*N$	$\sigma = -86.4131 + 0.5295368*N$ $\sigma = -86.4131 + 52.953684*Nm$
Intracapsular	$\sigma = 4.1232507 + 0.3602025*N$	$\sigma = 4.1232507 + 0.3602025*N$ $\sigma = 4.1232507 + 36.020245*Nm$

Table 4.3.1 Equations for total deformation, elastic strain, and shear stress for loading to failure.

	Total Deformation at Failure (mm)	**Elastic Strain Load at Failure (mm/mm)**	**Shear Stress Load at Failure (MPa)**
Normal	d = -0.041909 + 0.0005042*N	ε = 0.0003788 + 2.307e-6*N	τ = 11.111765 + 0.0839675*N
Subtrochanteric	d = -0.071 + 0.0006796*N	ε = -0.000353 + 4.9582e-6*N	τ = -23.2806 + 0.1699704*N
Intertrochanteric	d = 0.0459699 + 0.0004033*N	ε = -0.000538 + 4.2512e-6*N	τ = -37.69338 + 0.2084864*N
Intracapsular	d = 0.0694474 + 0.0004262*N	ε = 0.0006202 + 1.8964e-6*N	τ = 37.124356 + 0.0477092*N

Table 4.3.2 Equations for total deformation, elastic strain, and shear stress for loading and torque to failure.

	Total Deformation at Failure (mm)	**Elastic Strain at Failure (mm/mm)**	**Shear Stress at Failure (MPa)**
Normal	d = -0.043159 + 0.0004717*N d = -0.043159 + 0.0471691*Nm	ε = 8.8849e-5 + 2.6309e-6*N ε = 8.8849e-5 + 0.0002631*Nm	τ = 1.2514524 + 0.0859061*N τ = 1.2514524 + 8.590613*Nm
Subtrochanteric	d = -0.079682 + 0.000706*N d = -0.079682 + 0.0705973*Nm	ε = -0.000791 + 5.4571e-6*N ε = -0.000791 + 0.0005457*Nm	τ = -24.0961 + 0.1523619*N τ = -24.0961 + 15.236192*Nm
Intertrochanteric	d = 0.0731563 + 0.0004262*N d = 0.0731563 + 0.042619*Nm	ε = -0.000855 + 4.7591e-6*N ε = -0.000855 + 0.0004759*Nm	τ = -48.7579 + 0.2274627*N τ = -48.7579 + 22.74627*Nm
Intracapsular	d = 0.0694351 + 0.0004262*N d = 0.0694351 + 0.0426176*Nm	ε = 0.0006199 + 1.8967e-6*N ε = 0.0006199 + 0.0001897*Nm	τ = 37.124403 + 0.047685*N τ = 37.124403 + 4.7684961*Nm

Table 4.3.3 Max stress from the loading simulations.

	Load to Failure (N)	Failure Per Average Body Weight	Load and Torque to Failure (N + Nm)	Failure Per Average Body Weight w/Torque
Normal	3900.83N	4.88BW	3510.78N+35.11Nm	4.389BW
Subtrochanteric	1935.88N	2.42BW	1838.02N + 18.38Nm	2.3BW
Intertrochanteric	2305.49N	2.88BW	2146.05N + 21.46Nm	2.68BW
Intracapsular	2903.58N	3.63BW	2903.58N + 29.04Nm	3.63BW

Table 4.3.4 Max deformation, strain, and shear from loading scenarios.

	Total Deformation at Load to Failure (mm)	Elastic Strain at Load to Failure (mm/mm)	Shear Stress at Load to Failure (MPa)	Total Deformation at Load and Torque to Failure (mm)	Elastic Strain at Load and Torque to Failure (mm/mm)	Shear Stress at Load and Torque to Failure (MPa)
Normal	1.924	0.009378	338.66	1.613	0.009325	302.85
Subtrochanteric	1.245	0.009245	305.76	1.218	0.009239	255.95
Intertrochanteric	0.976	0.009263	442.97	0.988	0.009358	439.39
Intracapsular	1.307	0.006126	175.65	1.307	0.006127	175.58

Table 4.3.5 Gait comparison

	Max Deformation (mm)	Max Stress (MPa)	Max Strain (mm/mm)	Max Shear (MPa)
Normal	0.68012	420.61	3.7521e-003	120.28
Subtrochanteric	0.74314	586.66	5.2314e-003	155.04
Intertrochanteric	0.49534	518.11	4.6686e-003	153.99
Intracapsular	0.64256	512.61	3.4559e-003	109.23

The data produced from the finite element analysis can provide a comparison of how fracture type influences internal forces in the nail. Using the weight of the average adult male, 800N [40], and average torque experienced during walking, 13Nm [15], the data can be expressed as a ratio of average body weight average torque. A normal femur could be expected to withstand up to 3900.83N, 4.88 times the weight of the average adult male before it fails. A femur with a complete subtrochanteric fracture fairs the worst with only being able to withstand 1935.88N, just 2.42 times the average weight of an adult male. When factoring in for torque that would be present in a realistic loading scenario, the loading needed to fail was reduced to 3510.78N, a 10% decrease. The subtrochanteric fracture again shows the largest change decreasing to 1838.02N. That is a 5% reduction with only being able to withstand 2.3times the body weight of an adult male. The information generated also gives some insight into how different fractures influence the stress produced within the intramedullary nail. When comparing the fracture types to the normal femur model, the subtrochanteric, intertrochanteric, and intracapsular have a 50%, 41%, and 26% decrease in max load to failure, respectively. The data also shows that when

adding torque, the intracapsular fracture saw almost no change in the load to failure. The added torque did, however, have a significant effect on decreasing the load to failure other fracture types. When considering the effects of the gait cycle on the nail the data shows that all the femur models were experiencing loads up to 420-580MPa, depending on the fracture type. The fatigue limit of the titanium alloy Ti-6Al-7Nb is 580 per ten million cycles [39]. Considering this only one fracture type produces stress in this range. It is possible that the subtrochanteric fracture load the nail beyond the fatigue limit of the material. This should, however, not be a serious problem. When loading at the threshold it would take 10 million loading cycles before the material would fail. This would take more time than what is needed for the nail to complete its job. These types of internal fixation devices are not designed to be used indefinitely [31]. It is important to note that these tests consider that the nail is without any damage. While the device is not likely to fail from the cyclic loading from walking on its own, this could change if the device was damaged.

CHAPTER 5: Results

5.1 Conclusion

This project utilized a combination of qualitative and quantitative analysis to determine the causes of failure of a medical device. The analyses of the device under microscope show the self-tapping helical screw likely had rough contact with the interior of the femoral nail. This is evident by the scrape marks on both the screw and the nail. The microscope analysis also shows the likelihood that the nail failed due to overloading the material after some period of mechanical fatigue. This was later confirmed when the failure area was examined under SEM. The SEM analysis shows the propagation of an internal crack though cyclical loading resulting in microscopic striations. The striations averaged 0.689 micrometers in length. At this length the nail could have failed in as few as 11,000 cycles. There is also the characteristic of overloading failure occurring in several places along the fracture surface. This suggests the crack propagated to the point where a portion of the nail could no longer withstand the internal force generated during use. At this point, that portion of the device was overloaded and failed. The crack continued to grow and overloading failed the device. This cycle of crack growth and overload failure continued until the nail weakened to the point where it fractured into two pieces. The computational simulations show that an undamaged femur can withstand the forces of 4.4x the body weight of the average adult male. A femur subtrochanteric fracture, however, can only withstand over 2.3x the same weight, nearly 50% lower than the normal femur.

With this low amount it isn't impossible that an overloading scenario could occur. The data from the gait cycle shows that with a subtrochanteric fracture the nail experiences stress just within the fatigue limit of the material. Given the collected data the subtrochanteric fractures is most likely candidate for causing failures when comparing fracture types.

5.2 Future Direction

For a definitive conclusion to be reached on the failure of the nail, there is more information which needs to be collected. Currently, we have no radiological information for this case. The X-rays from before and after the failure can give useful insight into what happened to the nail. The femur models generated for this project were generalized models. With access to the patient X-rays, it could be possible to generate a model that accurately represents the real conditions to which the nail was subjected. Patient demography would also be useful in generating more accurate loading forces used in the gait simulations.

There is more work which needs to be performed analyzing the fracture surface under SEM. Only a small portion of the fracture surface has been examined under the SME. Currently we have not located the starting location of the initial crack. Examining this initial crack could give useful information on how it was created. Without this information, we cannot declare what created the crack in the first place. There also is not enough information gathered to accurately assess how many loading cycles the nail underwent before it failed completely. The striation should be increasing in length as the crack grows [16, 43]. With the information currently gathered, the length of the striations does not

appear to increase in any significant amount. Since these images were taken by a third party, we don't know the locations from where the high magnification images came relative to the fracture surface. Without better documentation, it would be difficult to establish the sequence of events that lead to the failure.

Moving forward it would be good for the project to independently determine the material properties present within the intramedullary nail. The modeling work completed for this project used the expected values for the material properties of the titanium alloys Ti-6Al-7Nb and Ti-15Mo as dictated by ASTM standards [63, 64]. This is, however, and assumption made based on that the chemical requirements are also as the standard requires. The EDS didn't show the presence of elements in the quantities that should be present within the alloy. There are forms of destructive testing that can be performed to learn the material properties that exist in the failed device. Performing a Rockwell hardness test we find the hardness of the alloy, which would correspond with a tensile strength [45]. With the real tensile strength of the material, the computer modeling could be refined.

Appendix

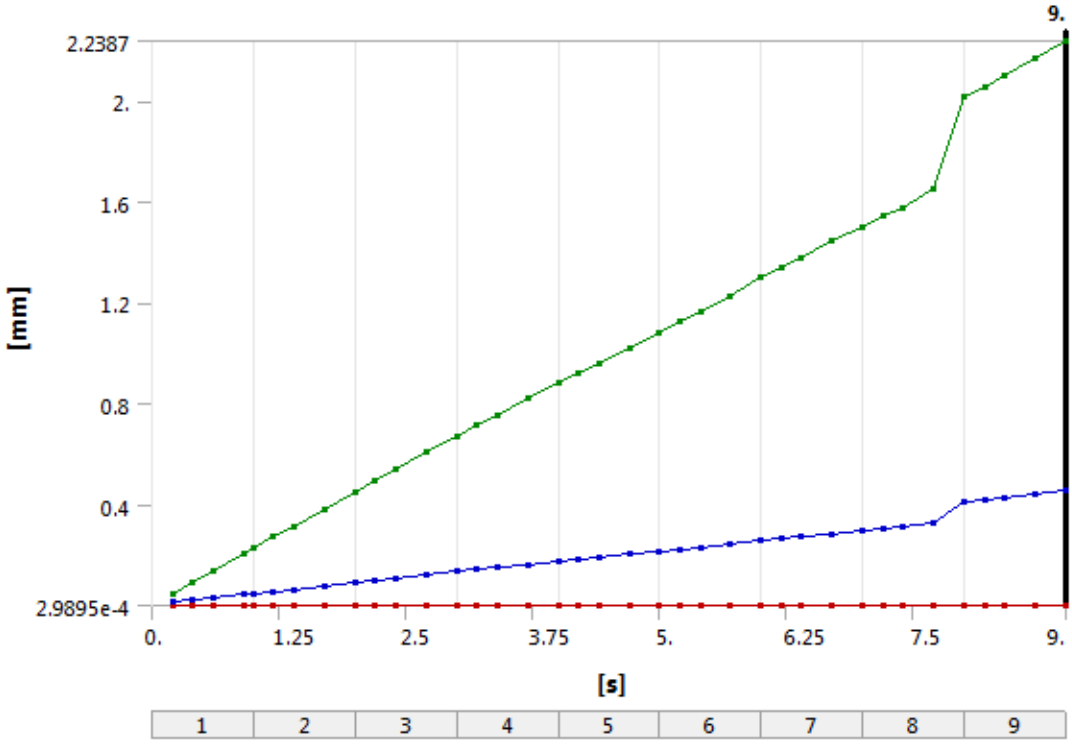

Appendix 1 Normal Femur Total Deformation

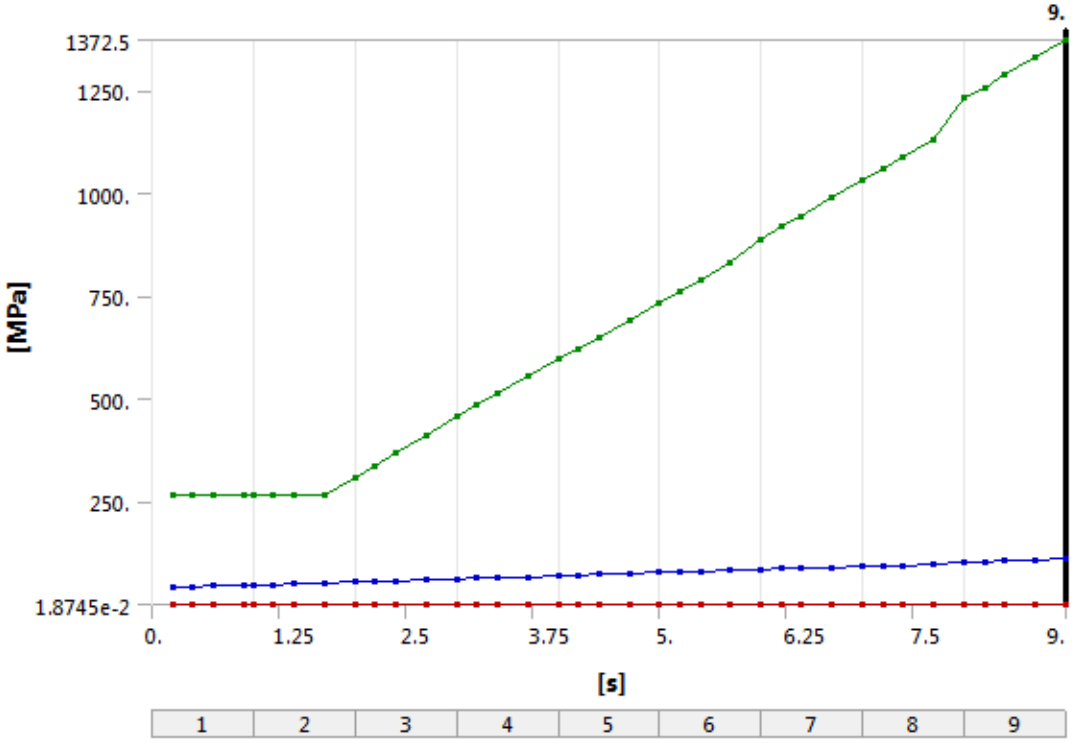

Appendix 2 Normal Femur Equivalent Stress

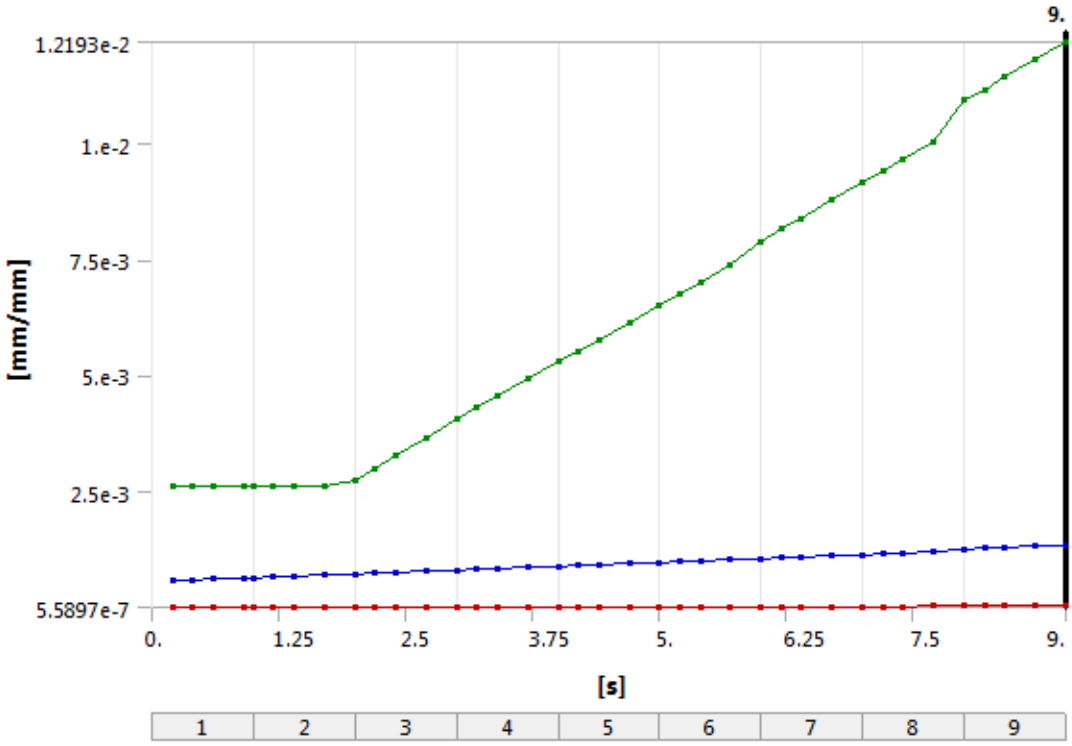

Appendix 3 Normal Femur Elastic Strain

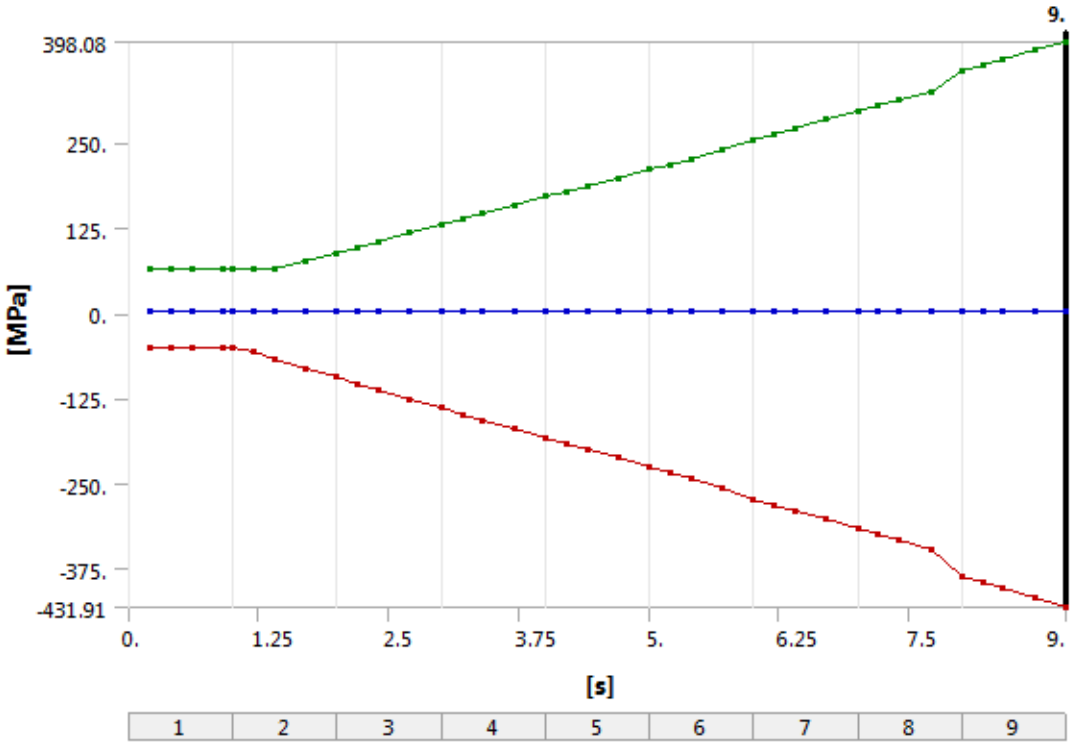

Appendix 4 Normal Femur Shear Stress

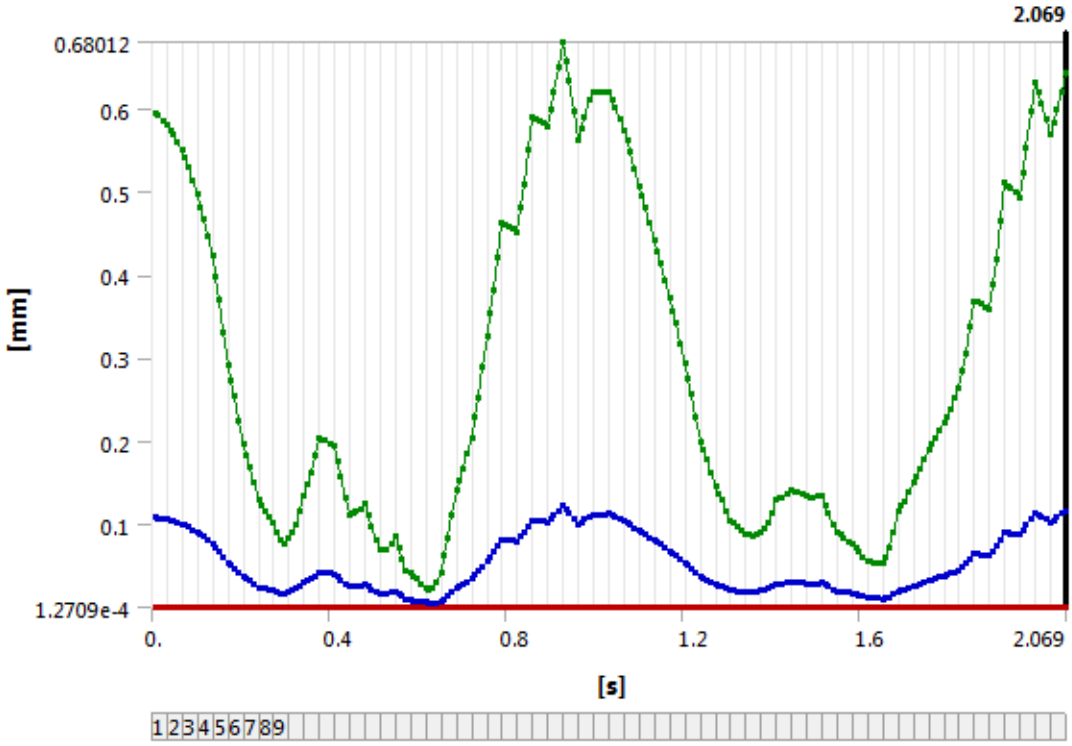

Appendix 5 Normal Femur Gait Total Deformation

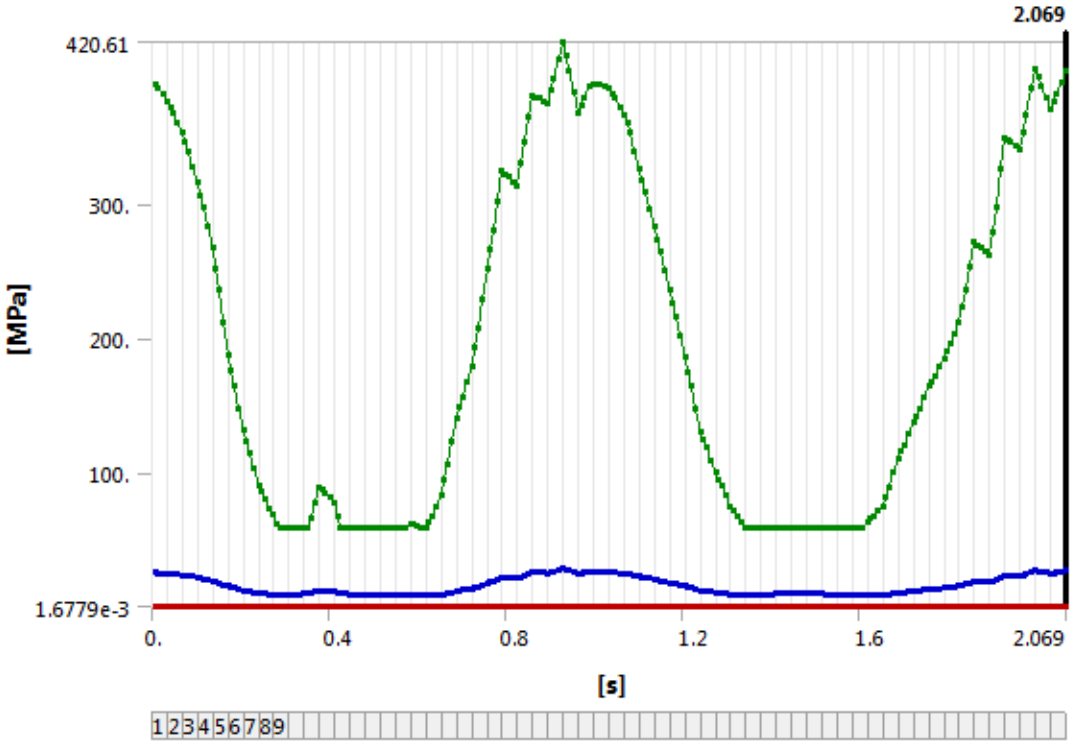

Appendix 6 Normal Femur Gait Equivalent Stress

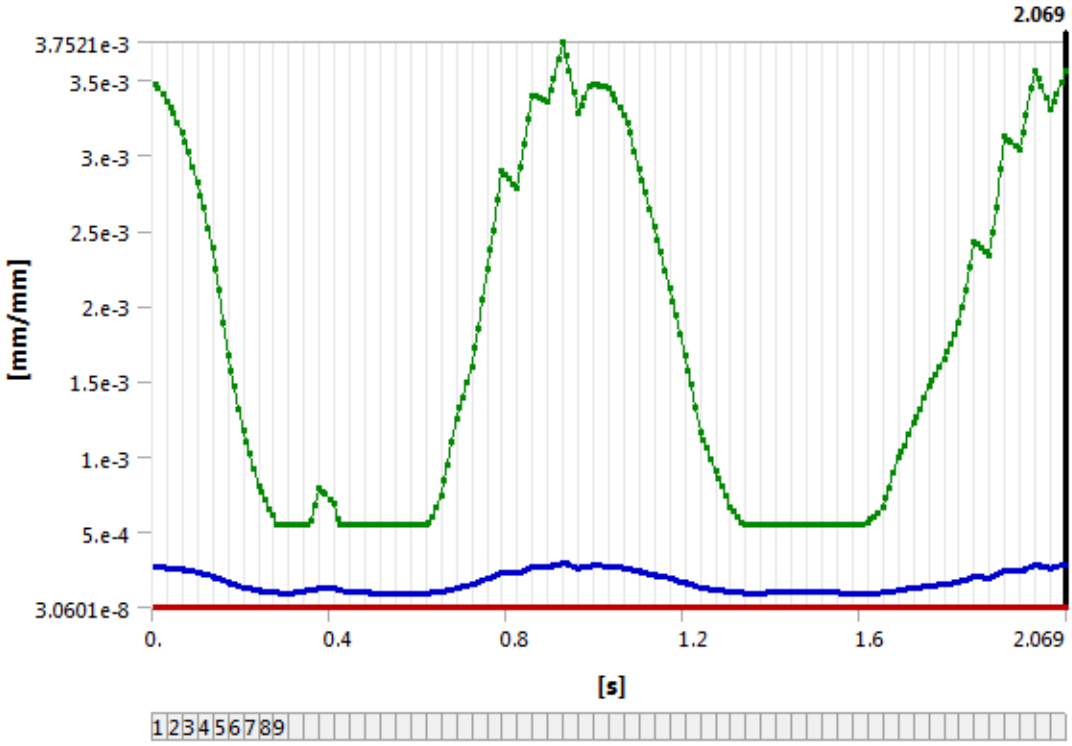

Appendix 7 Normal Femur Gait Elastic Strain

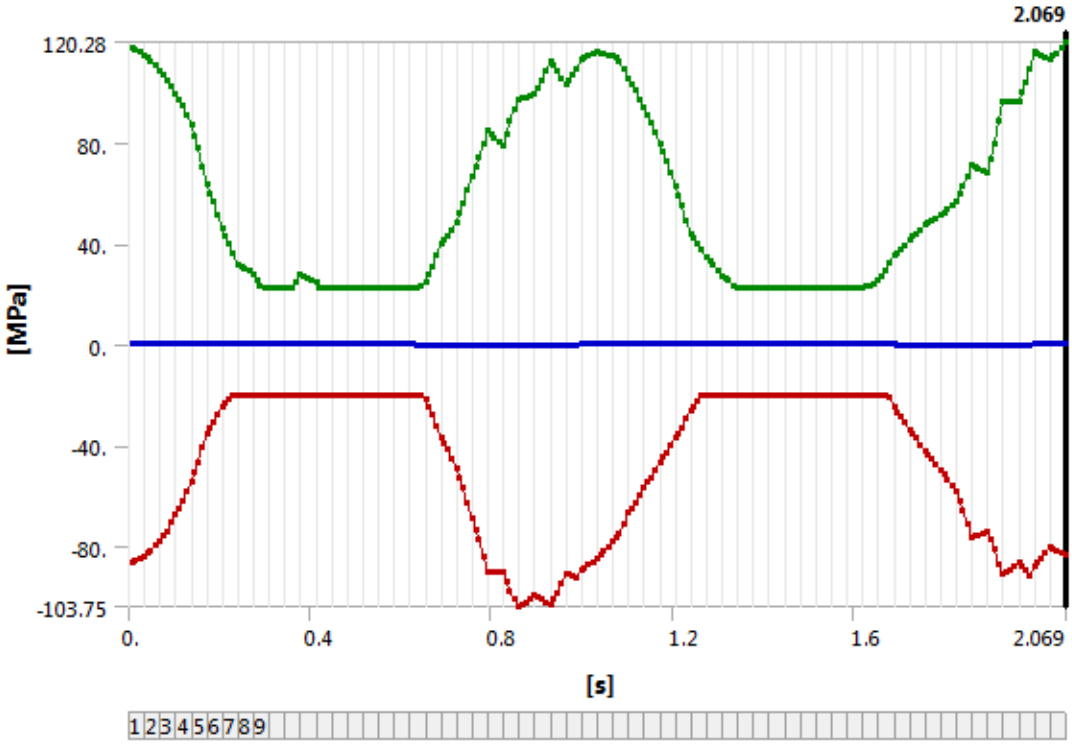

Appendix 8 Normal Femur Gait Shear Stress

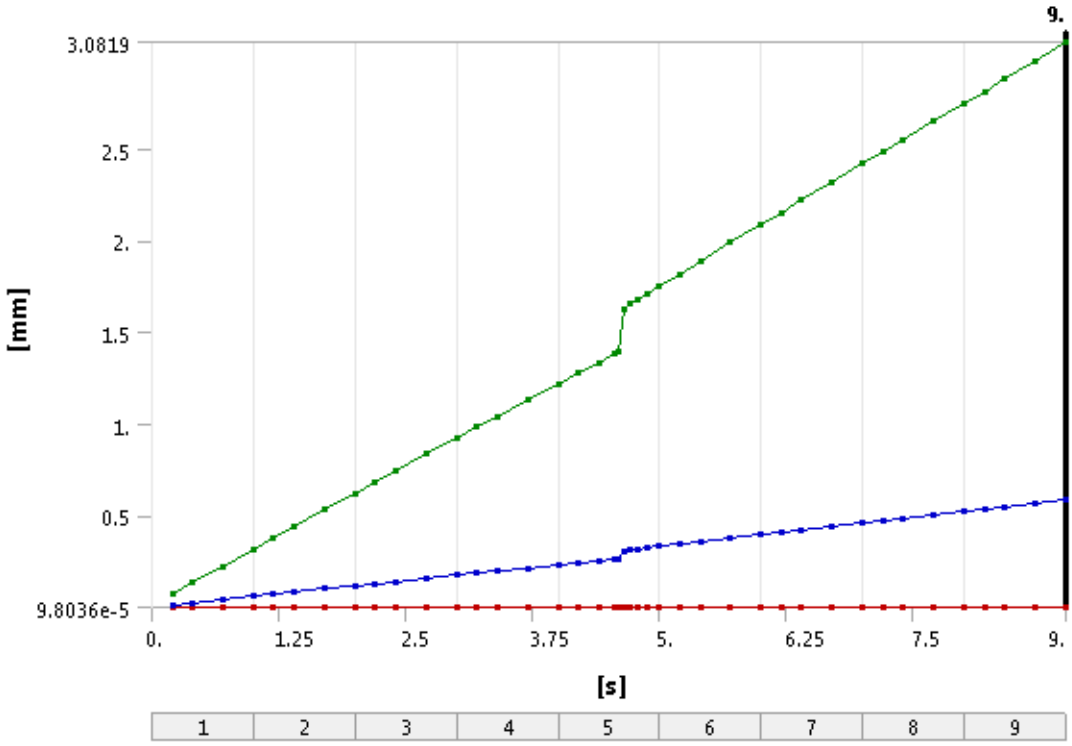

Appendix 9 Subtrochanteric Fracture Total Deformation

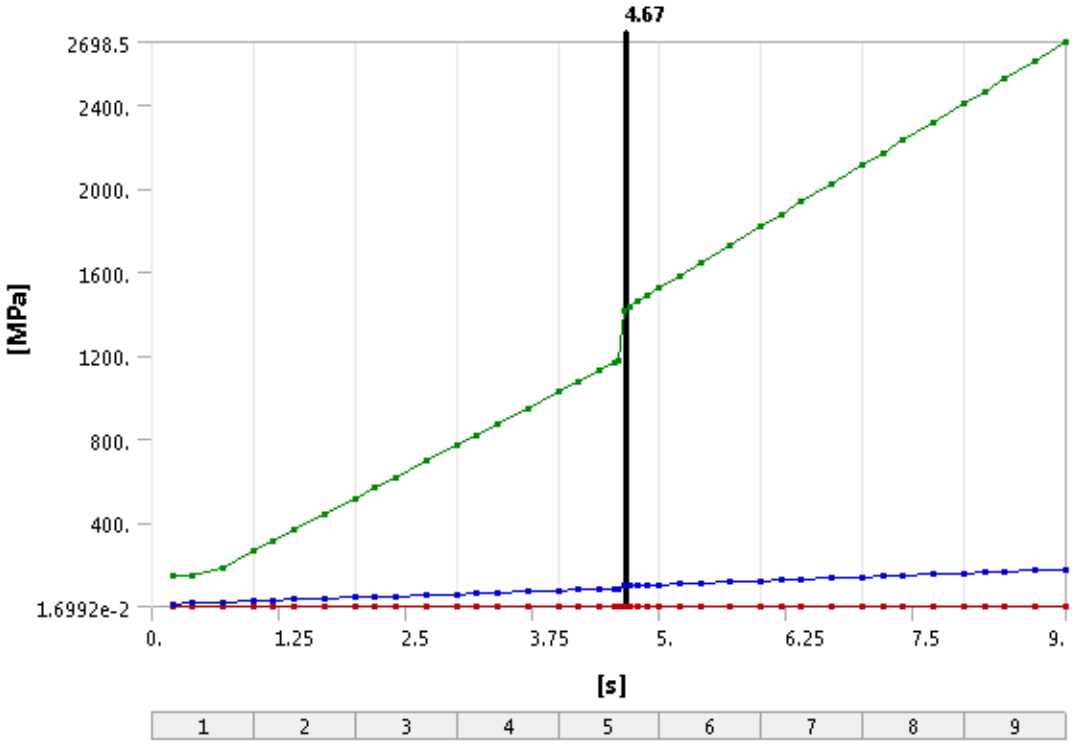

Appendix 10 Subtrochanteric Fracture Equivalent Stress

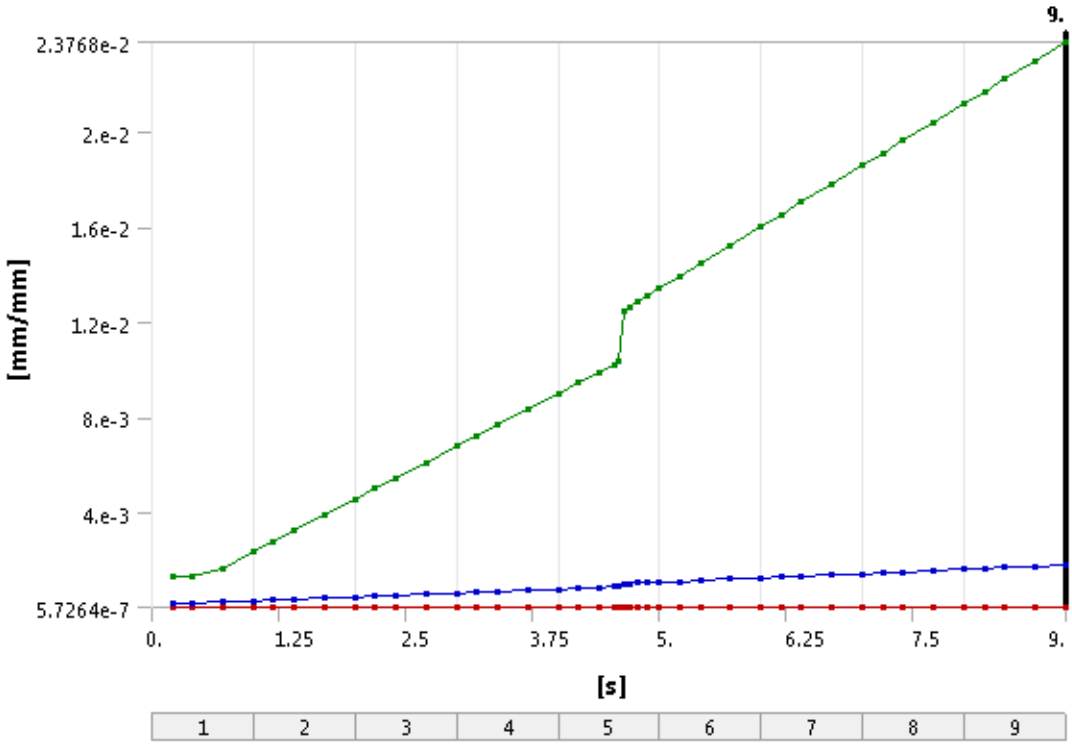

Appendix 11 Subtrochanteric Fracture Elastic Strain

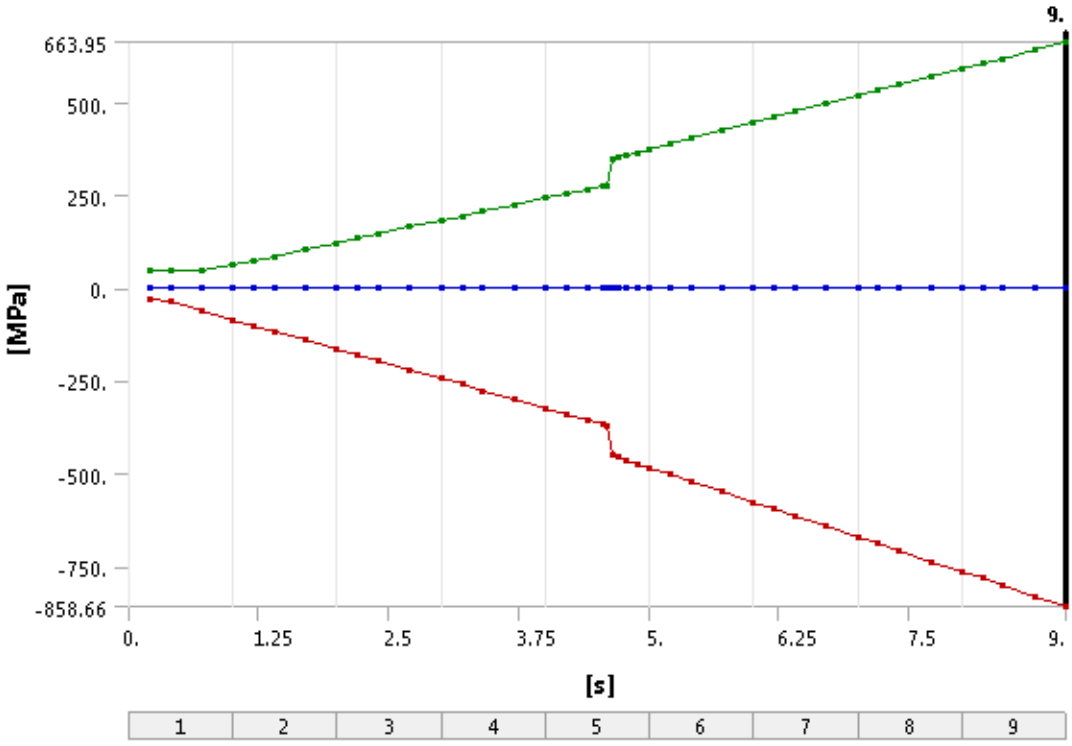

Appendix 12 Subtrochanteric Fracture Shear Stress

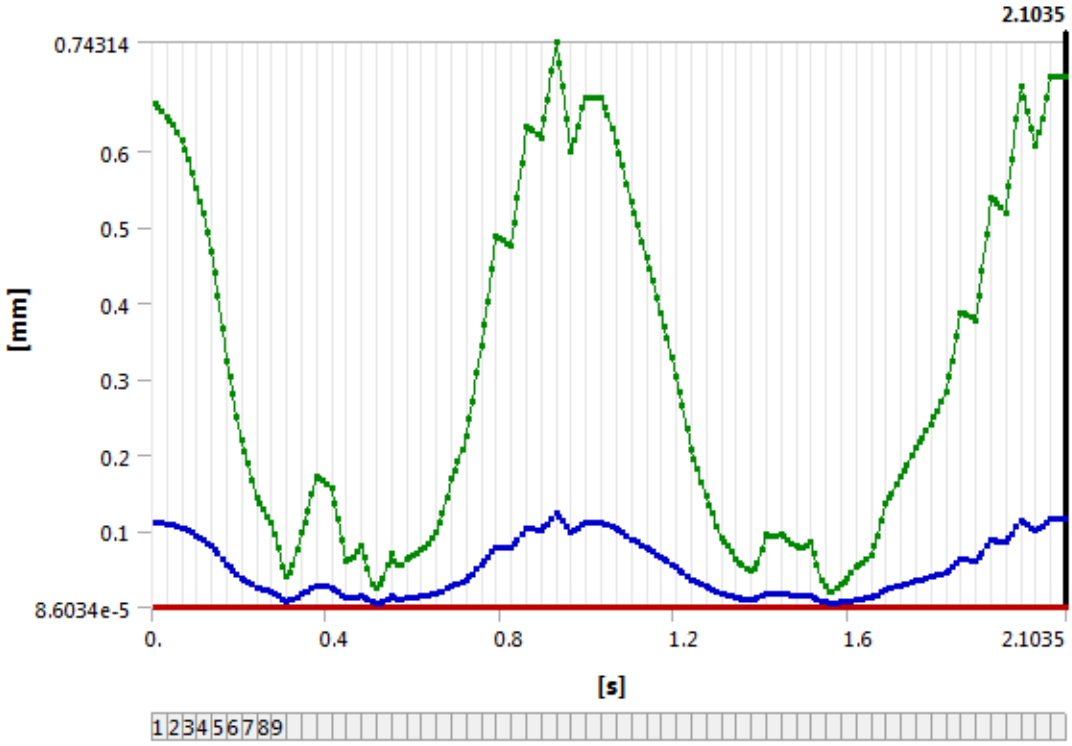

Appendix 13 Subtrochanteric Fracture Gait Total Deformation

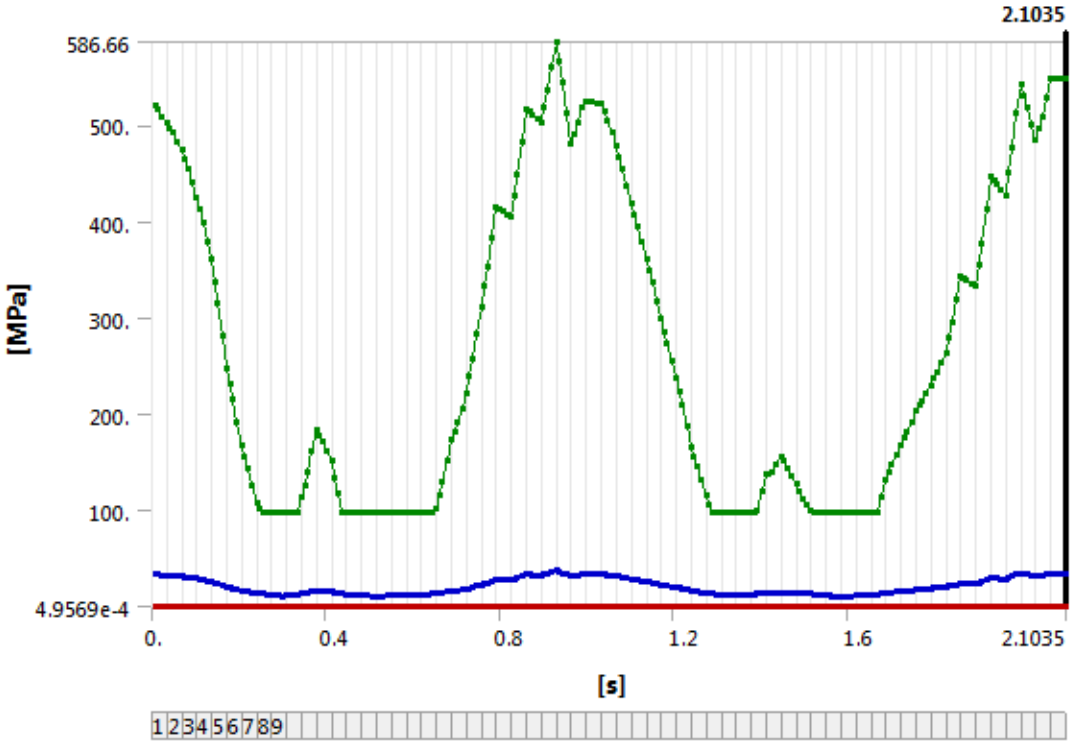

Appendix 14 Subtrochanteric Fracture Gait Equivalent Stress

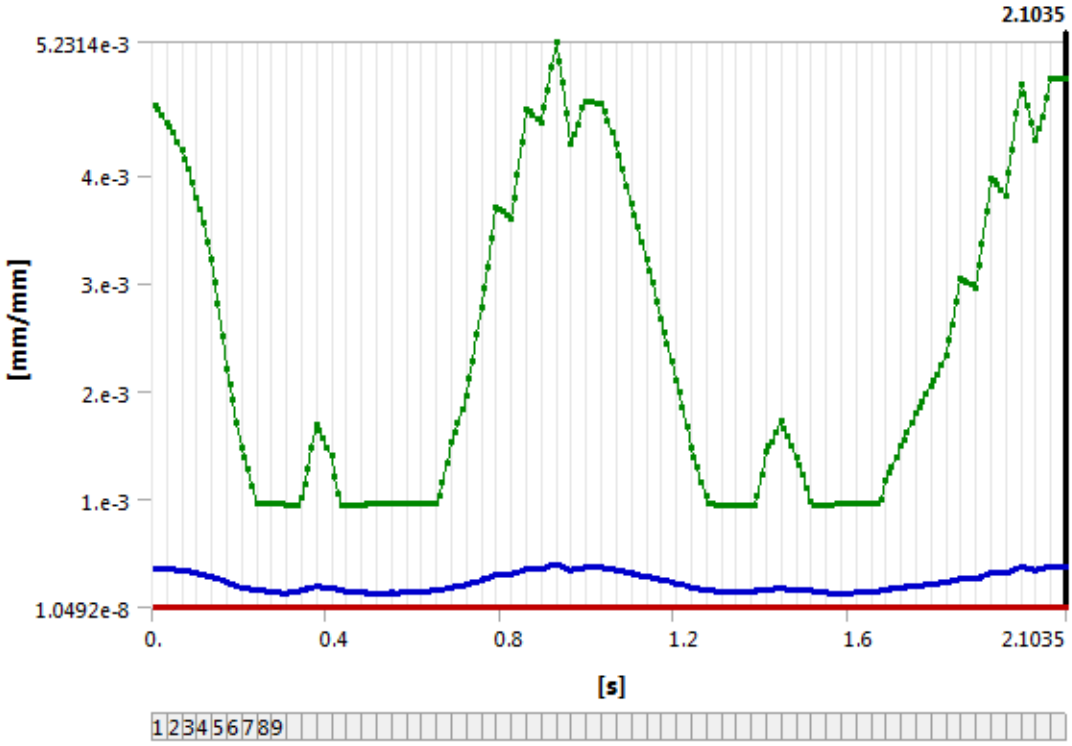

Appendix 15 Subtrochanteric Fracture Gait Elastic Strain

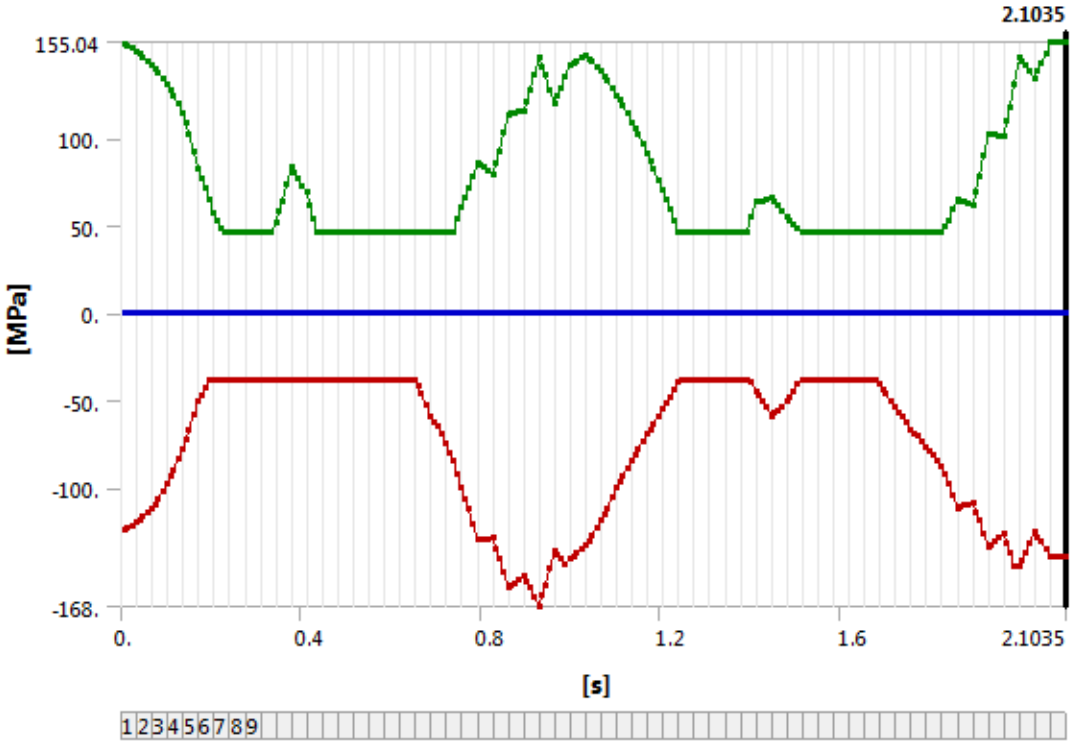

Appendix 16 Subtrochanteric Fracture Gait Shear Stress

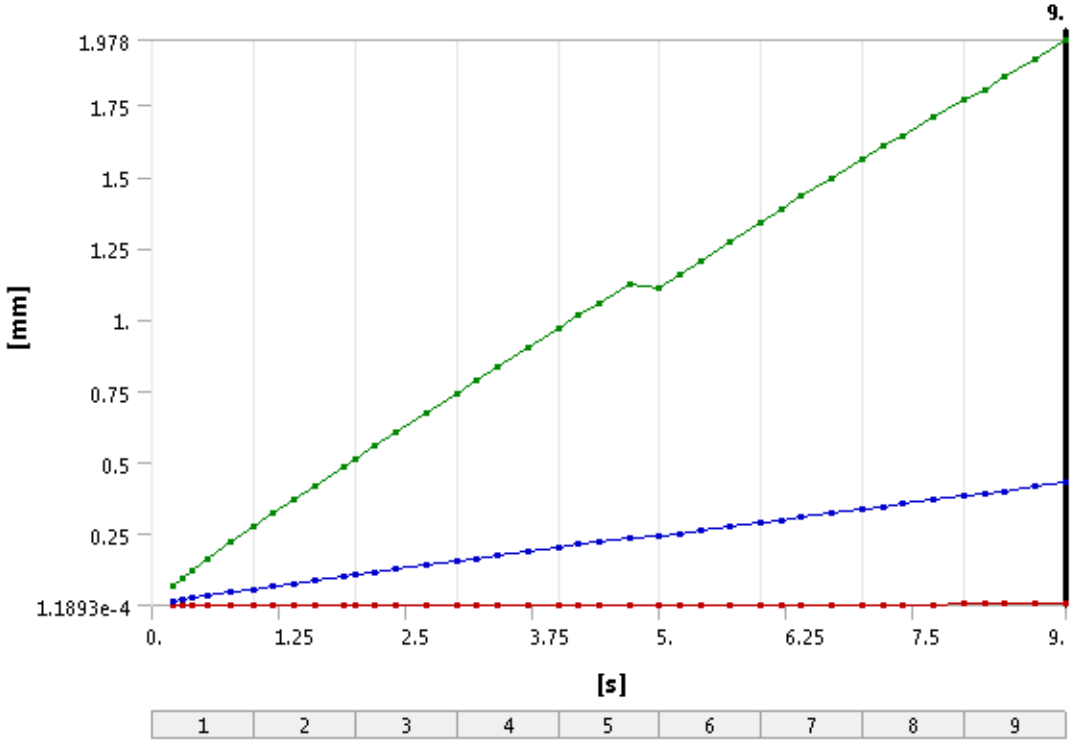

Appendix 17 Intertrochanteric Fracture Total Deformation

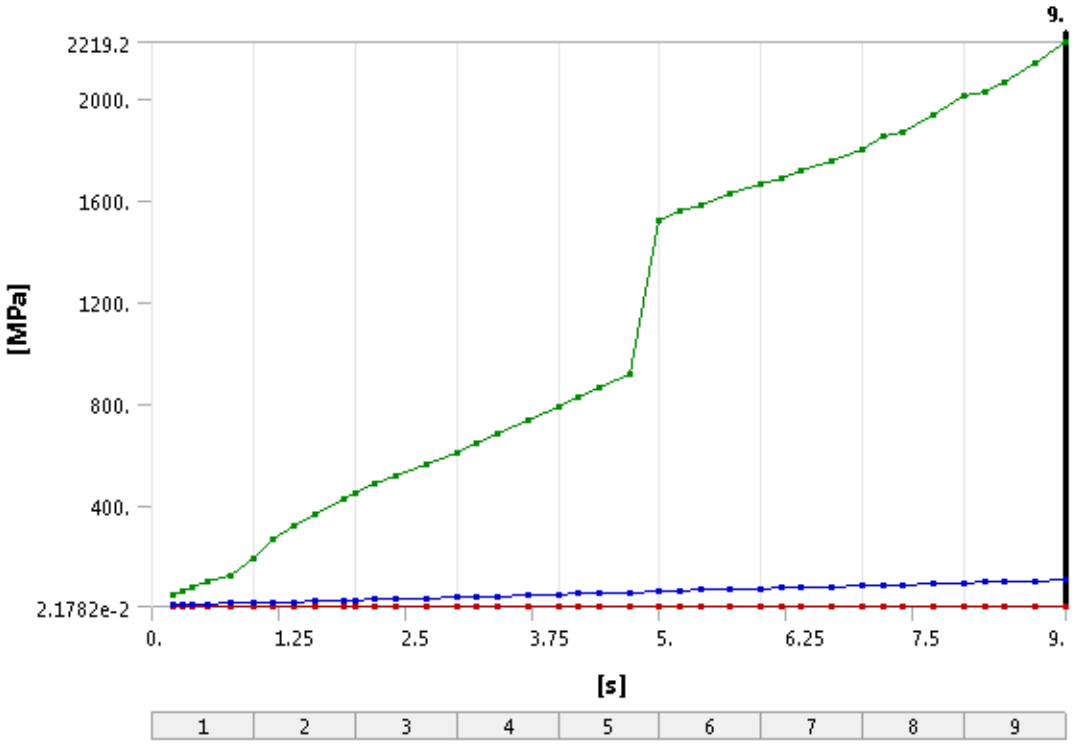

Appendix 18 Intertrochanteric Fracture Equivalent Stress

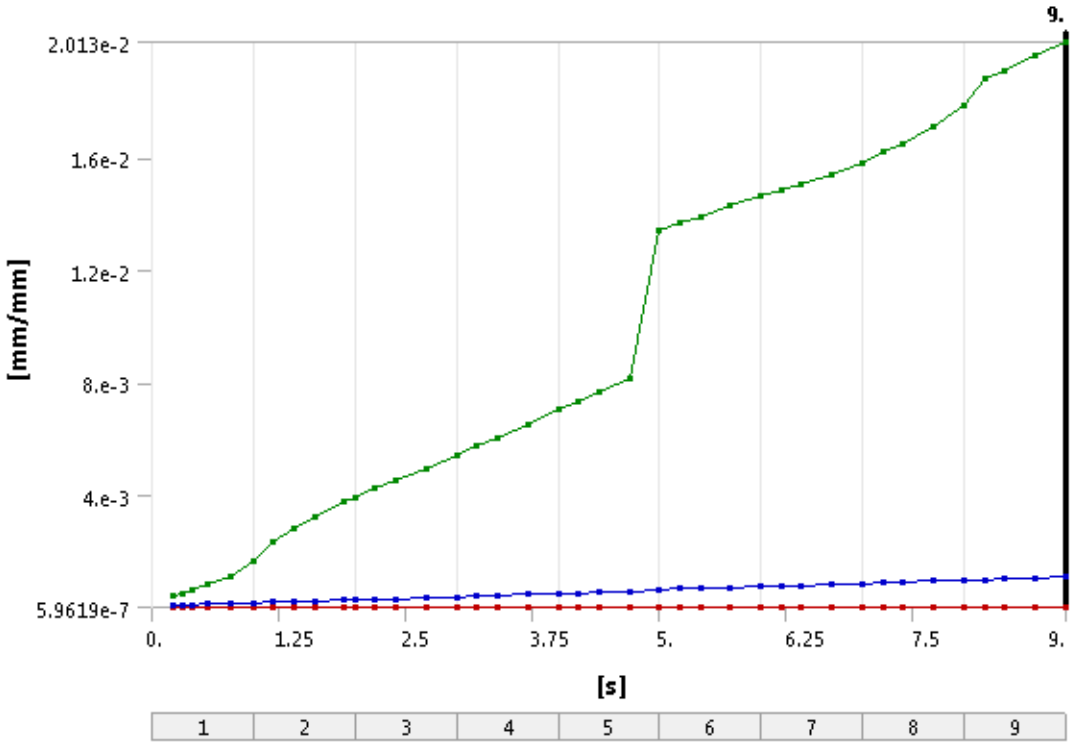

Appendix 19 Intertrochanteric Fracture Elastic Strain

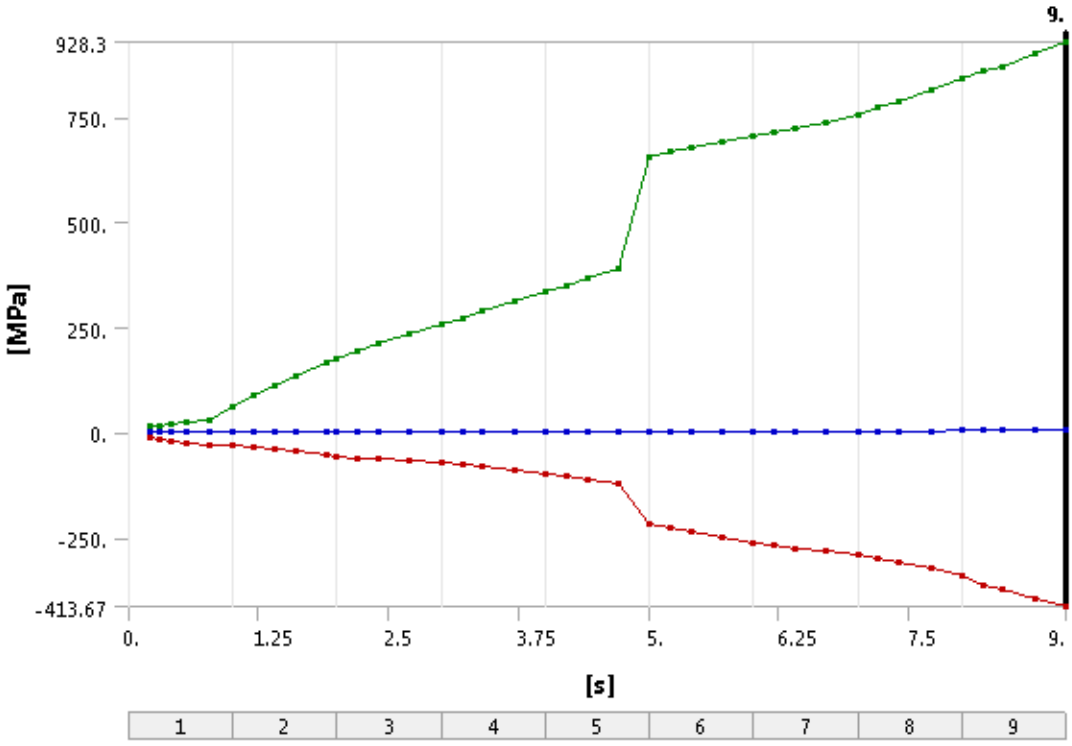

Appendix 20 Intertrochanteric Fracture Shear Stress

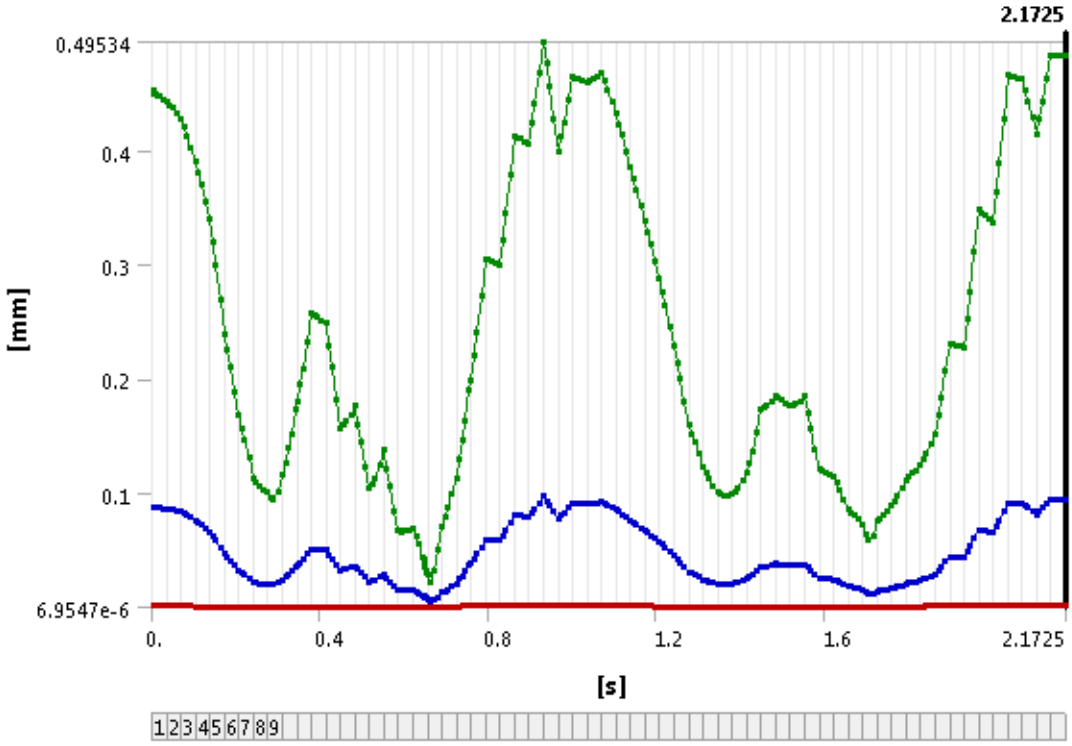

Appendix 21 Intertrochanteric Fracture Gait Total Deformation

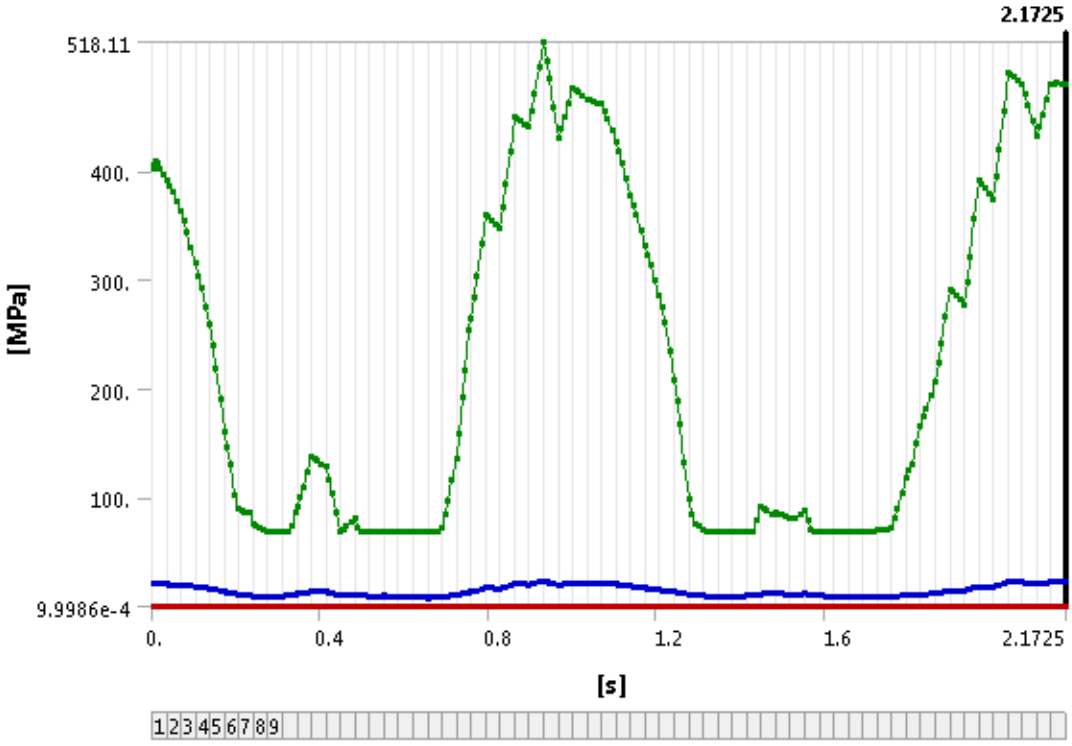

Appendix 22 Intertrochanteric Fracture Gait Equivalent Stress

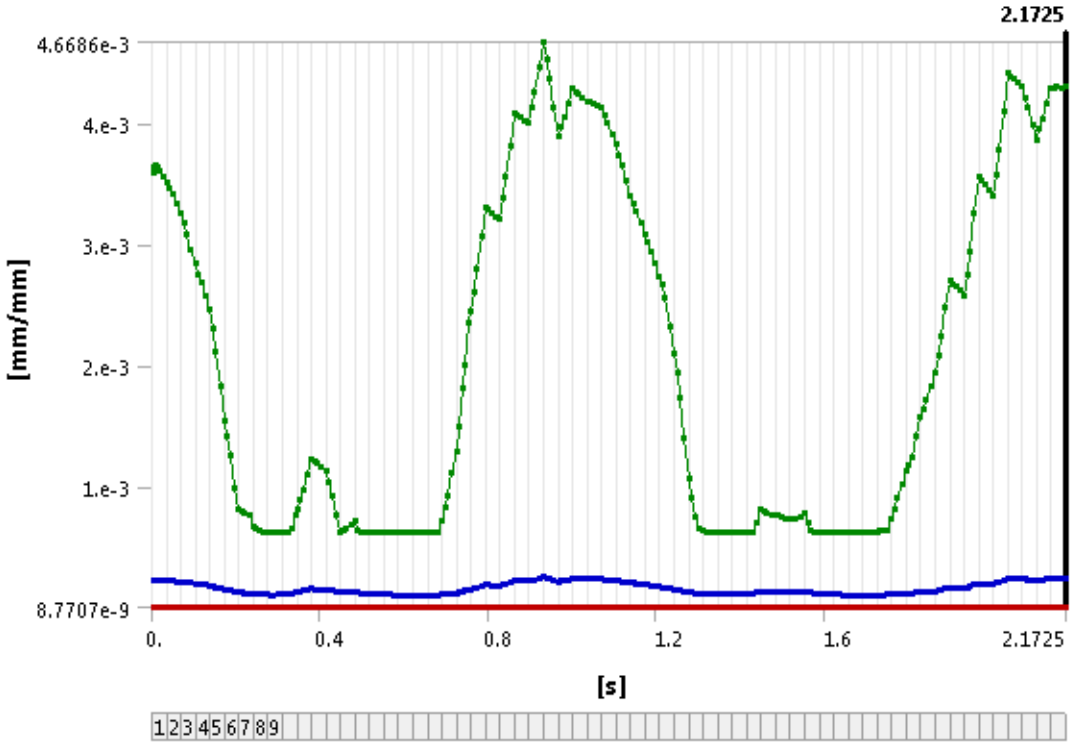

Appendix 23 Intertrochanteric Fracture Gait Elastic Strain

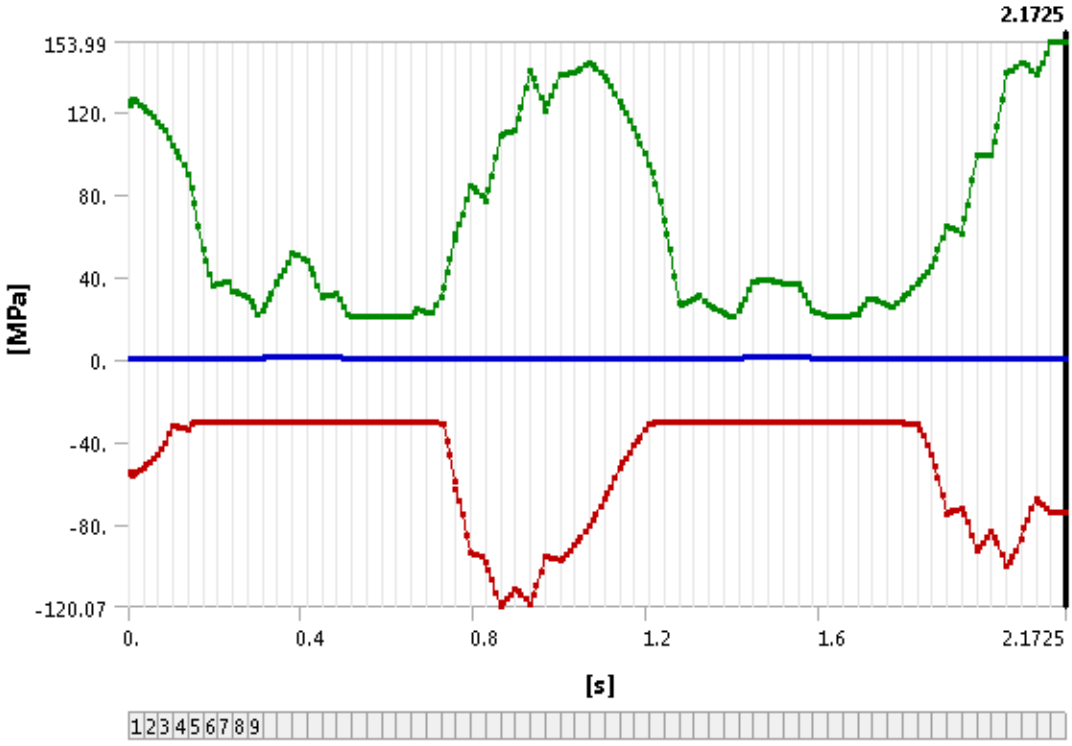

Appendix 24 Intertrochanteric Fracture Gait Shear Stress

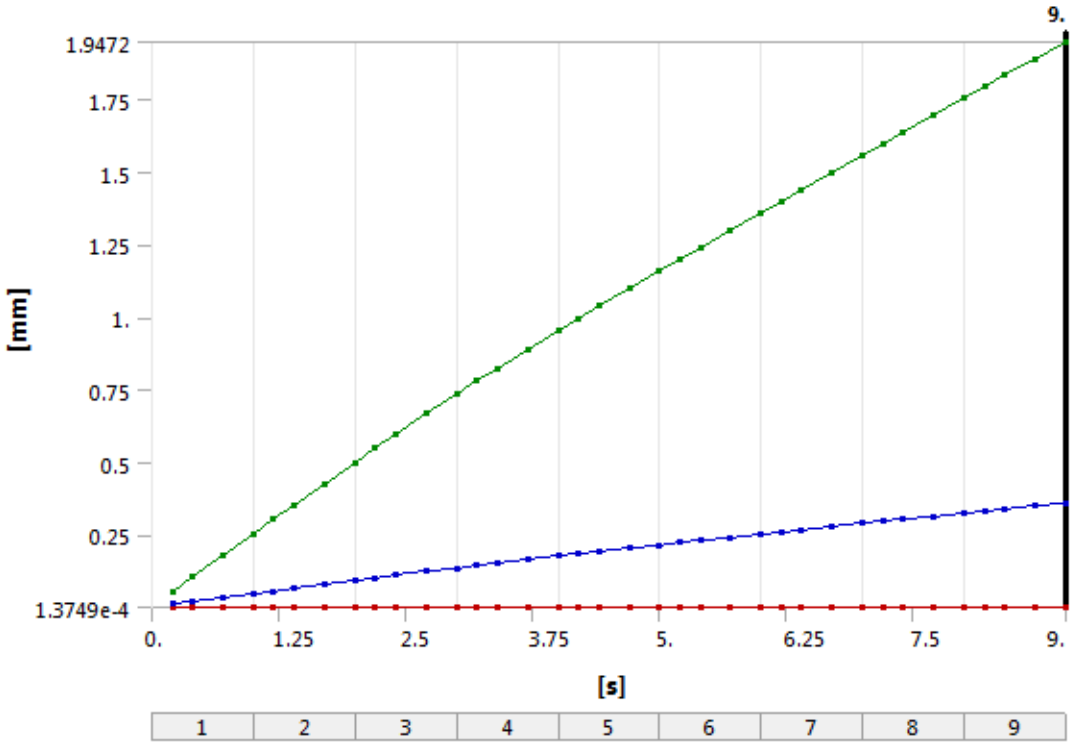

Appendix 25 Intracapsular Fracture Total Deformation

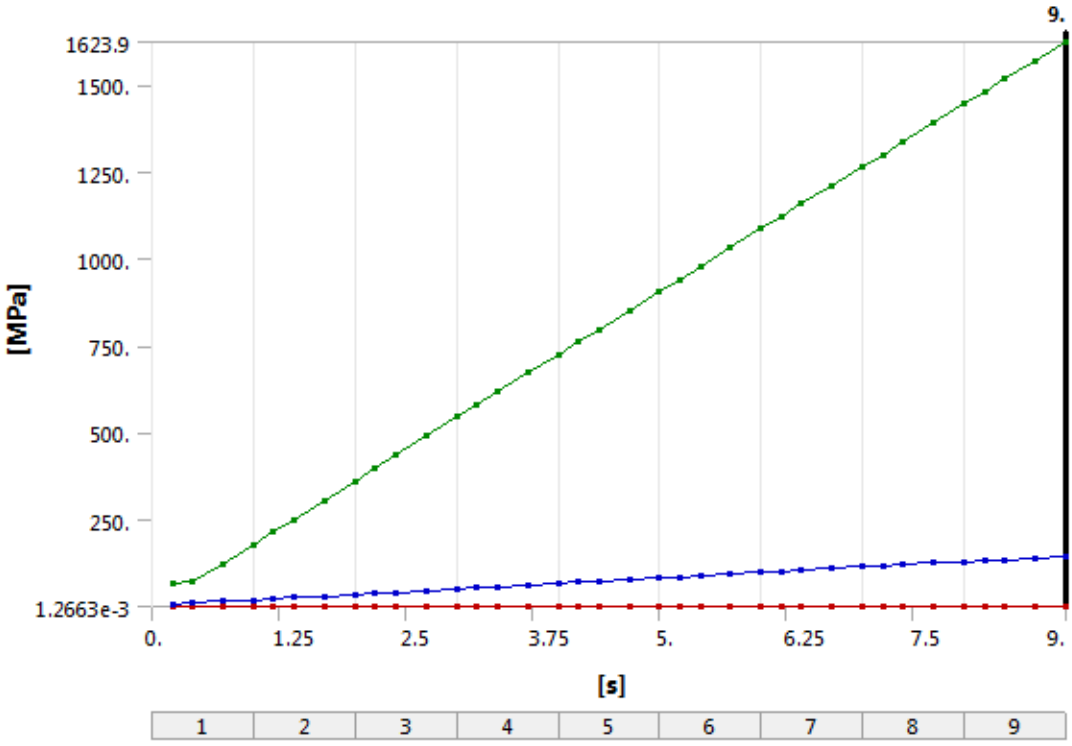

Appendix 26 Intracapsular Fracture Equivalent Stress

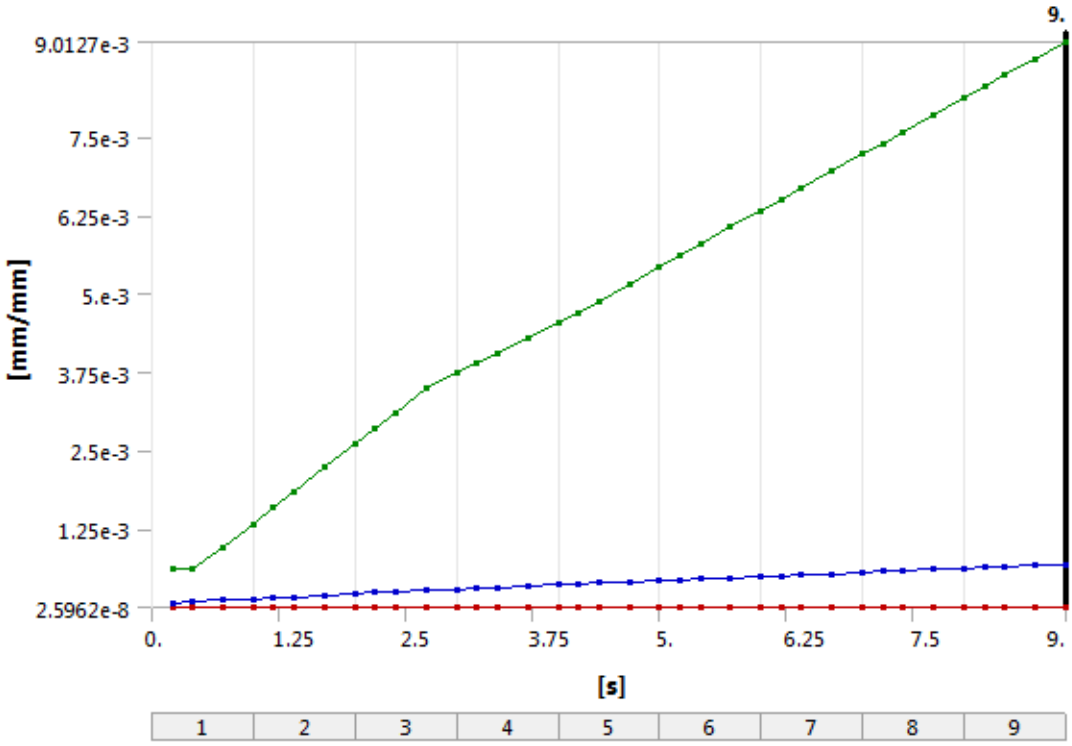

Appendix 27 Intracapsular Fracture Elastic Strain

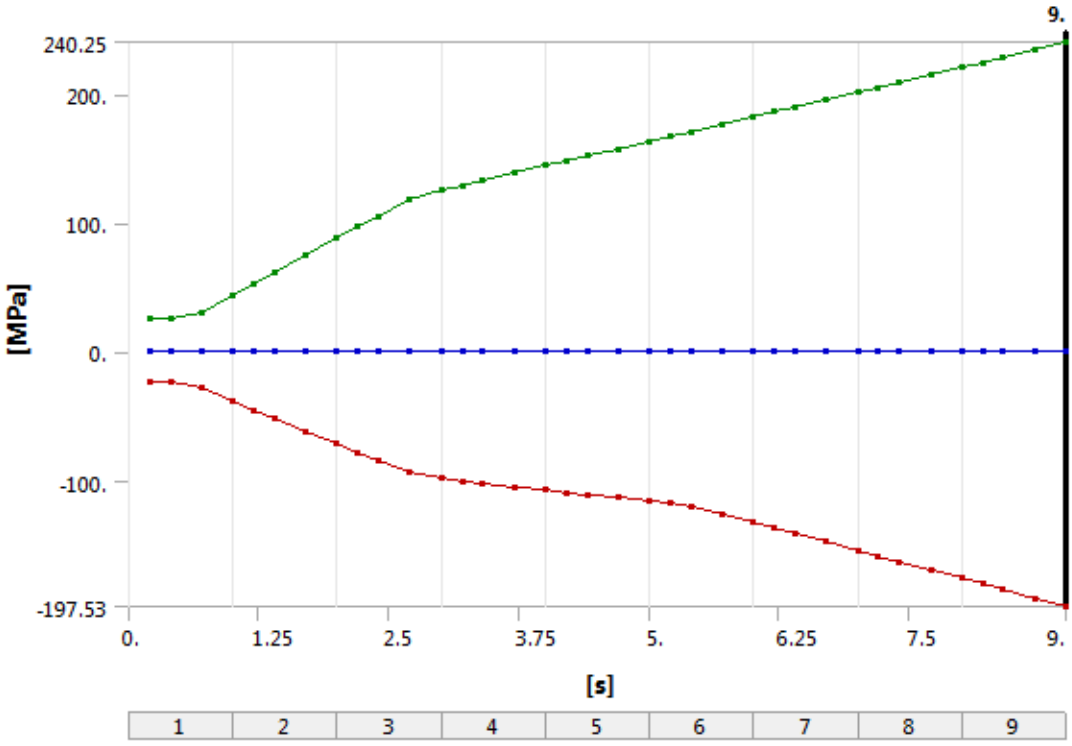

Appendix 28 Intracapsular Fracture Shear Stress

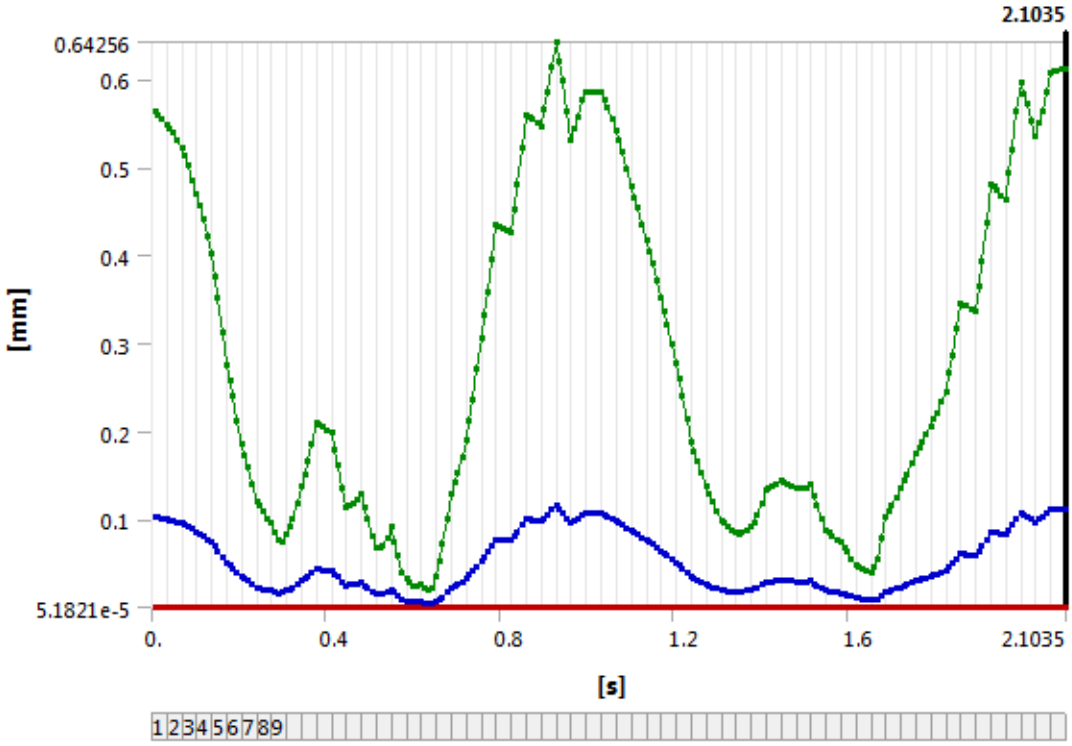

Appendix 29 Intracapsular Fracture Gait Total Deformation

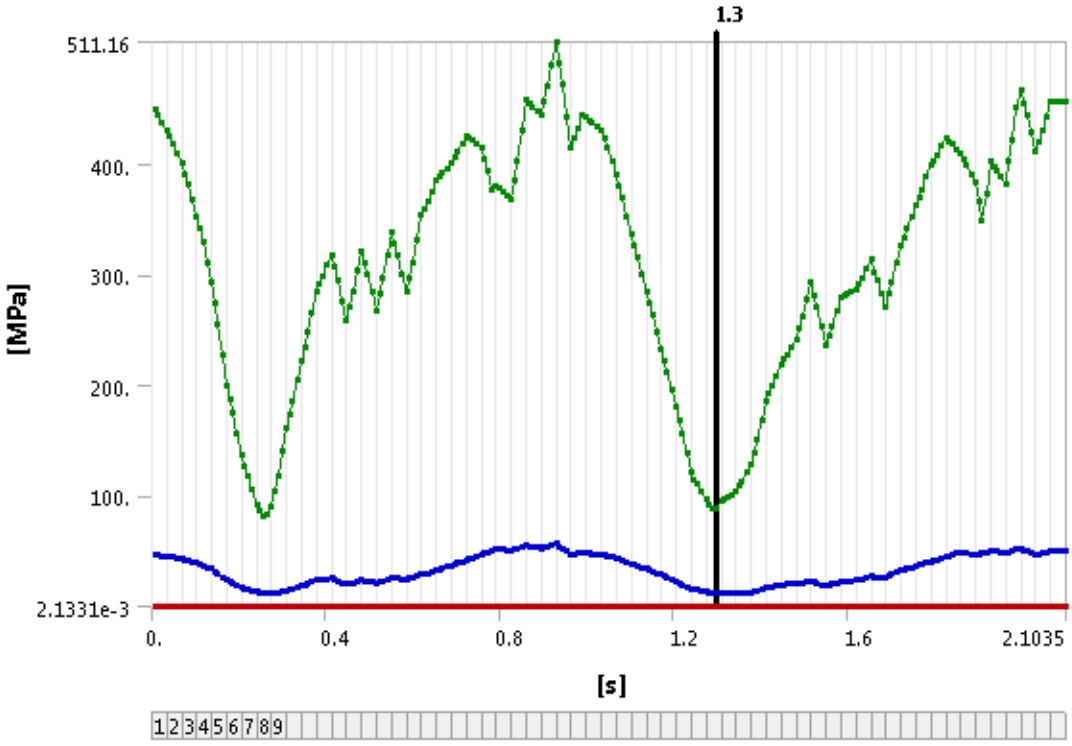

Appendix 30 Intracapsular Fracture Gait Equivalent Stress

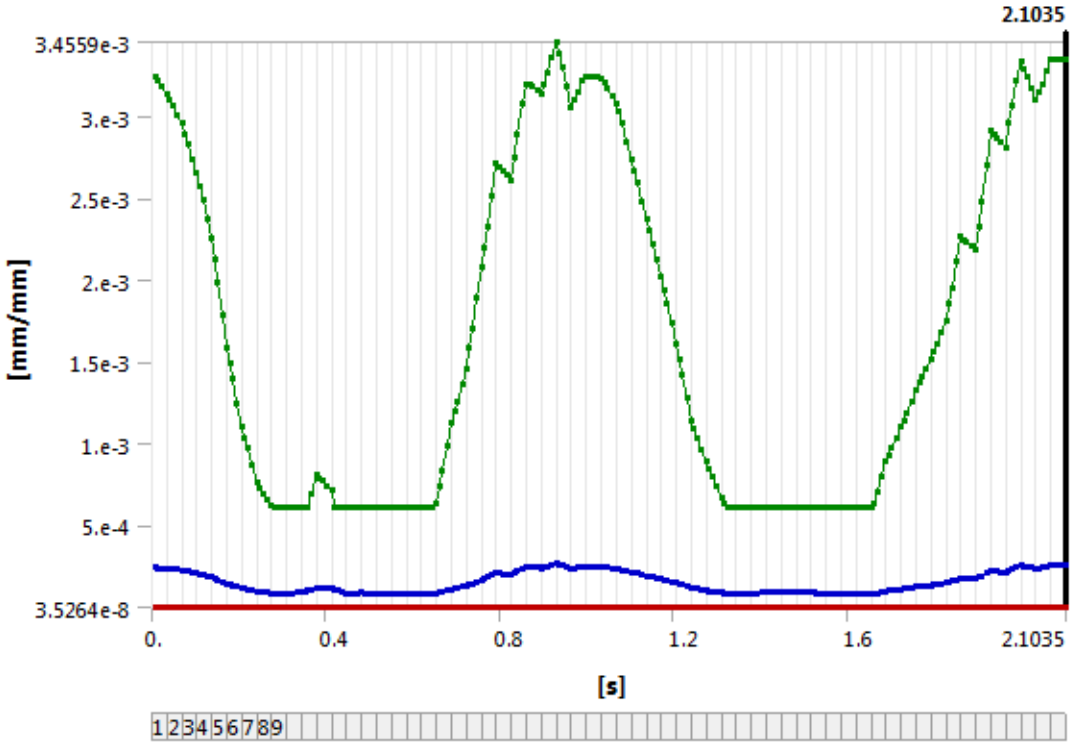

Appendix 31 Intracapsular Fracture Gait Elastic Strain

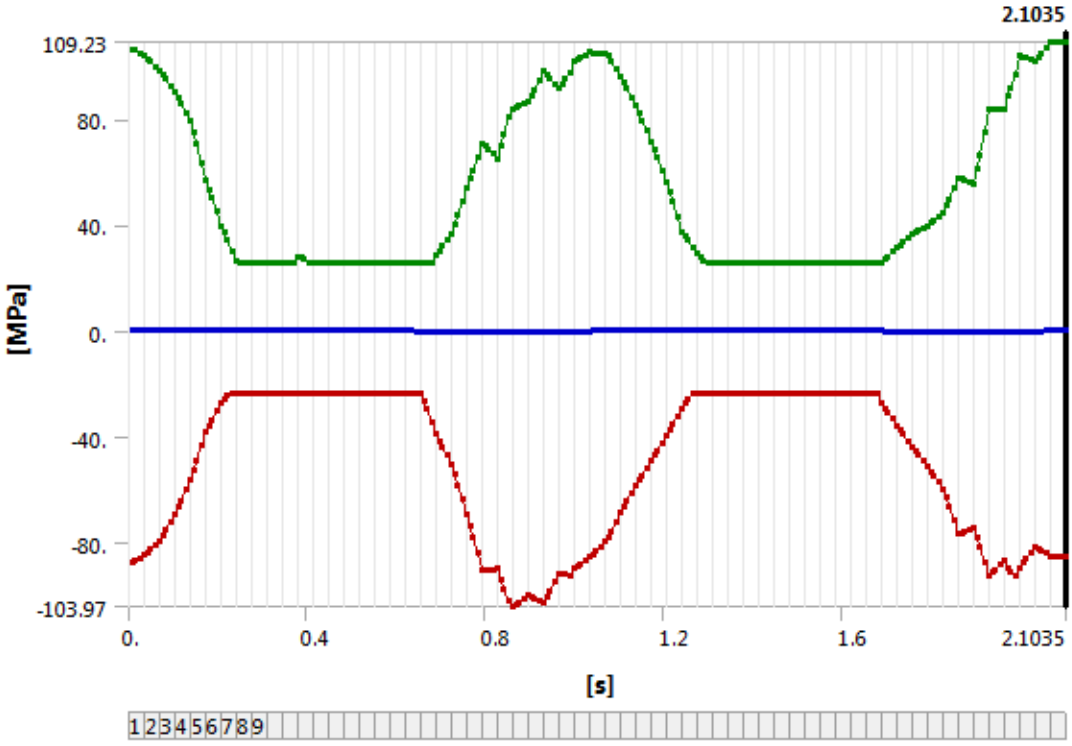

Appendix 32 Intracapsular Fracture Gait Shear Stress

References

1. Adedapo, A., & Ikpeme, J. (2001). The results of internal fixation of three-and four-part proximal humeral fractures with the polarus nail. *Injury, 32*(2), 115-121.
2. Asnis, S. E., & Wanek-Sgaglione, L. (1994). Intracapsular fractures of the femoral neck. results of cannulated screw fixation. *Jbjs, 76*(12), 1793-1803.
3. Belsky, M. R., Eaton, R. G., & Lane, L. B. (1984). Closed reduction and internal fixation of proximal phalangeal fractures. *The Journal of Hand Surgery, 9*(5), 725-729.
4. Black, D. M., Kelly, M. P., Genant, H. K., Palermo, L., Eastell, R., Bucci-Rechtweg, C., et al. (2010). Bisphosphonates and fractures of the subtrochanteric or diaphyseal femur. *New England Journal of Medicine, 362*(19), 1761-1771.
5. Blomstedt, P. (2014). Orthopedic surgery in ancient egypt. *Acta Orthopaedica, 85*(6), 670-676.
6. Bostman, O., Makela, E. A., Sodergard, J., Hirvensalo, E., Tormala, P., & Rokkanen, P. (1993). Absorbable polyglycolide pins in internal fixation of fractures in children. *Journal of Pediatric Orthopedics, 13*(2), 242-245.
7. Brorson, S. (2009). Management of fractures of the humerus in ancient egypt, greece, and rome: An historical review. *Clinical Orthopaedics and Related Research®, 467*(7), 1907-1914.
8. Burghardt, R. D., Specht, S. C., & Herzenberg, J. E. (2010). Mechanical failures of eight-plateguided growth system for temporary hemiepiphysiodesis. *Journal of Pediatric Orthopaedics, 30*(6), 594-597.

9. Cook, S. D., Renz, E. A., Barrack, R. L., Thomas, K. A., Harding, A. F., Haddad, R. J.,Jr, et al. (1985). Clinical and metallurgical analysis of retrieved internal fixation devices. *Clinical Orthopaedics and Related Research, (194)*(194), 236-247.
10. Cooper, C., Campion, G., & Melton, L. 3. (1992). Hip fractures in the elderly: A world-wide projection. *Osteoporosis International, 2*(6), 285-289.
11. Davis, T. R., Sher, J. L., Horsman, A., Simpson, M., Porter, B. B., & Checketts, R. G. (1990). Intertrochanteric femoral fractures. mechanical failure after internal fixation. *The Journal of Bone and Joint Surgery.British Volume, 72*(1), 26-31.
12. DePuy Synthes. *TFNAdvance proximal femoral nailling system.* Retrieved October 15, 2018, from http://synthes.vo.llnwd.net/o16/LLNWMB8/INT%20Mobile/Synthes%20International/Product%20Support%20Material/legacy_Synthes_PDF/DSEM-TRM-0514-0052-6_LR.pdf
13. Dienst, M., Wozasek, G. E., & Seligson, D. (1997). Dynamic external fixation for distal radius fractures. *Clinical Orthopaedics and Related Research®, 338*, 160-171.
14. Evans, W. (1998). Optimising mechanical properties in alpha beta titanium alloys. *Materials Science and Engineering: A, 243*(1-2), 89-96.
15. Farhoudi, H., Oskouei, R., Pasha Zanoosi, A., Jones, C., & Taylor, M. (2016). An analytical calculation of frictional and bending moments at the head-neck interface of hip joint implants during different physiological activities. *Materials, 9*(12), 982.

16. Forman, R. G., Kearney, V., & Engle, R. (1967). Numerical analysis of crack propagation in cyclic-loaded structures. *Journal of Basic Engineering, 89*(3), 459-463.
17. Frumberg, D. B., Van Lanen-Wanek, D. J., Jauregui, J. J., Nadarajah, V., & Illical, E. M. (2018). Can flexible intramedullary nails provide proper fixation of long bone fractures in patients weighing over 100 pounds? *Journal of Orthopaedics, Trauma and Rehabilitation,*
18. Gabarre, S., Herrera, A., Ibarz, E., Mateo, J., Gil-Albarova, J., & Gracia, L. (2016). Comparative analysis of the biomechanical behaviour of two cementless short stems for hip replacement: Linea anatomic and minihip. *PloS One, 11*(7), e0158411.
19. Gaines Jr, R. W. (2000). The use of pedicle-screw internal fixation for the operative treatment of spinal disorders. *Jbjs, 82*(10), 1458-1476.
20. Geraldes, D. M., Modenese, L., & Phillips, A. T. (2016). Consideration of multiple load cases is critical in modelling orthotropic bone adaptation in the femur. *Biomechanics and Modeling in Mechanobiology, 15*(5), 1029-1042.
21. Gerber, C., Mast, J., & Ganz, R. (1990). Biological internal fixation of fractures. *Archives of Orthopaedic and Trauma Surgery, 109*(6), 295-303.
22. Goswami, T., Gundapaneni, D., Slocum, M., Paul, P., & Christof, S. (2016). Failure investigation of a tibiotalocalcaneal arthrodesis system. *Engineering Failure Analysis, 59*, 588-604.
23. Gullberg, B., Johnell, O., & Kanis, J. (1997). World-wide projections for hip fracture. *Osteoporosis International, 7*(5), 407-413.

24. Hamandi, F., Laughlin, R., & Goswami, T. (2018). Failure analysis of PHILOS plate construct used for pantalar arthrodesis paper II—Screws and FEM simulations. *Metals, 8*(4), 279.

25. Harding, J. L., & Reynolds, M. M. (2014). Combating medical device fouling. *Trends in Biotechnology, 32*(3), 140-146.

26. ***Hip fracture***. Retrieved April 15, 2019, from https://www.physio-pedia.com/Hip_Fracture#cite_note-7

27. Centers for Disease Control and Prevention. ***Hip fractures among older adults***. (September 20, 2016). Retrieved April 8, 2019, from https://www.cdc.gov/homeandrecreationalsafety/falls/adulthipfx.html

28. Hodgskinson, R., & Currey, J. (1992). Young's modulus, density and material properties in cancellous bone over a large density range. *Journal of Materials Science: Materials in Medicine, 3*(5), 377-381.

29. Ina, J., Vallentyne, M., Hamandi, F., Shugart, K., Boin, M., Laughlin, R., et al. (2018). Failure analysis of PHILOS plate construct used for pantalar arthrodesis paper I—analysis of the plate. *Metals, 8*(3), 180.

30. Johner, R., & Wruhs, O. (1983). Classification of tibial shaft fractures and correlation with results after rigid internal fixation. *Clinical Orthopaedics and Related Research, (178)*(178), 7-25.

31. Johnson, N., Uzoigwe, C., Venkatesan, M., Burgula, V., Kulkarni, A., Davison, J., et al. (2017). Risk factors for intramedullary nail breakage in proximal femoral fractures: A 10-year retrospective review. *The Annals of the Royal College of Surgeons of England, 99*(2), 145-150.

32. Kuroda, D., Niinomi, M., Morinaga, M., Kato, Y., & Yashiro, T. (1998). Design and mechanical properties of new β type titanium alloys for implant materials. *Materials Science and Engineering: A, 243*(1-2), 244-249.
33. Kyle, R., Gustilo, R., & Premer, R. (2010). Analysis of six hundred and twenty-two intertrochanteric hip fractures. *Orthopedic Trauma Directions, 8*(06), 25-29.
34. Lawrence, T. M., White, C. T., Wenn, R., & Moran, C. G. (2005). The current hospital costs of treating hip fractures. *Injury, 36*(1), 88-91.
35. Lotz, J., Cheal, E., & Hayes, W. C. (1991). Fracture prediction for the proximal femur using finite element models: Part I—linear analysis. *Journal of Biomechanical Engineering, 113*(4), 353-360.
36. Lotz, J. C., Cheal, E. J., & Hayes, W. C. (1991). Fracture prediction for the proximal femur using finite element models: Part II--nonlinear analysis. *Journal of Biomechanical Engineering, 113*(4), 361-365.
37. Milbank, A. J., Montague, D. K., Angermeier, K. W., Lakin, M. M., & Worley, S. E. (2002). Mechanical failure of the american medical systems ultrex inflatable penile prosthesis: Before and after 1993 structural modification. *The Journal of Urology, 167*(6), 2502-2506.
38. Muminagic, S. N. (2011). History of bone fracture: Treatment and immobilization. *Materia Socio-Medica, 23*(2), 111.
39. Niinomi, M. (2007). Fatigue characteristics of metallic biomaterials. *International Journal of Fatigue, 29*(6), 992-1000.
40. Ogden, C. L., Fryar, C. D., Carroll, M. D., & Flegal, K. M. (2004). Mean body weight, height, and body mass index, united states 1960-2002.

41. Osorio, I., Frei, M. G., & Bhavaraju, N. C. (2008). *Medical Device Failure Detection and Warning System,*

42. Palanisamy, A. M., Doshi, H., Selvaraj, D., Chan, W., Naidu, G., & Ramason, R. (2015). Fixation versus replacement in geriatric hip fractures: Does functional outcome and independence in self-care differ? *Geriatric Orthopaedic Surgery & Rehabilitation, 6*(4), 258-262.

43. Paris, P., & Erdogan, F. (1963). A critical analysis of crack propagation laws. *Journal of Basic Engineering, 85*(4), 528-533.

44. Parker, M. J., White, A., & Boyle, A. (2008). Fixation versus hemiarthroplasty for undisplaced intracapsular hip fractures. *Injury, 39*(7), 791-795.

45. Pavlina, E., & Van Tyne, C. (2008). Correlation of yield strength and tensile strength with hardness for steels. *Journal of Materials Engineering and Performance, 17*(6), 888-893.

46. Russell, T. A., & Pepper, J. R. (1996). *Femoral Intramedullary Nail,*

47. Salib, P. (1962). Orthopaedic and traumatic skeletal lesions in ancient egyptians. *The Journal of Bone and Joint Surgery.British Volume, 44*(4), 944-947.

48. Seo, J., Min, H., Kim, D. M., Oh, S., & Kim, S. (2016). Surgical results of the cephalomedullary nail for the femoral intertrochanteric fracture: Comparison between non-experienced surgeons and experienced surgeon. *Hip & Pelvis, 28*(4), 225-231.

49. Shemshaki, H. R., Mousavi, H., Salehi, G., & Eshaghi, M. A. (2011). Titanium elastic nailing versus hip spica cast in treatment of femoral-shaft fractures in children. *Journal of Orthopaedics and Traumatology, 12*(1), 45-48.

50. Smith, G. E. (1908). The most ancient splints. *British Medical Journal, 1*(2465), 732-736.2. doi:10.1136/bmj.1.2465.732 [doi]

51. Sullivan, R. (1996). The identity and work of the ancient egyptian surgeon. *Journal of the Royal Society of Medicine, 89*(8), 467-473.

52. Swiontkowski, M. F. (2009). Intracapsular fractures of the hip. *Orthopedic Trauma Directions, 7*(01), 31-33.

53. von Rüden, C., Hungerer, S., Augat, P., Trapp, O., Bühren, V., & Hierholzer, C. (2015). Breakage of cephalomedullary nailing in operative treatment of trochanteric and subtrochanteric femoral fractures. *Archives of Orthopaedic and Trauma Surgery, 135*(2), 179-185.

54. Weiss, I., & Semiatin, S. (1998). Thermomechanical processing of beta titanium alloys—an overview. *Materials Science and Engineering: A, 243*(1-2), 46-65.

55. Wheeless, C. R. (1996). *Wheeless' textbook of orthopaedics* CR Wheeless, MD.

56. Wills, R. P., & Brooker, A. F. (1985). *Distal Locking Intramedullary Nail,*

57. Winquist, R. A., & Hansen, S. T.,Jr. (1980). Comminuted fractures of the femoral shaft treated by intramedullary nailing. *The Orthopedic Clinics of North America, 11*(3), 633-648.

58. Wirtz, D. C., Schiffers, N., Pandorf, T., Radermacher, K., Weichert, D., & Forst, R. (2000). Critical evaluation of known bone material properties to realize anisotropic FE-simulation of the proximal femur. *Journal of Biomechanics, 33*(10), 1325-1330.

59. Woo, S. L., Lothringer, K., Akeson, W., Coutts, R., Woo, Y., Simon, B., et al. (1983). Less rigid internal fixation plates: Historical perspectives and new concepts. *Journal of Orthopaedic Research, 1*(4), 431-449.

60. Zadpoor, A. A., & Nikooyan, A. A. (2011). The relationship between lower-extremity stress fractures and the ground reaction force: A systematic review. *Clinical Biomechanics, 26*(1), 23-28.

61. Zannoni, C., Mantovani, R., & Viceconti, M. (1999). Material properties assignment to finite element models of bone structures: A new method. *Medical Engineering & Physics, 20*(10), 735-740.

62. ASTM F1295-05, Standard Specification for Wrought Titanium-6 Aluminum-7 Niobium Alloy for Surgical Implant Applications (UNS R56700), ASTM International, West Conshohocken, PA, 2005, www.astm.org

63. ASTM F2066-18, Standard Specification for Wrought Titanium-15 Molybdenum Alloy for Surgical Implant Applications (UNS R58150), ASTM International, West Conshohocken, PA, 2018, www.astm.org

64. ASTM F620-00, Standard Specification for Alpha Plus Beta Titanium Alloy Forgings for Surgical Implants, ASTM International, West Conshohocken, PA, 2000, www.astm.org